

Trustworthiness of Laser-Induced Breakdown Spectroscopy Predictions via Simulation-based Synthetic Data Augmentation and Multitask Learning

Riccardo Finotello^{*1,2}, Daniel L’Hermite^{†1}, Celine Quéré^{‡1}, Benjamin Rouge^{§1}, Mohamed Tamaazousti^{¶2} and Jean-Baptiste Sirven^{||1}

¹Université Paris-Saclay, CEA,
Service d’études analytiques et de réactivité des surfaces (SEARS),
Gif sur Yvette, F-91191, France
²Université Paris-Saclay, CEA,
LIST,
Palaiseau, F-91120, France

Abstract

We consider quantitative analyses of spectral data using laser-induced breakdown spectroscopy. We address the small size of training data available, and the validation of the predictions during inference on unknown data. For the purpose, we build robust calibration models using deep convolutional multitask learning architectures to predict the concentration of the analyte, alongside additional spectral information as auxiliary outputs. These secondary predictions can be used to validate the trustworthiness of the model by taking advantage of the mutual dependencies of the parameters of the multitask neural networks. Due to the experimental lack of training samples, we introduce a simulation-based data augmentation process to synthesise an arbitrary number of spectra, statistically representative of the experimental data. Given the nature of the deep learning model, no dimensionality reduction or data selection processes are required. The procedure is an end-to-end pipeline including the process of synthetic data augmentation, the construction of a suitable robust, homoscedastic, deep learning model, and the validation of its predictions. In the article, we compare the performance of the multitask model with traditional univariate and multivariate analyses, to highlight the separate contributions of each element introduced in the process.

highlights: we build an end-to-end pipeline to deal with data augmentation, robust multitask deep calibration models and the trustworthiness assessment of LIBS predictions.

keywords: LIBS, calibration, deep learning, data augmentation, trustworthy AI

*e-mail: riccardo.finotello@cea.fr

†e-mail: daniel.lhermite@cea.fr

‡e-mail: celine.quere@cea.fr

§e-mail: benjamin.rouge54@gmail.com

¶e-mail: mohamed.tamaazousti@cea.fr

||e-mail: jean-baptiste.sirven@cea.fr

Contents

1	Introduction	3
2	Related Works	4
2.1	Data Augmentation	5
2.2	Multitask Learning	5
2.3	Trustworthy AI	6
3	Methodology	6
3.1	Simulation-based Synthetic Data Augmentation	6
3.2	Multitask Convolutional Neural Networks	10
3.3	Trustworthiness of the Model Via Validation of the Predictions	12
4	Implementation and Experimental Details	13
4.1	Experimental Setup	14
4.2	Secondary Outputs	15
4.3	Train and Test Sets Selection	15
4.4	Preprocessing	16
4.5	Evaluation Metrics	17
4.6	Training and Optimisation Strategies	17
4.6.1	Input Representation	17
4.6.2	Fully Connected Neural Networks	17
4.6.3	Multitask Architectures	18
4.6.4	Hyperparameter Optimisation Strategy	19
4.6.5	Training of the Neural Networks	19
4.7	Neural Network Architectures	19
4.7.1	Fully Connected Neural Networks	20
4.7.2	Multitask Neural Networks	20
4.8	Software and Hardware Setups	21
5	Results and Discussion	23
5.1	Baseline Analysis	23
5.1.1	Traditional Algorithms	23
5.1.2	Multitask Learning Without Synthetic Data Augmentation	25
5.2	Performance Review of the Multitask Approach	25
5.2.1	Training Set Size	25
5.2.2	Random Noise	27
5.2.3	Validation of the Results	29
5.2.4	Anomaly Detection Mechanism: Calibration Transfer	32
5.2.5	Towards the Resolution of Spectral Interference	33
6	Conclusions	34
	References	36
A	Compositions of the Matrices	i
B	Implementation Details	iv
C	Results	vi
D	Complementary Figures	xi

1 Introduction

Deep Learning (DL) has been widely developed with great success in many areas, among which computer vision and natural language processing have become well-known mainstream applications. The performance of those algorithms in solving complex tasks stimulated their development in many other fields. Analytical chemistry is no exception to the rule. As recently reviewed by Dubus et al., DL has already proved successful in chromatography, spectroscopy, chemical sensing, imaging applications [1]. Historically, some optical spectrometry techniques have particularly benefited from multivariate approaches. The example of near-infrared spectroscopy shows that they have become unavoidable for decades [2]. Their development is more recent in the Laser-Induced Breakdown Spectroscopy (LIBS) community, but it has been growing for more than 15 years. In this field, the possibility to make fast measurements with detectors of hundreds to several millions pixels for *Echelle* spectrometers rapidly leads to a large amount of experimental data, and this is all the truer for hyperspectral imaging applications [3], [4]. Data processing algorithms with a variable degree of complexity were successfully applied to LIBS datasets for efficient detection of compounds, samples classification, quantitative analysis or chemical mapping. Basic artificial Neural Networks (NNS) were implemented as soon as the '90s for identification of polymers [5]. Beyond, in the second half of the 2010s, Machine Learning (ML) techniques first, DL after, have been more and more developed. The recent review of Li et al. showed that modern concepts and architectures of NNS have already been tested in LIBS, and this seems to be a promising direction to explore [6].

In quantitative analysis by spectroscopic methods, the objective is to build a model relating experimental spectra to the concentration of the species of interest. This is based on a set of known calibration samples, and can be done by a variety of supervised techniques. A quantitative model is then valid for a given sample matrix and for given experimental conditions. However, for direct analytical techniques like LIBS, which do not require sample preparation, it can happen that an unknown sample has a slightly different matrix compared to calibration ones, or that its measurement conditions are slightly variable. In this case, it can be expected that the predicted concentration is biased to a certain extent. Yet, a quantitative model is designed to deliver a concentration but not to estimate to which extent an unknown sample is well represented by calibration ones. In other words, we do not know how reliable the prediction is. It is therefore necessary to develop models that are able to estimate, if possible quantitatively, the trustworthiness of a prediction. Thanks to their ability to perform different tasks in parallel, MultiTask (MT) NNS are a type of model that could address this issue. However, a well-known drawback of NNS is that they are easily prone to overfitting of training data, since they require a very large number of spectra to be properly trained. Experimental, time and cost constraints generally do not enable to acquire enough spectra. A possibility to overcome this limitation is to generate calibration data. This can be done either by transforming the initial spectra, or by phenomenological modelling of training spectra, or by hard modelling based on physical equations – in the case of LIBS, the equations ruling laser ablation, the plasma formation and emission.

The objective of this paper is then to introduce a new approach of quantitative analysis by LIBS and DL, enabling both to generate enough spectra to train a model based on MT Convolutional Neural Networks (CNNs), and to evaluate the confidence in the model predictions. In this article, we propose a methodology for calibration models based on three fundamental elements:

1. simulation-based synthetic data augmentation, namely the generation of an arbitrary number of new spectra from experimental data to train complex DL architectures;
2. robust deep MT CNNs, capable of processing entire LIBS spectra and increasing the robust-

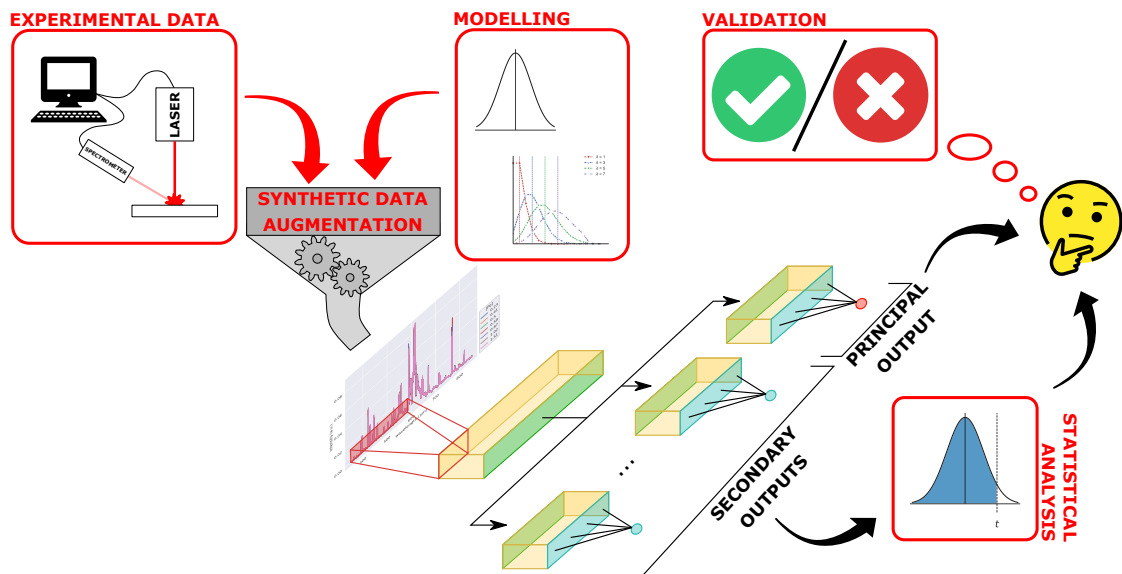


Figure 1.1. Schematics of the methodology. *Mathematical modelling and experimental data are used as inputs for the data augmentation procedure. A robust multitask model is trained on synthetic data to predict a principal variable (e.g. the concentration of the analyte) and several secondary spectral quantities, which can be verified on experimental data. Given the inter-dependence of the parameters of the network, the statistical analysis of the latter enables the assessment the trustworthiness of the predictions of the principal output.*

ness (homoscedasticity) of the model;

3. measure of the trustworthiness of the predictions of the model through the statistical analysis of the inter-dependencies of the parameters and the outputs of the MT architecture.

The procedure, presented in Figure 1.1, aims at providing a way to increase the robustness of the calibration models, and to benchmark the confidence of the Artificial Intelligence (AI) architecture through its own predictions.

In the article, we first revise the State-Of-The-Art (SOTA) of augmentation, DL and trustworthy AI in LIBS. We then move to the description of the technique, introducing in detail the three mentioned aspects. In the following section, we discuss the experimental setup and the details of the implementation. We then show the results of the analysis, compared to known techniques in the LIBS literature, and we provide a separate analysis of the contribution of each element.

2 Related Works

Several univariate and multivariate calibration techniques are explored in the literature [7]. The first are widely adopted for their ability to provide interpretable results quickly and with good precision [8]. In this scenario, calibration standards are used to build a map between the concentration of a given analyte and the information contained in a single measurable variable, such as the integral intensity of an emission line. The model is then inverted during inference to use the measured intensity as predictor to predict the concentration of the analyte. On the other hand, multivariate methods were introduced for their ability to take advantage of more information

contained in the input spectra, rather than focusing on a single variable. Techniques based on principal components and multilinear regression have been widely adopted in LIBS [9]–[12]. As a multivariate technique, DL has also been explored at length, comparing various types of architectures [6], [13], [14]. In particular, CNNs present interesting properties, capable of scanning complex spectral data, with minimal preprocess treatments needed [15]. It is often coupled to dimensionality reduction algorithms or to input selection criteria [16]–[19]. However, the increased computational power witnessed in the last decade, enables avoiding the loss of information in the spectra [20]–[23].

2.1 Data Augmentation

Though DL shows potential for various analyses, time and experimental conditions often prevent building large LIBS datasets. The preferred solution seems to be the simplification of the models and an accurate selection of the input data. Feature engineering and feature selection, for instance through a principal components analysis or *a priori* expertise, have been employed to reduce the size of the input data [16], [18]. At the same time, the production of purely synthetic data, based on local thermodynamical equilibrium, has been explored in LIBS applications [24]. The idea of enriching existing data by means of different representations of the inputs, such as time resolved spectra, was experimented with success [25]. However, most of the time, no real augmentation of the training datasets is provided, at least in the same sense as in modern ML [21]. More recently, standard data augmentation techniques were used for the classification of LIBS maps, though mostly exploiting the spatial information of the two-dimensional maps, rather than the spectral distribution of the signal [6]. Augmentation through synthetic data via the simple addition of random noise to the experimental data is also briefly discussed in the literature, though no implementations seem to be present [23].

2.2 Multitask Learning

Though explored at length in ML literature [26], [27], recently, MT learning has seen major developments and a wide range of applications. In particular, it has been shown to improve the performance of different computer vision models [28], used, for instance, for multiple object detection in self-driving cars. At the same time, the possibility to create latent common representations for multiple tasks has been considered for computations in fundamental research in physics and mathematics [29]–[31]. Its improved generalisation ability on multiple tasks is used for the creation of versatile agents [32], towards the definition of Artificial General Intelligence [33]. In LIBS applications, univariate and multivariate analyses focus on the prediction of a single output, usually the concentration of the analyte. However, some examples of multi-output algorithms were recently explored, based on NNS [25], [34] and on Partial Least Squares (PLS) with two outputs, i.e. PLS2 [35]. In these cases, the response variables are usually the concentrations of multiple elements. Interestingly, multi-output NN architectures found successful applications for the computation of plasma parameters from LIBS data [36], [37]. MT learning was also introduced for the simultaneous predictions of concentrations of analytes and lithology classes: different NNS were used to process the data with different loss functions, using a latent representation of the input, computed by a common backbone architecture [38]. This shows the viability of MT learning as an analysis technique in LIBS, capable of providing information of different nature on related tasks, at the same time.

2.3 Trustworthy AI

Once the calibration model is defined, it is difficult to assess the correctness of the predictions for unknown samples. Standard techniques in statistics are usually employed [39], [40], though they rely on strong assumptions on the type of data analysed, notably their heteroscedasticity [41]. Moreover, calibration-free methods in LIBS have been proven successful in providing robust elemental analyses [42]–[46], with the possibility to compare the predictions with sensible physical hypotheses. On the other hand, it has been seen heuristically that traditional models do not systematically generalise to unknown data [6], [34], [47]. For instance, algorithms used for calibration can present different performances at different levels of concentrations, hence the possible need to separately work on different sub-populations of samples [35]. Random permutations and cross-validation of the samples used in the NN models have also been proposed to test the robustness of the algorithms, by measuring the differences in the prediction on given samples [47]. The computation of misclassification probability based on ML methods has also been considered, in order to assess the validity of classification models [48]. Recently, different teams proposed DL frameworks to understand the learning process of the AI architectures for spectral data. These interpretable-AI methods either analyse the progression of the feature maps in the hidden layers [49], or study the importance of the spectral variables leading to the prediction [50]. This represents indeed a step towards the comprehension of the mechanisms behind NNS, as it enables a semi-quantitative analysis of the hidden layers. Nevertheless, it does not deal with the confidence of the predictions, or the automatic detection of changes in the distribution of the samples. As a matter of fact, the validation of the outputs of a model, and the study of their trustworthiness, remains a challenging task, with only a few algorithmic implementations or statistical treatments.

3 Methodology

We use a DL approach based on MT learning to increase the robustness of the models. We predict, at the same time, the concentration of the analyte and a set of related spectral quantities. Given the complexity of the architecture, we introduce a simulation-based data augmentation to increase the number of available spectra for training. Though formally inspired by traditional data augmentation techniques, we focus on generating new synthetic spectra from a theoretical prior on the experimental data, rather than transforming the experimental spectra. Finally, we validate the predictions of the model using the additional outputs of the MT architecture as reference for a statistical analysis. The procedure is used to reveal possible anomalies in training or modifications of the experimental conditions.

3.1 Simulation-based Synthetic Data Augmentation

For the analysis, we build complex DL architectures, with a large number of free parameters, compared to traditional models. In this regime, training large NNS by optimising the bias-variance trade-off may lead to phenomena such as poor stability and bad generalisation in inference on unknown samples. Many training samples are usually required to train more complex architectures to overcome the issues. Inspired by usual DL practices, we thus introduce a data augmentation technique for LIBS.

We train the MT model on entire LIBS spectra, without *a priori* data selection. For the LIBS analysis, typical data augmentations used in computer vision, and based on rotations, reflections and crops, may jeopardise the predictive power of the model: the spatial distribution of the wavelength channels, and their neighbouring relations, should not be altered randomly by

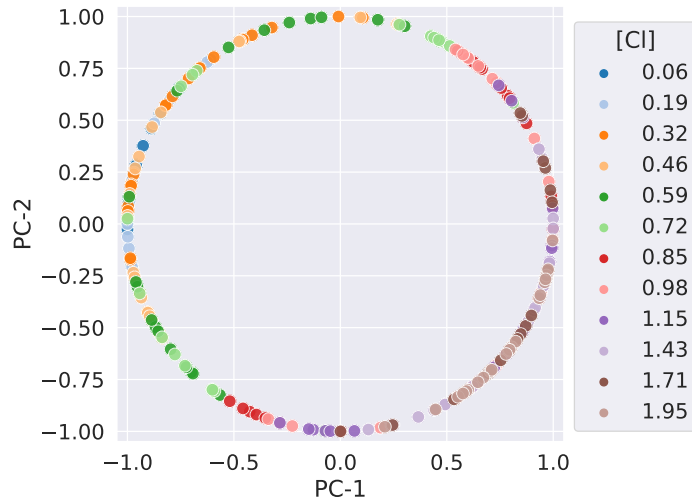


Figure 3.1. Sample training distribution at different concentrations. *Example of the training distribution of cement samples (described in the text) as principal components in feature space, normalised to the unit sphere. Differences in distribution display as rotations.*

transformations, in order to retain a physical meaning. At the same time, given the scarcity of training data, the simple addition of random noise to the experimental spectra may result in a training distribution no longer representative, at least locally, of the use case. As a reference, Figure 3.1 shows the span of the first two principal components of the distribution, normalised to the unit sphere to highlight differences as rotations. We first proceed to model the distribution of the original spectra, and then to synthetically produce an arbitrary number of spectra. We show that noise can be added to each individual channel, provided that its global average effect is negligible, in order to make the synthetic distribution more realistic. For instance, this influences locally the models which use small mini-batches of spectra for training, such as NNS (see Section 5.1.1 for additional details). The procedure ensures to enlarge consistently the feature space spanned by the synthetic spectra. The generated samples are able to cover an extended range of variations inside the original distribution, before the addition of noise. In turn, we noticed that the model is able to generalise to unknown data more efficiently.

From a technical point of view, we first compute the average experimental spectrum of each sample as input of the data synthesis technique. This alleviates the effects of possible experimental local signal fluctuations. It also ensures the statistical consistency of the frequentist analysis. We then consider each wavelength channel as independently modelled by a random variable following a probability distribution function, whose expected value is represented by the average spectrum. As a whole, the expected values follow another probability distribution, which reproduces the profile of the emission lines (or bands) in the average spectrum, experimentally available. That is, we consider the set of n spectra with p wavelength channels $\{\mathbf{x}^{(i)} \in \mathbb{R}^p\}_{i \in [1, n]}$ and the corresponding average spectrum $\bar{\mathbf{x}} = (\bar{x}_r) \in \mathbb{R}^p$, where $\bar{x}_r = \mathbb{E}[x_r]$. For each wavelength channel $r = 1, 2, \dots, p$, we fix the expected value of a random variable $y_r \in \mathbb{R}$ such that $\mathbb{E}[y_r] = \bar{x}_r$. Generalising to an arbitrary number m of random variables, we consider the set:

$$\left\{ y_r^{(j)} \in \mathbb{R} \mid \mathbb{E} \left[y_r^{(j)} \right] = \bar{x}_r, \quad j = 1, 2, \dots, m \right\}. \quad (3.1)$$

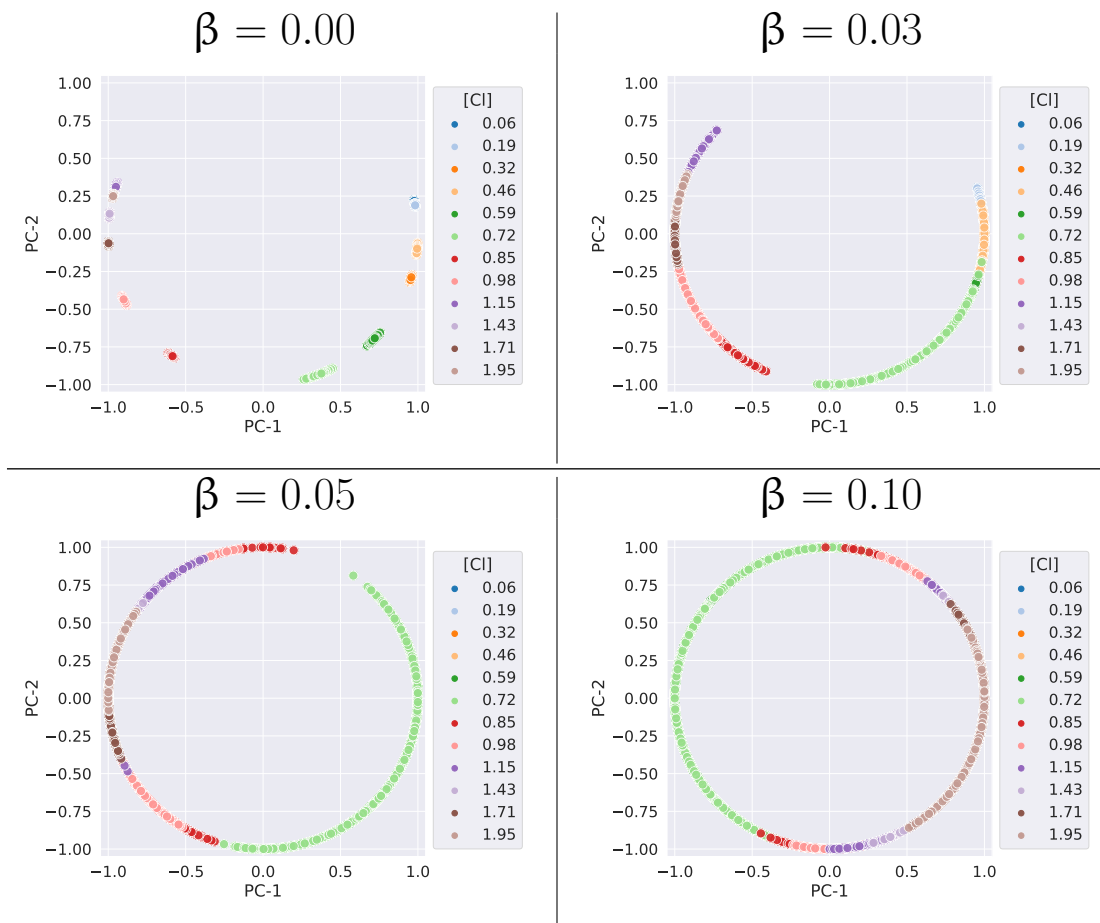


Figure 3.2. Qualitative effects of the confounder parameter β . *Synthetic data under the influence of a noise parameter locally span the entire feature space, rather than forming cluster structures. The overall distribution is more realistic (see Figure 3.1).*

An arbitrary number $m \gg n$ of full spectra can be constructed by similarly proceeding for all wavelength channels $r \in [1, p]$.

In detail, we model the intensity of a given wavelength channel as a probability distribution

$$P(\lambda, \beta) = P_1(\lambda \mid \beta) P_2(\beta), \quad (3.2)$$

where λ represents the experimental photon-like contributions to the LIBS spectra (either the genuine signal or low-intensity photon noise), while β is a confounder variable, modelling external factors. In this realisation, we achieve good performance by choosing independent variables λ and β (i.e. $P_1(\lambda \mid \beta) = P_1(\lambda)$), leading to $P(\lambda, \beta) = P_1(\lambda) P_2(\beta)$, for the synthetic spectra. In Figure 3.2, we show the effect of β on the distribution of the synthetic spectra. Qualitatively, the confounder parameter makes the synthetic set locally more realistic, by enlarging the portion of feature space spanned by the spectra. Specifically, we model the spectral intensity of a wavelength channel r through a variable y_r using a Poisson-like law. We decompose

$$y_r = z_r p_r, \quad z_r \sim \mathcal{N}(1, \beta), \quad p_r \sim \mathcal{P}(\bar{x}_r), \quad (3.3)$$

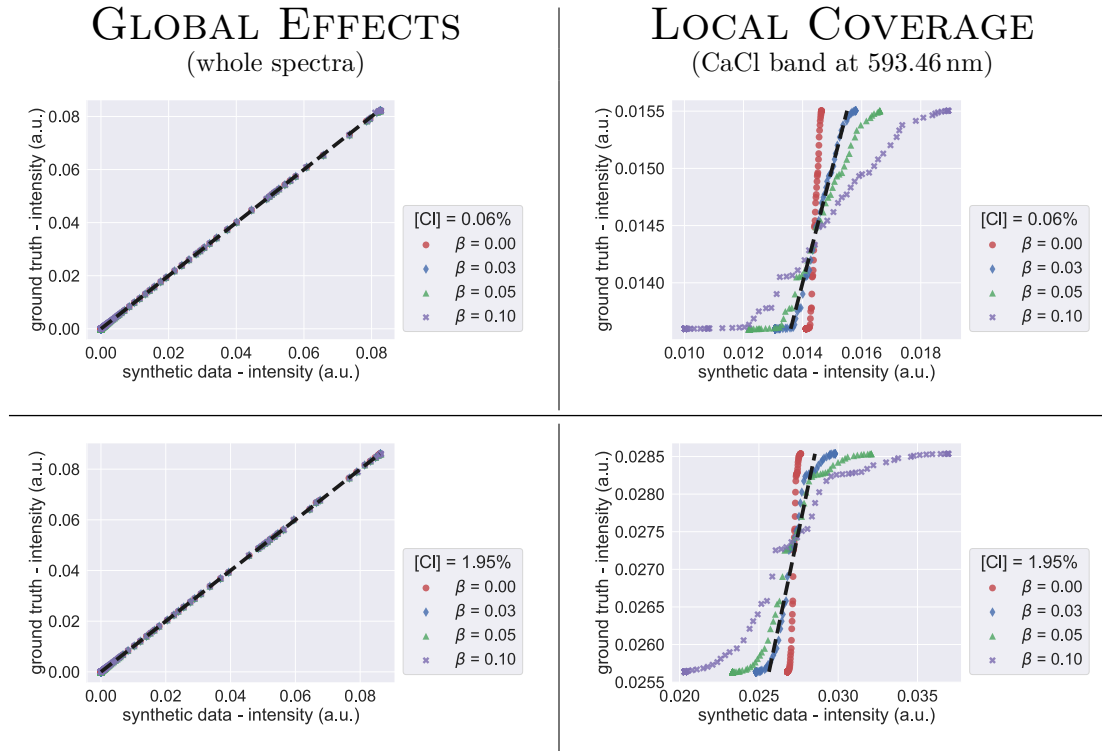


Figure 3.3. Global and local quantitative effects of the noise parameter (low concentration of the analyte at the top, higher concentration at the bottom). *The confounder parameter β does not impact the average (global) distribution of the spectra. However, it presents local differences at given wavelengths and for different concentrations of the analyte.*

where $\mathcal{N}(\mu, \sigma)$ is a normal distribution with expected value μ and variance σ^2 , and $\mathcal{P}(\lambda)$ is a Poisson distribution with expected value and variance λ . As z_r and p_r are independently sampled, we have $\mathbb{E}[y_r] = \mathbb{E}[z_r] \mathbb{E}[p_r] = \bar{x}_r$ for $r = 1, 2, \dots, p$.

We can use the spectra in the training sets to choose appropriate values of β . For illustration purposes, in Figure 3.3 we present the quantitative effects of different choices of β on the modelled distribution using a quantile-quantile diagram of the average spectra to compare the real and the synthetic distributions. We use a dataset of cement samples, described in Section 4.1, for the prediction of chlorine concentration. On average, the generated samples seem to reproduce correctly, on a global scale, the ground truths, especially at low signal intensity, as shown on the left of Figure 3.3: as expected, β as a low impact as a global effect. Moreover, the average spectra of the synthetic samples do not present strong deviations from the original distribution, suggesting that the theoretical model may correctly represent the experimental data. On the right, we study in detail the statistical coverage of the simulated spectra at a given wavelength, namely the CaCl emission band at 593.46 nm, used later in the analysis to infer the concentration of Cl in the samples. In the absence of the parameter β , the statistical model is over-confident at (i.e. it does not reproduce the full distribution) low intensity and under-confident at higher intensities (i.e. it creates out-of-distribution intensities), while the opposite occurs for higher values of the noise parameter. This suggests that there is an optimum of the parameter β , for which the synthetic distribution covers correctly the variance of the training distribution at

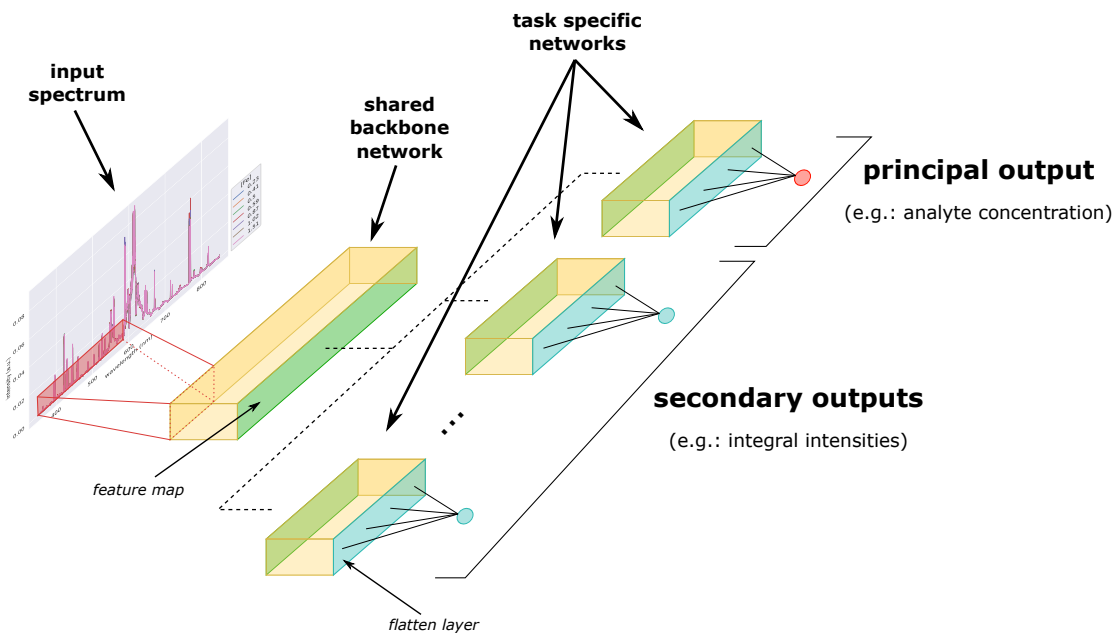


Figure 3.4. Structure of the DL architecture. *The model is a hard parameter sharing structure built using a common backbone network and several heads, connected to the shared feature map and computing regression scalars.*

a local level. The value of β can be chosen deterministically by maximising the coefficient of determination (R^2) between the ground truths and the synthetic quantiles at a given wavelengths of interest, or by weighting the R^2 at different relevant wavelengths. In Figures D.1 to D.4 in Appendix D, we show the same diagrams for different alloy matrices, introduced in Section 4.1. The effect of the noise parameter β is different depending on the matrix, and results suggest that it may be advisable to model independently each sample at different concentrations of the analyte, even though the global results do not deviate from the experimental distribution. However, as shown later in Section 5, the case of the alloy matrices presents peculiarities in the DL model which mitigate the differences in the theoretical priors, leading to a less intense impact of the choice of β with respect to the cement samples. In the article, we provide the results for several values of β for comparison, without focusing on finding the optimal value of the parameter.

3.2 Multitask Convolutional Neural Networks

By definition, multi-output NNs are a broad class of algorithms, which provide multiple predictions at the same time, using a shared structure of weights, trained simultaneously. MT networks are a subset of these architectures, implementing different strategies for sharing the training of their free parameters. This property gives the networks great versatility, as it is capable of using information on one task to improve its generalisation. This strategy acts as a regularisation and reduces the overfitting of the training data, as the model supposedly learns new representations, which should generalise well on all tasks [26], [27]. However, outputs need to be chosen carefully, such that the every single output could benefit from learning the others [51], [52].

In this analysis, we use a *hard parameter sharing* implementation of MT learning, with a

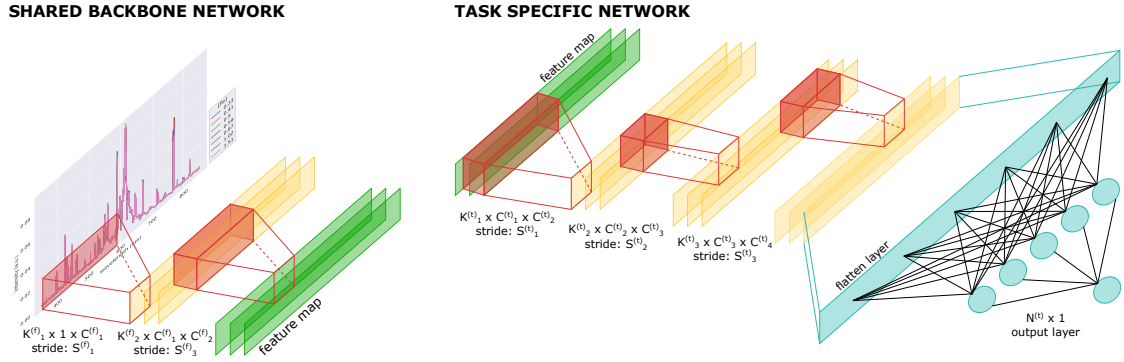


Figure 3.5. Structures in the MT architecture. *The shared backbone is a one dimensional CNN, which processes the spectra and produces a latent vector representation. The task-specific networks are CNNs with shallow FCNNs as top layers.*

common set of bottom layers (see the general schematics in Figure 3.4). The MT architecture is made by different sub-structures, shown in Figure 3.5. The innermost backbone processes the input spectra and produces a new latent vector representation. The task-specific heads separately use the latent representation as inputs to compute a scalar regression output. We use one-dimensional convolutions in the spectral dimension of the data cube as main operation. This is repeated on different channels, thus adding a depth dimension to the output. Additional details on the exact implementation of the architecture are in Section 4.

The choice of the outputs is particularly relevant, as their predictions from a common representation should be mutually beneficial. From a likelihood perspective, let the variables Y_1 and Y_2 be two outputs of the MT learning architecture, given an input X . The model aims at maximising, as a function of the parameters, the function:

$$P(Y_1, Y_2 | X; \{A, B, \Omega\}) = \frac{1}{2} P(Y_1 | Y_2; X; \{A, B, \Omega\}) P(Y_2 | X; \{A, B, \Omega\}) + (1 \leftrightarrow 2), \quad (3.4)$$

where A and B are the task-oriented sets of parameters, and Ω represents the shared parameters. The right-hand side of (3.4) is thus symmetric in the outputs: all sets of parameters are used to ensure the optimal prediction of Y_1 and Y_2 . In turn, maximising the likelihood of Y_2 , helps to maximise of the likelihood of Y_1 , and viceversa. The procedure can be generalised to an arbitrary number of outputs by summing over all permutations in the right-hand side of the identity. Therefore, uncorrelated tasks would work against each other, resulting in worse performance. In what follows, we choose to use the concentration of the analyte as the principal prediction of the network, and the integral intensities of the associated emission lines or bands as secondary outputs of the network. In turn, this helps to stabilise the model and increase its robustness during inference. It also provides a set of secondary results used to validate the performance of the model and to detect anomalies, as described in Section 5.2.3. Notice that the prediction of the maximal intensity of the emission lines may result in an easy task for the network. As a consequence, the network may be imbalanced with respect to the prediction of the concentration of the analyte, which requires non-trivial computations. For this reason, we use integral intensities in the effort to complicate the secondary tasks. We also implement a specific training strategy, described in Section 4.6.3.

3.3 Trustworthiness of the Model Via Validation of the Predictions

The evaluation of the performance of any model is always possible in the training and development sets, by comparing the predictions of the model with the corresponding known ground truths. However, the validation of the predictions on new data and the detection of anomalies remain complicated issues. In this implementation, given the mutual dependence of the multiple outputs of the MT architecture, we rely on the set of secondary outputs of the model to assess its performance on unknown data. As seen previously, good predictions on sub-tasks related to the principal output concur to improve its stability and overall results. Conversely, a bad performance on the secondary tasks leads to poor predictions on the principal output. This is especially true if the sample matrix significantly changes in the inference set or following a modification in the experimental conditions. For this reason, the set of sub-tasks chosen in this analysis is experimentally measurable on unknown samples. In fact, the integral intensities of emission lines or bands can be extracted from experimental spectra at any given time, even though the concentration of the analyte remains unknown. In turn, this can be used to assess the trustworthiness of the predictions of the model.

When dealing with new experimental data, we compute the predictions of the model on a single spectrum basis, independently. We then average the results per sample, to smooth the influence of defects on the surface. This procedure allows us to use standard frequentist statistical tests to compare the results to ground truths. The Mean Absolute Percentage Error (MAPE) gives a measure of the deviation of the data and the performance of the model. For the i -th secondary output of the network and a sample s , we compute the MAPE $M_i^{(s)}$ of the predicted intensities $\mathbf{I}_i^{(s)} \in \mathbb{R}^n$ and the corresponding ground truths $\widehat{\mathbf{I}}_i^{(s)} \in \mathbb{R}^n$, with n samples:

$$M_i^{(s)} \stackrel{\text{def}}{=} \mathbb{E} \left[\left| \frac{\mathbf{I}_i^{(s)} - \widehat{\mathbf{I}}_i^{(s)}}{\widehat{\mathbf{I}}_i^{(s)}} \right| \right]. \quad (3.5)$$

This offers a first estimate of the error made by the model, independent of the variance of its predictions: it describes the trueness of the model in predicting a given quantity. We use this value as a first step in the analysis of the trustworthiness of the predictions. For instance, a larger MAPE on the secondary outputs is an indication of worse performance of the model or anomalies, which could reflect on the main prediction. In order to estimate a soft threshold for the quantity, we use the validation set V . We compute a confidence interval around the MAPE $M_i^{(s)}$ of a sample $s \in V$ for the i -th secondary output:

$$\left[M_i^{(s)} - \widehat{t}_{1-\alpha}^n \frac{\sigma_i^{(s)}}{\sqrt{n}}, M_i^{(s)} + \widehat{t}_{1-\alpha}^n \frac{\sigma_i^{(s)}}{\sqrt{n}} \right], \quad (3.6)$$

where

$$\left(\sigma_i^{(s)} \right)^2 = \mathbb{E} \left[\left| \frac{\mathbf{I}_i^{(s)} - \widehat{\mathbf{I}}_i^{(s)}}{\widehat{\mathbf{I}}_i^{(s)}} \right|^2 \right] - \left(M_i^{(s)} \right)^2 = \text{Var} \left(\left| \frac{\mathbf{I}_i^{(s)} - \widehat{\mathbf{I}}_i^{(s)}}{\widehat{\mathbf{I}}_i^{(s)}} \right| \right), \quad (3.7)$$

and $\widehat{t}_{1-\alpha}^v$ is the value of the *Student's t* variable for v degrees of freedom (the number of spectra for each sample), at a confidence level $1 - \alpha$.

A second analysis is based on a Student test on the predicted intensity, given its nature of repeated measurement on the sample. Supposing that the ground truth value of a sample s for the i -th average intensity has a sample variance σ_i^2 , we can compute the random variable

$$t_i^{(s)} \stackrel{\text{def}}{=} \frac{\left| \mathbb{E} \left[\mathbf{I}_i^{(s)} \right] - \mathbb{E} \left[\widehat{\mathbf{I}}_i^{(s)} \right] \right|}{\sqrt{\widehat{\Sigma}_i^2 + \sigma_i^2}}, \quad (3.8)$$

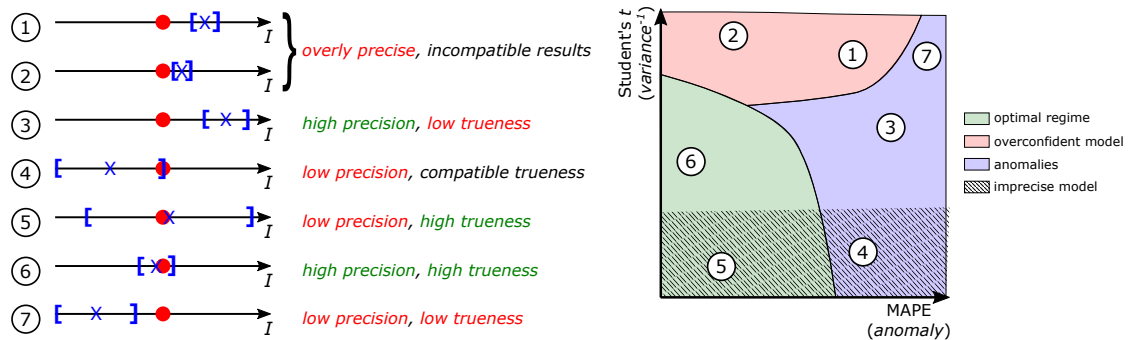


Figure 3.6. Interpretation of the trustworthiness assessment results. *MAPE* and *Student's t* are used as measure of the confidence of the predictions, with possible outcomes summarised on the left of the figure. Interpretations of these results are presented schematically on the right.

where Σ_i^2 is the sample variance of the predictions. By including the dependence on the variance, this test gives a statistical measure of the ability of the MT model to generalise to unknown data. In order to discriminate possible anomalies, we can use a standard approach by choosing a threshold value $\hat{t}_{1-\frac{\alpha}{2}}^n$ of a two-tailed t -test at confidence level $1 - \alpha$, with n degrees of freedom, such that the probability $P\left(t_i^{(s)} \geq \hat{t}_{1-\frac{\alpha}{2}}^n\right) = \alpha$. Unknown samples can be compared to validation standards according to the compatibility of their principal outputs. This way, we recover a probabilistic interpretation of the result in terms of confidence: models can be compared based on their performance at different values of α on the secondary outputs.

The values of *MAPE* and of the *Student's t* variable can be used together to evaluate the trustworthiness of the model and characterise its predictions. For instance, large *MAPE* and low t values may be an indication of the model ability to extrapolate the results for out-of-distribution samples or an anomaly, though with high variance. In other words, the prediction is compatible with the ground truth, though not precise. Conversely, small values of *MAPE* and large t values can be interpreted as anomalies in training, leading to an artificially good prediction, whose variance is too small to explain the variability of the data. Hence, in this case, the prediction is close to the ground truth, though not compatible with the real value. We graphically summarise these interpretations in the plane in Figure 3.6. Though the confidence level of the principal output is not easily computed from the confidence of the secondary outputs, this measure gives an implicit feedback on the main output. Given the dependencies of the MT parameters in Section 3.2, the information determines whether the prediction of the concentration of the analyte is trustworthy.

4 Implementation and Experimental Details

In this section, we describe experimental methods. We also present the details of the MT model based on CNNs used in the analysis. We then highlight the differences with the univariate Linear Regression (LR) and multivariate algorithms such as Multi-Linear Regression (MLR), Partial Least Squares (PLS1), and Fully Connected Neural Networks (FCNNs).

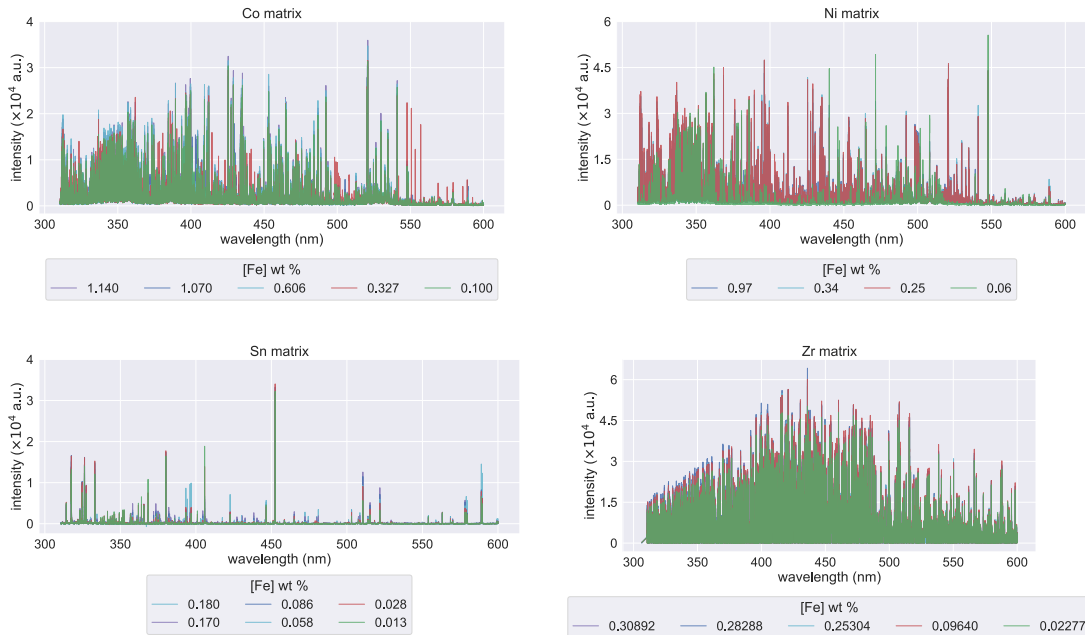


Figure 4.1. Average spectra of the selected alloy matrices. *This selection allows displaying different degrees of noise and spectral interference at different concentration levels of the analyte.*

4.1 Experimental Setup

We compare the predictive ability of different algorithms on two types of datasets. We consider 19 cement samples, whose elemental compositions are reported in Table A.1 in Appendix A, and on 6 alloy matrices with 4 to 6 samples each, summarised in Tables A.2 and A.3 in Appendix A. The first were built in the framework of an interlaboratory comparison in 2021 [53] by the *Bundesanstalt für Materialforschung und -prüfung* (BAM) in Berlin, Germany. All measurements were carried out in air, at room temperature.

Data on alloys were collected using a Nd:YAG laser (*Quantel Ultra*) operating at a wavelength of 266 nm, 6 mJ pulse energy, and 4 ns pulse length. The plasma emission was analysed with a *LTB Aryelle 400* spectrometer with a fixed aperture of $50 \mu\text{m} \times 50 \mu\text{m}$, equipped with an *Andor DH740* ICCD, in the range 310 nm to 613 nm (resolving power: $\lambda/\Delta\lambda \simeq 1.8 \times 10^4$). We used a gate delay of 1 μs and a gate width of 0.5 μs . For each sample, 25 spectra were collected, accumulating 20 laser shots for per crater. The irradiance on the surface of the samples was 76 GW cm^{-2} . A selection of average spectra is shown in Figure 4.1 (see Figure D.5 in Appendix D for the other matrices).

Cement samples, whose average spectra are shown in Figure 4.2, were probed using a Nd:YAG laser (*Quantel Brio*) at a wavelength of 1064 nm, 15 mJ pulse energy and 4 ns pulse length. For each sample, 25 spectra were collected, accumulating 40 laser shots (5 pre-ablation shots). We used a *Mechelle* spectrometer with an *Andor iStar* ICCD and a fixed aperture of $50 \mu\text{m} \times 50 \mu\text{m}$, 10 μs gate delay, and 100 μs gate width in the range 200 nm to 975 nm (resolving power $\lambda/\Delta\lambda \simeq 4 \times 10^3$ measured at 589.60 nm on a Na peak). The irradiance on the sample surface was 190 GW cm^{-2} .

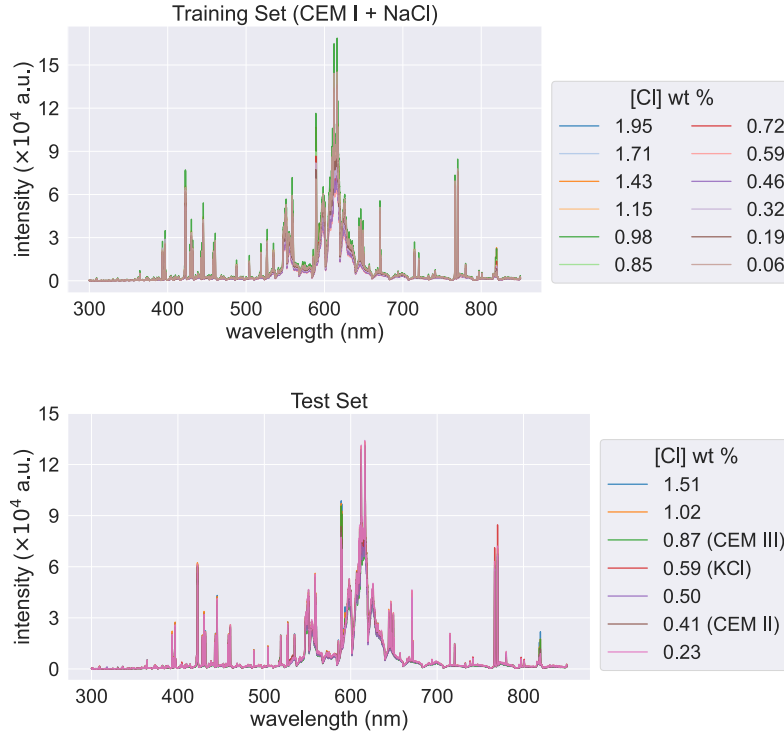


Figure 4.2. Average spectra of the cement samples. Spectra are separated into training and test sets. Samples were fabricated using CEM I, with the addition of NaCl, unless otherwise stated.

4.2 Secondary Outputs

As the prediction of a peak intensity may result in simple secondary tasks for the NNS, we use integral intensities on a neighbourhood of wavelength channels to complicate the computation. Other strategies are also employed to solve the possible issue, though they are discussed in Section 4.6.3, when we introduce the architecture and the training procedure. Notice that these secondary outputs of the MT architecture are considered to be the inputs in the MLR and FCNNs for this analysis.

For the analysis of the alloy matrices, we use the intensities of the most intense persistent lines of Fe in the spectral range considered, integrated over 10 wavelength channels. Specifically, we choose 8 lines, reported in Table B.1 in Appendix B. For the cement samples, we consider two molecular bands centred at 593.46 nm and 617.74 nm, and integrated over 14 channels in the intervals 593.20 nm to 593.64 nm and 617.47 nm to 617.93 nm. As a general guideline, choosing a large number of secondary outputs helps the convergence of the network, and preserves a good generalisation performance of the model. Moreover, since the CNN architecture of the MT model is sufficiently versatile, there is no need for an accurate selection of the emission lines.

4.3 Train and Test Sets Selection

In the case of alloy matrices, given the small number of samples available, 30% of the spectra for each sample is retained as independent test set, while the rest is used as training set for the

baseline models, and as input of the data augmentation for the MT architecture. This ensures, on average, an in-sample inference for the algorithms (the selection of test samples comes from the same samples in the training set). Moreover, it provides the means to verify whether the augmentation technique correctly enhances the training distribution. Notice that this does not automatically translate into a simpler task for the model: spectra in the test set may still differ from the training distribution, due to random and local fluctuations, thus they may represent out-of-distribution data on a spectrum basis.

Differently, cement matrices are separated into training and test sets on a sample basis: 12 matrices are considered as calibration set, while 7 samples are used for inference. In the test set, we insert specifically samples which present a different matrix (type of cement) or manufacturing procedure (different salts added in the mixture) in order to check the out-of-distribution generalisation ability of the algorithms (see Table A.1 in Appendix A for details), and their ability to recognise possible anomalies.

For LR and MLR, no additional validation sets have been considered, as no free parameters are present in the algorithms: for these baselines, we do not introduce lasso or ridge regularisations, thus no hyperparameter optimisation procedures are necessary. For PLS1, we perform a cross-validation procedure (5-fold, chosen to optimise the number of spectra in each permutation of the data and the computation wall time) to determine the best number of components to retain. However, in the case of NNS, both FCNN and MT CNN, several hyperparameters (number of hidden layers, number of units, size of the convolutional kernels, etc.) are considered. Given the time consuming operations involved, we use a single holdout validation set made of 20 % of the spectra contained in the training set, selected using a stratified strategy to preserve the fraction of spectra for each sample. Notice that, in the case of the data-augmented training, we provide the results for different sizes of the training set, namely 100, 1000, 5000 and 10 000 synthetic spectra for each experimental sample. In this case, the validation set is chosen from the synthetic data: in order to avoid any data leakage, we avoid using the experimental spectra when optimising the model. Results always refer to the independent experimental test set.

4.4 Preprocessing

We first remove peripheral zones by reducing the spectra of the alloy matrices to the interval 310 nm to 600 nm, and the cement spectra in the range 300 nm to 850 nm. This sets the number of wavelength channels in the range 67 829 to 68 438 in the first case, and to 16 917 in the second.

Outliers are then removed from the training set, either experimental or synthetic: in our analysis, at a given wavelength, outliers are spectra which present an intensity outside the interval between the 5th and 95th percentile of the values. The goal is to build performing calibration models without using extreme configurations. In order to test the generalisation ability of the models, we retain the outliers in the test set. For the alloy samples, we focus on the Fe line at 373.49 nm (the most intense persistent line), while, for the cement matrices, we consider the molecular band of CaCl at 593.46 nm.

Finally, spectra are normalised using the integral intensity at a given wavelength. Since the procedure is performed independently on each spectrum, we can also safely normalise the spectra in the test sets. For the alloy matrices, we consider the integrated intensity of the most intense emission line of the matrix itself over an interval of 10 wavelength channels (emission lines and corresponding integration intervals are reported in Table B.2 in Appendix B). The cement samples have been normalised to the intensity of the CaO molecular band at 615.03 nm, integrated over 20 wavelength channels in the interval 614.66 nm to 615.38 nm.

4.5 Evaluation Metrics

In the framework of the analysis, different evaluation metrics are used to assess the performance of the models on their predictions. In order to obtain comparable results, we adopt the same metrics and strategy for the univariate and multivariate analyses. We use common regression metrics such as the Mean Squared Error (MSE, also expressed in the same units as the predictions by its square root, the Root Mean Squared Error, or RMSE), the Mean Absolute Error (MAE), and the MAPE to score the results of the algorithms. We provide the results of the algorithms on the independent test set, made of experimental spectra, unless otherwise specified.

4.6 Training and Optimisation Strategies

Depending on the algorithms used for the analysis, we use different training techniques and representations of the input data. We also define different optimisation strategies, in order to fix the optimal hyperparameters of the models, used for inference.

4.6.1 Input Representation

In the case of LR, we consider the integral intensity of selected wavelength channels as inputs of the model. Specifically, we consider the integral intensity of the Fe emission line at 373.49 nm, integrated over 10 wavelength channels, for the alloy matrices. For the cement samples, we use the CaCl molecular band at 593.46 nm, integrated over 14 channels. As already stated at the end of Section 4.2, for the MLR and the FCNN, we select several atomic Fe emission lines as inputs, in the case of the alloy matrices. We use the CaCl molecular bands at 593.46 nm and 617.74 nm for the cement samples. In both cases, they are the same variables used as secondary outputs by the MT model. On the other hand, for PLS1 and the MT network, we use the entire spectra as input. Finally, we choose a quadratic regression model in the case LR (without interaction terms), while we consider a simple regression model for MLR.

4.6.2 Fully Connected Neural Networks

In the case of fully connected networks, we consider a simple architecture, described in detail in Section 4.7.1, with a traditional MSE loss function. We introduce both ℓ_1 and ℓ_2 regularisations for the parameters of the network. The latter is defined both independently and as weight decay [54] in the gradient descent optimiser. The global loss function is, thus:

$$\mathcal{L}_{\text{glob}}(\mathbf{y}, \hat{\mathbf{y}}; \Omega; \alpha, \beta) = \mathbb{E} \left[(\hat{\mathbf{y}} - \mathbf{y})^2 \right] + \alpha \mathcal{L}_1(\Omega) + \beta \mathcal{L}_2(\Omega), \quad (4.1)$$

where $\mathcal{L}_p(\Omega) = \sqrt[p]{\sum_{\omega \in \Omega} |\omega|^p}$ is the ℓ_p norm of the set of parameters of the network Ω . In the expression of the loss, \mathbf{y} and $\hat{\mathbf{y}}$ represent the ground truth values and their predictions. The two hyperparameters α and β control the entity of the penalties. The learning objective is thus a convex optimisation problem, in principle freeing training from weight initialisation issues. We use the ADAMW optimiser [54], which has been shown to grant better generalisation abilities with respect to other implementations (e.g. the traditional ADAM algorithm [55]). We leave the default hyperparameters β_1 and β_2 in its definition, and an initial learning rate defined by the optimisation.

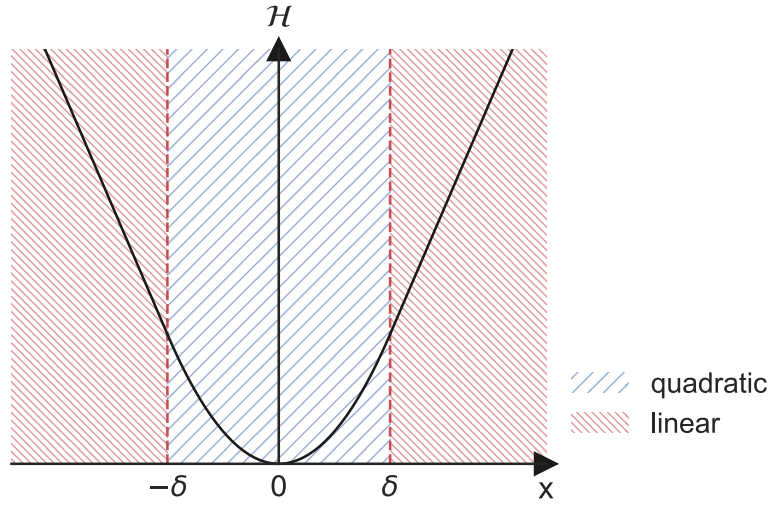


Figure 4.3. Huber loss function. *The Huber loss is a continuous interpolation of a quadratic curve with a linear behaviour, due to the presence of the hyperparameter δ .*

4.6.3 Multitask Architectures

The MT loss presents additional peculiarities, with respect to the previous case:

$$\mathcal{L}_{\text{MT}}(\mathbf{Y}, \hat{\mathbf{Y}}; \Omega; \mathbf{v}, \alpha, \beta) = \mathbf{v} \cdot \mathbf{L}(\mathbf{Y}, \hat{\mathbf{Y}}; \Omega) + \alpha \mathcal{L}_1(\Omega) + \beta \mathcal{L}_2(\Omega). \quad (4.2)$$

The vector $\mathbf{L}(\mathbf{Y}, \hat{\mathbf{Y}}; \Omega) \in \mathbb{R}^p$ contains the losses of each prediction output. With this notation, $\mathbf{Y} \in \mathbb{R}^{n \times h}$ and $\hat{\mathbf{Y}} \in \mathbb{R}^{n \times h}$ are matrix representations of the ground truths and their predictions, respectively, where h is the number of outputs of the model.

In this formulation, \mathbf{v} , β and γ are hyperparameters of the model. As we deal with the multiple outputs of the network, $\mathbf{v} \in \mathbb{R}^h$ is the vector of coefficients of the linear combination of single-output loss functions. In this article, we adopt the strategy to weight equally the secondary outputs, and to perform an adaptive adjustment of the scalar weight \hat{v} of the principal output. In particular, we start the learning process with a coefficient $0 < \hat{v}_0 < 1$ for the main output. After each epoch t (full iteration of the training dataset), we implement an exponential decrease of the learning coefficient $\hat{v}_{t+1} = \eta \hat{v}_t$. Secondary outputs are all weighted by a factor $1 - \hat{v}_t$. In other words, we consider the hyperparameter vector $\mathbf{v}_t = (\hat{v}_t, (1 - \hat{v}_t)\mathbf{1}_{h-1})$ for each epoch t , where $\mathbf{1}_d$ is a d -dimensional unit vector. Both \hat{v}_0 and $0 < \eta < 1$ are subject to hyperparameter optimisation. The result is an algorithm capable of first learning the most difficult output (usually, the concentration of the analyte), and then fine-tuning on the simpler predictions (the integral intensities of the emission).

We adopt the MSE loss function for the secondary outputs of the MT architecture. However, for the main output (the concentration of the analyte), we introduce a *Huber* loss [56] to ease the learning of the principal output. Such loss function is defined as:

$$\mathcal{H}(\mathbf{y}, \hat{\mathbf{y}}; \delta) = \begin{cases} \frac{1}{2} \mathbb{E} [(\hat{\mathbf{y}} - \mathbf{y})^2] & \text{if } |\hat{\mathbf{y}} - \mathbf{y}| < \delta \\ \delta \mathbb{E} [|\hat{\mathbf{y}} - \mathbf{y}| - \frac{\delta}{2}] & \text{if } |\hat{\mathbf{y}} - \mathbf{y}| \geq \delta \end{cases}. \quad (4.3)$$

This formulation is a continuous and differentiable interpolation between a quadratic (MSE) and linear (MAE) loss, depending on the value of a hyperparameter δ (see Figure 4.3). The loss is less sensitive to outliers, given its linear behaviour for deviations greater than δ . It collapses to the MSE for $\delta = 0$.

As in the FCNNs case, we use the ADAMW optimiser with default hyperparameters. The initial learning rate is defined during the optimisation. When dealing with different numbers of spectra in the simulated training sets, we adjust the mini-batch size of the stochastic gradient descent to fit learning needs and GPU memory. When the mini-batch size is modified by a given multiplicative factor, we also scale the learning rate of the same factor, to improve the chances of convergence. We also implement an exponential learning rate scheduling: after each training epoch t , the learning rate q_t is multiplied by a factor $0 < \varphi < 1$ as $q_{t+1} = \varphi q_t$.

4.6.4 Hyperparameter Optimisation Strategy

In the case of the LR and MLR, no optimisation is required, hence no validation dataset is used in those cases. Training is directly performed on the dedicated set, before computing the final predictions on the test set. For PLS1, we optimise the number of components used to infer the results. We build a 5-fold cross-validation strategy in order to seek the best hyperparameter. We use a grid search approach (see Table B.3 in Appendix B for the number of components used in the PLS1 models). Differently, in the case of NNS, we use a separate holdout validation set for the development of the models. We train several models in parallel with different hyperparameters, and we retain the architecture with highest evaluation score on the validation set. For both experimental datasets, we use the MSE on the validation set of the predicted concentrations as scalar metric to evaluate the best model.

The values of the hyperparameters are sampled using a tree-structured *Parzen* estimator [57]. It enables to use Gaussian mixtures to evaluate the posterior distribution of the hyperparameters, making the optimisation easier. We run 200 cycles of optimisation of at most 200 epochs. In all cases, an early stopping strategy is employed where no improvement on the validation loss occurred for at least 100 epochs. Given the different nature of the data, we optimise the FCNN and the MT architecture independently for the alloy and cement matrices. However, for metallic samples, we run the full optimisation only on the Al matrix, for simplicity. For the MT network, we run the optimisation cycle on synthetic data: we optimise the architecture for 5000 synthetic spectra per sample, and a noise parameter $\beta = 0.05$. We fix the mini-batch size to 128. Once the hyperparameter are chosen, we separately re-train the best model for different sizes of the simulated training sets and noise parameters.

4.6.5 Training of the Neural Networks

We train the FCNN for 1000 epochs, with an early stopping after 500 epochs without improvements on the validation loss, and a mini-batch size of 4 spectra. The MT networks are trained for 500 epochs, with an early stopping after 250 epochs without improvements on the validation loss. In this case, we choose to adjust the mini-batch size to 16, 32, 64 and 128 spectra when working with 100, 1000, 5000 and 10 000 simulated spectra per sample.

4.7 Neural Network Architectures

In this analysis, we use two different kinds of networks: a classical FCNN as baseline, and a MT CNN. In this section, we detail the implementation of these architectures as used in the analysis of the LIBS data.

4.7.1 Fully Connected Neural Networks

The first architecture we consider is a simple multi-layered perceptron [58] with a single output unit. The n -th layer in the architecture computes:

$$\mathbf{x}^{(n+1)} = \mathcal{B}\left(f\left(\mathcal{D}_r\left(\mathbf{x}^{(n)} \cdot \mathbf{W}^{(n+1)} + \mathbf{b}^{(n+1)}\right)\right)\right), \quad (4.4)$$

where $\mathbf{x}^{(n)} \in \mathbb{R}^p$ is the input vector and $\mathbf{x}^{(n+1)} \in \mathbb{R}^q$ is the activated output. In the expression, $\mathbf{W}^{(n+1)} \in \mathbb{R}^{p \times q}$ and $\mathbf{b}^{(n+1)} \in \mathbb{R}^q$ are the weight and bias of the n -th layer. A dropout operation \mathcal{D}_r with rate $0 \leq r < 1$ is used as regularisation strategy. Finally, f is the activation function. The function \mathcal{B} is a batch normalisation (BN) operation [59], used to accelerate the convergence of the network. That is, for each mini-batch $\{\mathbf{z}_i \in \mathbb{R}^p, i = 1, 2, \dots, B\}$ of data in the gradient descent, the inputs are rescaled:

$$\hat{\mathbf{z}}_i = \frac{\mathbf{z}_i - \boldsymbol{\mu}_B}{\sigma_B}, \quad i = 1, 2, \dots, B, \quad (4.5)$$

where

$$\boldsymbol{\mu}_B = \frac{1}{B-1} \sum_{i=1}^B \mathbf{z}_i, \quad \sigma_B^2 = \frac{1}{B-1} \sum_{i=1}^B (\mathbf{z}_i - \boldsymbol{\mu}_B)^2 \quad (4.6)$$

are the empirical mean and variance of the mini-batch. BN is defined as:

$$\text{BN}_{\beta, \gamma} : \mathbb{R}^{B \times p} \rightarrow \mathbb{R}^{B \times p} \\ \mathbf{Z} \mapsto \text{BN}_{\beta, \gamma}(\mathbf{Z}), \quad (4.7)$$

where

$$\text{BN}_{\beta, \gamma}(\mathbf{Z}) = \gamma \hat{\mathbf{Z}} + \beta. \quad (4.8)$$

In the last equation, γ and β are learnable parameters of the network. Other than speeding up training, BN can also restrict the growth the values of the activated outputs of the layers, thus making it easier to train complex models.

For the analysis of the alloy matrices, the network contains 4 hidden layers with 136, 56, 328 and 392 units, respectively. The dropout rate is 0.23. The activation function used in the architecture is a leaky *REctified Linear Unit* (ReLU) with a slope $\alpha = 0.03$. Defined as $z \mapsto \max(z, \alpha z)$, it becomes a simple ReLU for $\alpha = 0$, as in Figure 4.4. The initial learning rate is 10^{-3} , and the weight decay is 3×10^{-2} . In the case of cement samples, the network has 2 hidden layers with 424 and 152 units. The dropout rate is fixed to 0.17. The activation function is, again, a leaky ReLU with a slope of 5.5×10^{-2} . For both types of experimental dataset, the optimisation procedure leads to vanishing hyperparameters for ℓ_1 and ℓ_2 regularisations.

4.7.2 Multitask Neural Networks

The multitask architecture is fundamentally built on strided convolution operations. Given two vectors $\mathbf{x} \in \mathbb{R}^p$ and $\mathbf{v} \in \mathbb{R}^k$, and an integer *stride* s , the operation can be written in components:

$$(\mathbf{x} *_s \mathbf{v})_i = \sum_{n=0}^{k-1} x_{i-s+n} v_n, \quad i = 1, 2, \dots, q, \quad q = \left\lfloor 1 + \frac{p-k}{s} \right\rfloor. \quad (4.9)$$

The n -th convolutional layer, thus computes:

$$\mathbf{x}^{(n+1)} = f\left(\mathcal{D}_r\left(\mathcal{B}\left(\mathbf{x}^{(n)} *_s \mathbf{v}^{(n+1)} + \mathbf{b}^{(n+1)}\right)\right)\right), \quad (4.10)$$

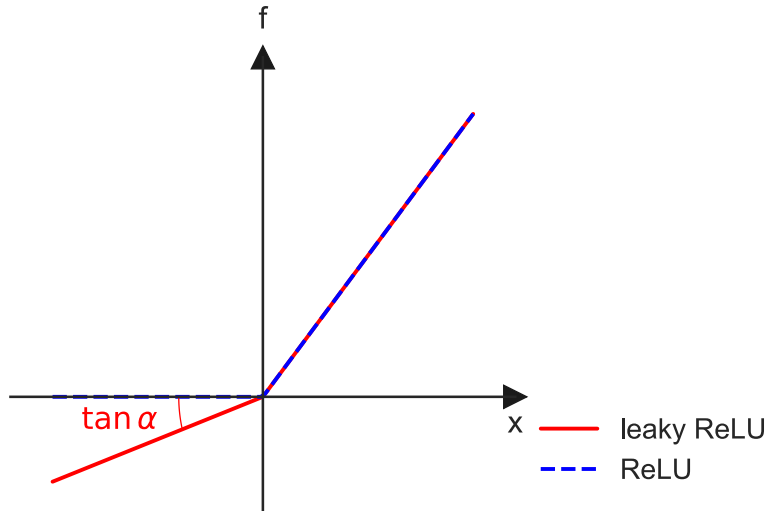


Figure 4.4. Leaky ReLU activation. Differently from the usual ReLU function, the hyperparameter α of the leaky ReLU represents its negative slope.

where $\mathbf{v}^{(n+1)}$ and $\mathbf{b}^{(n+1)} \in \mathbb{R}^q$ are learnable parameters of the n -th layer. We do not use pooling layers, since, in the case of spectral, they may result in the loss of relevant information among neighbouring wavelength channels (as also pointed out in [15]).

In the case of the alloy matrices, the shared representation network contains 3 convolutional layers, while the task-specific networks present 4 convolutional and 1 fully connected layer. The strides are particularly wide, in order to reduce significantly the size of the outputs of the layers. In this case, BN was used throughout the architecture, to contain the values of the activations. In the implementation, a ℓ_2 regularisation loss was also added to constrain the growth of the free parameters.

For the cement samples, the shared representation is the result of 2 convolutional layers. The task-specific networks are made of 3 hidden convolutional layers. Only the heads of the network use BN operations. The final regressor networks are made of a single hidden layer. All layers present a dropout operation, and the activations vary between pure ReLU and leaky ReLU.

For both architectures, different values of the initial learning rate are also used. We also notice that the optimisation procedure eventually chooses $\delta = 0$ in the loss function, thus opting for a classical MSE loss, to assign a stronger penalty to the possibly remaining outliers. The full list of hyperparameters is available in Table B.4.

4.8 Software and Hardware Setups

For the analysis, we use the Python libraries *Scikit-learn* [60] and *PyTorch* [61] (and its wrapper *Pytorch Lightning* [62]) for the development of shallow and DL algorithms, respectively. *NumPy* [63] is used for the synthesis of artificial data. We choose *Optuna* [64] for the optimisation of the hyperparameters of the networks. Computations of linear models and FCNNs are performed on a laptop with 32 GB RAM and Intel[®] Core[™] i7-10875H CPU and a NVidia[®] Quadro T2000 GPU with 4 GB GDDR6 memory. The optimisation and training of the MT architecture are performed in parallel on NVidia[®] V100 cards with 16 GB or 32 GB HBM2 memory, and NVidia[®] P5000 cards

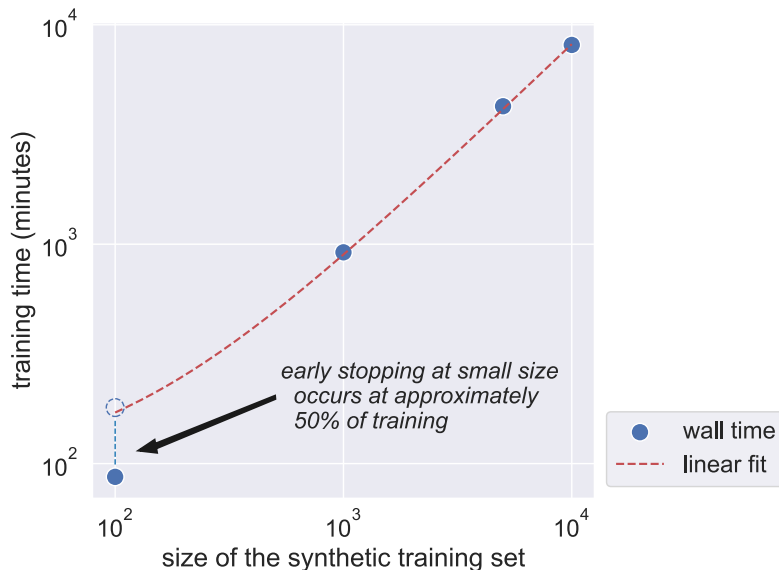


Figure 4.5. Wall time of the training process. *At the smallest synthetic set size, the training is interrupted halfway through the complete training, due to the early stopping strategy. Accounting for this effect leads to a linear relation between size of the training set and training time.*

with 16 GB GDDR5X memory. The setup is able to provide virtually immediate results for the shallow ML algorithms. The optimisation cycle of the FCNNs usually takes a few hours to complete (approximately 9 hours for each dataset we consider in the analysis, using up to 4 GPUs in parallel). Training takes less than an hour (approximately 45 minutes) for each matrix. On the other hand, the MT architecture is longer to train, though not dramatically more involved. The hyperparameter optimisation takes a few days, depending on the number of cycles and the size of the search space (4.5 days in our case, 4 GPU cards in parallel). Training on a longer number of epochs takes hours to days to complete, as shown schematically in Figure 4.5 (the average training time between different experimental matrices has been considered). Notice that the training wall time scales linearly with the size of the training set, as expected (early stopping must be taken into account). Computations were carried out using a private infrastructure, namely the *FactoryIA* supercomputer, located in the Île-de-France region in France, with a carbon efficiency of 0.1 kgCO₂eq/kWh (national average). Considering only the most power consuming card and the MT model (NVidia[®] V100 32 GB consumes up to 300 W), we estimate the cost of optimisation to 13 kgCO₂eq, separately for the cement samples and the alloy matrices. Training simultaneously on the different sizes of the synthetic training set impacted for approximately 7 kgCO₂eq for each experimental matrix [65], approximately equivalent to 120 km driven by an average petrol-powered passenger vehicle [66]. Experiments repeated during several months, amounting to several return journeys from Paris, France, to Turin, Italy ($2 \times 800 \text{ km} = 1600 \text{ km}$). Some specific LIBS applications (e.g. inference on a simple matrix) may require smaller MT models. In this case, less synthetic spectra are needed, thus making the analysis feasible even on less performing hardware. On the other hand, once the architecture is trained, predictions are very fast to compute (from less than a second to a few seconds, depending on size of the batch of spectra). Models can thus be easily deployed and used for online inference.

5 Results and Discussion

In what follows, we compare the results of the different analysis techniques on the experimental matrices. We first introduce the predictions made by the shallow ML algorithms and the FCNNs. We then discuss in detail the MT architecture, and the aspect of validation of its predictions.

5.1 Baseline Analysis

In the analysis, we consider different types of baselines, in order to provide a complete comparison of the proposed technique with the SOTA. Specifically, we show the results of PLS₁, which does not require the extraction of information from the experimental spectra. Differently, models such as LR, MLR and FCNNs need *a priori* knowledge of the spectra and a screening process to extract the integral intensities used for training. Similarly to the first, our proposed MT model does not require expertise in selecting input data, since the important variables are learnt during training. It requires a degree knowledge of the emission lines of the analyte to choose the secondary outputs. However, as the addition of several outputs to the network is, in principle, always beneficial (see Section 3.2), there is no need for an accurate selection of these lines. A simple choice is to consider the full set of persistent lines of the analyte in the spectral range available, since spectral interference on single lines (or bands) is taken care of by the CNN architecture.

For the comparison with the MT model, we group the results of LR, MLR and FCNNs into a single *ensemble* meta-model, based on the RMSE of the predictions. For these algorithms, we only display the best result among the three of them in the main text. We refer to Appendix C for the separate results. Details on the traditional analysis on experimental data are given in Section 5.1.1, where we also provide the results of the baseline algorithms on synthetic data. We also include the results of the MT model on experimental data, without synthetic data augmentation in Section 5.1.2, as a separate term of comparison with other algorithms.

5.1.1 Traditional Algorithms

As shown in Table C.1 in Appendix C, FCNNs seem to be more versatile, and provide, in general, the best generalisation results, with respect to the linear models used as baselines. Simpler algorithms, such as LR or MLR, struggle at very low concentrations of the analyte, displaying error fractions which can reach and surpass the unit. As expected, the linear models also present a typical heteroscedastic behaviour, with uncertainties which tend to proportionally decrease at higher concentrations of the analyte. Globally, the PLS₁ model presents larger uncertainties, with respect to previous models. However, in some cases, the implicit dimensionality reduction of the algorithm, helps in partially solving the spectral interference in the data, and provides good results. As already anticipated, these results are summarised in a meta-model, which therefore displays different behaviours on the entire range of variation of the concentration of the analyte.

In Table C.2 in Appendix C, we show the results of the classical algorithms on synthetic data, for comparison with MT learning. In this case, we simply replace the experimental training set with a synthetically generated dataset, made of 1000 spectra per sample for the alloy matrices, and 100 spectra for each cement sample. We notice that linear models are, in general, only slightly affected by the presence of synthetic data. Uncertainties computed at different sizes of the training set are compatible with those found using only the experimental data. As predictable, the FCNNs behave differently: more complicated matrices, with strong differences between samples, such as Al, Co and Zr, show an improvement. However, matrices in the presence of strongly interfered emission lines, often show a decrease in performance, when comparing *a posteriori* the predictions of the concentration of the analyte. This is most probably due to

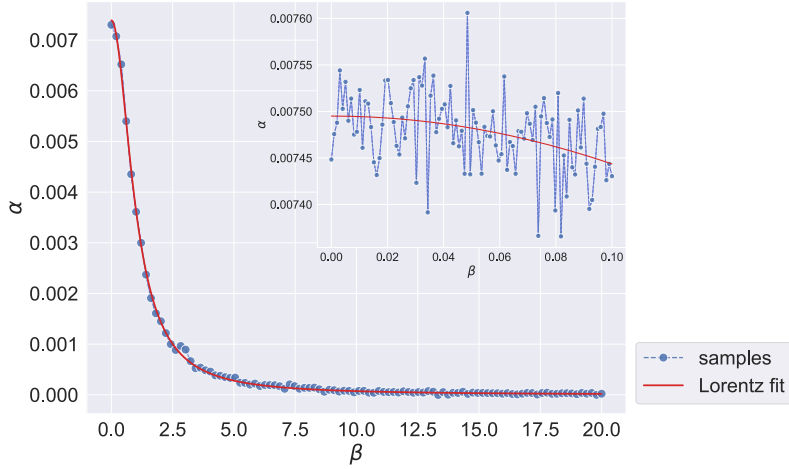


Figure 5.1. Regression coefficient as a function of the noise parameter. *The large plot represents the functional behaviour of the parameter α as a function of the confounder β . The inset plot shows the same behaviour for the explored values of β : modifications are relevant starting from the fourth significant figure.*

the size of the model not being able to account for all local variations in the training distribution to ensure a good generalisation to unknown data. In the case of cement samples, no significant differences are registered.

For the traditional algorithms, we also performed a scan in the β parameter at different sizes of the training set. For the values explored, the results of the linear models do not vary as functions of the intensity of the noise. This can be seen by considering, without loss of generality, a simple regression model $y_i = \alpha x_i + \varepsilon$ with predictions \hat{y}_i , where $i = 1, 2, \dots, N$ and $\varepsilon \sim \mathcal{N}(0, 1)$ and $x_i, y_i \in \mathbb{R}$. We have

$$\alpha \left(\frac{1}{N} \sum_{i=1}^N x_i^2 - \bar{x}^2 \right) - \frac{1}{N} \sum_{i=1}^N x_i \hat{y}_i - \bar{x} \bar{y} = 0, \quad (5.1)$$

where

$$\bar{x} = \frac{1}{N} \sum_{i=1}^N x_i, \quad \bar{y} = \frac{1}{N} \sum_{i=1}^N \hat{y}_i. \quad (5.2)$$

In our implementation of the synthetic data augmentation, the role of the predictor x_i is represented by the intensity of the emission $x_i \stackrel{\text{def}}{=} I_i = z_i p_i$, where $z_i \sim \mathcal{N}(1, \beta)$ and $p_i \sim \mathcal{P}(\bar{I})$ as in (3.3) (\bar{I} is expressed as a pure number in arbitrary units). The dependent variable y_i is the concentration C_i of the analyte. From (5.2), the parameter α shows a dependence

$$\alpha \propto \frac{1}{(1 + \beta^2)(1 + \bar{I})\bar{I} - \bar{I}^2} \propto \frac{1}{1 + (1 + \bar{I})\beta^2}, \quad (5.3)$$

since

$$\begin{aligned} \frac{1}{N} \sum_{i=1}^N x_i^2 &= \mathbb{E} [z_i^2] \mathbb{E} [p_i^2] \\ &= \left(\mathbb{E} [z_i]^2 + \text{Var} (z_i) \right) (\mathbb{E} [p_i] + \mathbb{E} [p_i(p_i - 1)]) \\ &= (1 + \beta^2) (1 + \bar{I}) \bar{I}. \end{aligned} \tag{5.4}$$

Hence, the intensity of the noise β directly influences the learning of the parameter α , which follows a Lorentzian profile. The procedure can be generalised to MLR or more complex models, with the same principle. In Figure 5.1, we show a simulation on synthetic data, generated as in the analysis: the fit shows the Lorentz-like behaviour of the type

$$\alpha = \frac{a}{b + \beta^2} = \frac{a}{b} - \frac{a}{b^2} \beta^2 + \mathcal{O}(\beta^4), \tag{5.5}$$

where a and b are fixed by the least squares. For the values explored in the analysis $\beta \ll 1$, hence the behaviour of α is dominated by the constant term, as confirmed also by the analysis. In fact, the decrease in α is substantially less than 1% for the explored values $0 \leq \beta \leq 10^{-1}$. However, the derivation is no longer valid for models using mini-batch gradient descent, notably NNS, since, in these cases, only a subset of samples is considered at each iteration of the gradient descent. Therefore, the contribution of the β parameter is different and directly impacts the predictions.

5.1.2 Multitask Learning Without Synthetic Data Augmentation

As a separate baseline, we also trained the MT model on experimental data. The columns **Exp** in Table C.3 reports the results for all samples considered in the analysis. For the alloy matrices, the MT model is not able to provide accurate predictions, as its parameters do not adapt correctly to the data. The synthesis of data is thus fundamental to increase the generalisation ability of the model, and to provide accurate predictions. Differently from alloys, in the case of the cement samples, the MT model is actually able to provide an acceptable performance even with experimental data. Results are, however, not at the same level as using synthetic data, especially at higher concentration of the analyte. As shown in the next section, in the case of cement matrices, the best performance is actually reached with just a few synthetic samples.

5.2 Performance Review of the Multitask Approach

We focus on various aspects such as the dependency on the size of the synthetic training set, the level of the random noise β in (3.3), and the validation of the predictions. We compare the results of the baseline techniques using the best result of the ensemble model and PLS1.

5.2.1 Training Set Size

We first consider the dependence on the size of the synthetic training set: we train different models generating 100, 1000, 5000 and 10000 synthetic spectra for each sample. For these considerations, we fix the noise parameter β to the best fitting choices for the different samples. We choose $\beta = 0.10$ for the alloy matrices, and $\beta = 0.03$ for the cement samples, in order to avoid introducing an additional dependency (see Figures 3.3 and D.1 to D.4 in Appendix D, and their relative details in Section 3.1). For brevity, in Table C.3 in Appendix C, we report the full

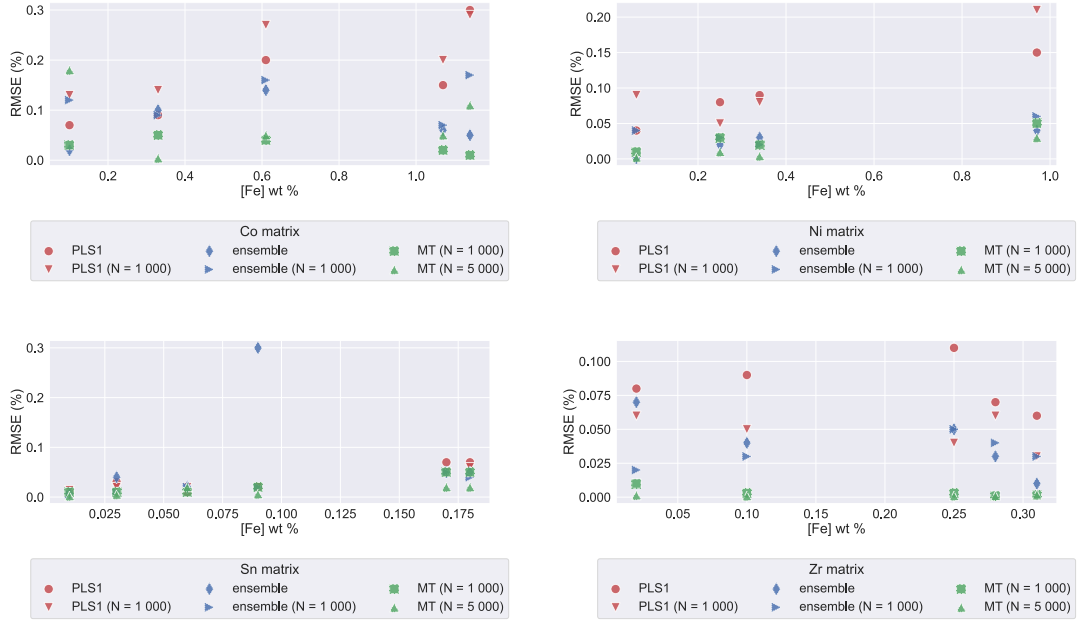


Figure 5.2. Prediction uncertainties of the MT model on alloy matrices as a function of training set size. *Uncertainties are expressed as RMSE on the concentration of the analyte. For brevity, results of the MT architecture are reported for 1000 and 5000 synthetic spectra per sample, as they represent the best terms of comparison in the dataset.*

inference results, which we graphically summarise in Figure 5.2 for the alloy matrices, and in Figure 5.3 for the cement samples.

The possibility to increase arbitrarily the size of the training set is key to increase the overall performance of the model. We see, for instance, that, in terms of robustness, the MT architecture is capable of delivering a homoscedastic performance for all concentrations of the analyte (apart from anomalies, which are discussed in the following). Moreover, the prediction uncertainties are usually comparable with or better than the ensemble model, which already presents good results. The MT architecture is thus capable of selecting the information contained in the data to base its own predictions. The use of synthetic samples enables to capture the fluctuations at low concentrations, where the PLS1 model struggles to give accurate results. In this case, the analysis usually benefits from a manual simplification of the data by an expert in the field, as shown by the meta-model. However, the MT model seems to provide at least comparable performance, by selecting automatically spectral ranges of relevance for the predictions. As a general remark, the optimal number of synthetic spectra varies for each matrix, depending on the degree of spectral interference, noise, and sparsity (e.g. 5000 spectra per sample in the case of the Zr matrix, or 1000 spectra per sample for the Cu matrix). The ideal size of the synthetic training set is, however, quite challenging to know *a priori*. Rules of thumb in known DL competitions, such as *ImageNet* [67], seem to suggest a number $\mathcal{O}(10^3)$ of samples per class, in order to reach good classification or regression results. Data augmentation is usually the solution to the lack of training data, provided some conditions on the augmentation procedure are respected [68]. Research on the topic shows different functional dependencies of standard classification and regression metrics, which usually grow as a function of the size of the training

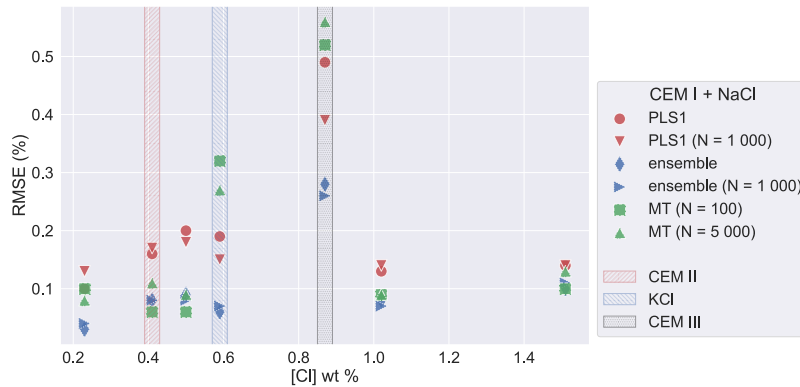


Figure 5.3. Prediction uncertainties of the MT model on cement samples as a function of training set size. *Uncertainties are expressed as RMSE on the concentration of the analyte. For brevity, results of the MT architecture are reported for 100 and 5000 synthetic spectra per sample, as they represent the best terms of comparison in the dataset. Anomalous samples are highlighted in the plot, with the description of the different elements in their fabrication.*

set [69]–[72]. Imbalanced datasets [73] may, however, spoil such behaviour. Heuristically, we noticed that the creation of a large number of synthetic spectra impacts on training time for less than 1% of the total training time, while the latter grows linearly (see Figure 4.5). Such behaviour makes it usually possible to experiment with a few options, in order to determine, using the validation set or the experimental training samples, the best trade-off between the performance of the model and the computational power available.

Finally, notice that, depending on the matrix of the samples and the size of the MT model (number of hidden layers, size of the kernels, etc.), there may be regimes in which the addition of too many synthetic samples may hurt the performance. Recent studies on the double descent phenomenon show an additional trade-off between the size of the model and the amount of data used for training. Nevertheless, the mechanism behind this behaviour remains an open research question [74]–[77]. In the “classical” DL regime, consisting in the optimisation of the bias-variance trade-off, we look for one model, which fits the training set and generalises well to other samples. Larger DL architectures enable more models to fit the same training set, and use the additional parameters to improve the generalisation. This appears as a second descent in the test loss, as a function of the number of free parameters in the model. However, in the phase transition between the two regimes, more synthetic samples may not necessarily lead to better results, since the architectures may not have enough parameters to model correctly the variance of the training set. A simple solution is experimenting with the number of synthetic samples, for instance, looking at the inference results on the experimental training set, or on a synthetic validation set. A second solution, depending on the computational power available, is to study the performance as a function of the size of the DL models (e.g. the number of free parameters). This should allow targeting explicitly the double descent of the loss function, rather than the optimisation of bias and variance.

5.2.2 Random Noise

We then focus on the dependence of the random noise level on the correct representation of the experimental data using synthetic samples. As previously shown, the noise parameter β

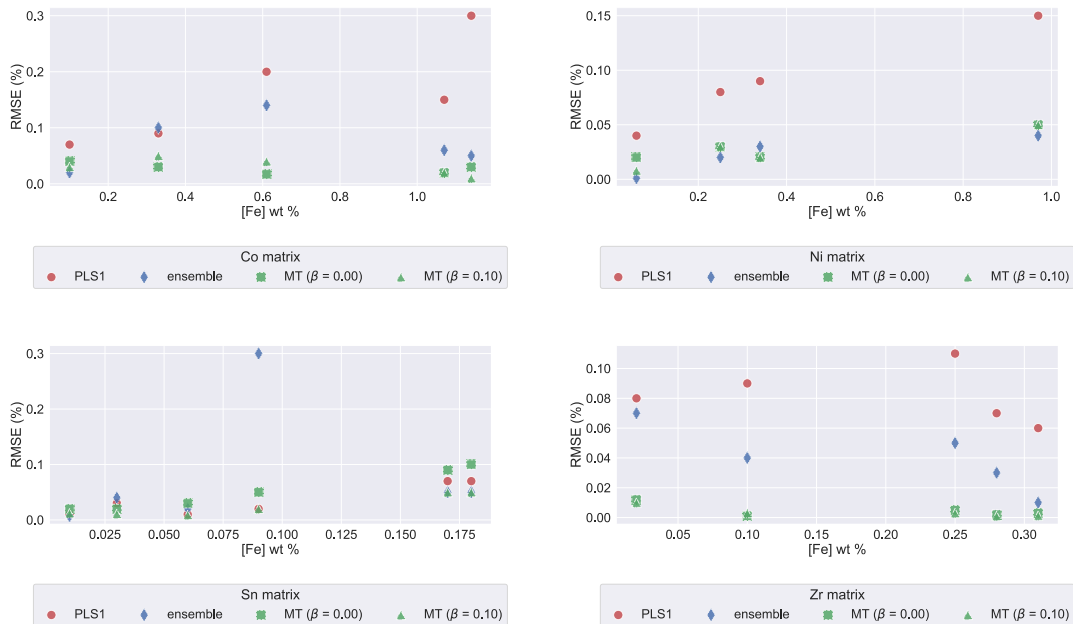


Figure 5.4. Prediction uncertainties of the MT model on alloy matrices as a function of the noise parameter. *Uncertainties are expressed as RMSE on the concentration of the analyte. Results of the MT architecture are reported for $\beta = 0.00$ and $\beta = 0.10$, for illustration purposes.*

influences the distribution of the intensities of the emission lines or molecular bands. Thus, the parameter can be chosen deterministically to suit different needs, for instance by optimising the R^2 score of the coverage diagrams, as shown in Section 3.1, either globally, or on a sample basis. In this section, we do not specifically look for an optimum of the confounder parameter, since we explicitly report results for different values of the noise β . However, we highlight the best choice of such parameter in the range of its explored values. In order to avoid introducing additional variability, we fix the number of synthetic spectra to 1000 per sample, which seems to be a sensible choice in terms of size of the training set, memory requirements, and training time. The detailed results of the analysis are shown in Table C.4 in Appendix C. We present a graphical summary of the salient results in Figure 5.4, for the alloy matrices, and Figure 5.5, for the cement samples. The results suggest that the addition of random noise influences the performance and the robustness of the model.

In particular for the cement samples, the optimal results are achieved using $\beta = 0.03$, which also represents the best fitting choice of the coverage diagrams. As a consequence, the correct modelling of the spectra reduces the average deviations of the samples, even for the out-of-distribution cases. It also improves the robustness of the model at different scales, seen as an overall decrease in the error metrics and a homoscedastic behaviour of the model (with respect, for instance, to the simple LR).

In the case of the alloy matrices, the MT model presents a similar behaviour. The addition of noise to create realistic synthetic samples improves, in general, the performance and the robustness, even though the effect is less intense than previously observed for the cement samples. One of the reasons is experimentally observable in the coverage plots (see Figures D.1 to D.4 in Appendix D for a reference). Spectral interference, more pronounced in these samples, strongly

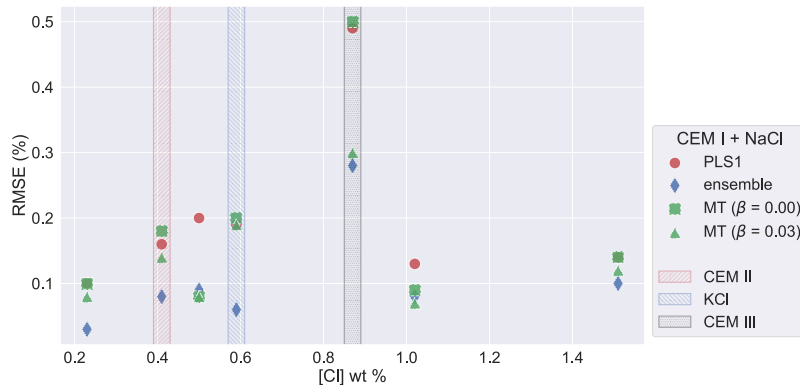


Figure 5.5. Prediction uncertainties of the MT model on cement samples as a function of the noise parameter. *Uncertainties are expressed as RMSE on the concentration of the analyte. Results of the MT architecture are reported for $\beta = 0.00$ and $\beta = 0.03$, for illustration purposes.*

affects different kinds of matrices, and introduces variability at different values of the analyte concentration. Larger, though acceptable, deviations are displayed by difficult cases, such as the Sn matrices, for which the choice $\beta = 0.10$ is not optimal for all samples. On the other hand, matrices, whose samples are well modelled by such a value of the noise parameter (such as Ni and Zr), present both a good and robust out-of-the-box performance. In some alloy matrices, we also notice a negligible impact of differences in the choice of β . This is, in general, due to the DL architecture which is able to leverage the presence of a strong signal, with the help of a large number of heads in the architecture. As previously shown, the MT architecture outputs the intensity of several Fe lines, each competing to improve the main prediction and the other secondary outputs (see Section 3.2). This behaviour enables to mitigate the effects of a sub-optimal modelling of the spectra, as well as providing good generalisation capabilities.

5.2.3 Validation of the Results

For the analysis of the trustworthiness of the model, we use the predictions of the MT model on the independent test set of the alloy matrices and the cement samples. In this analysis, ground truth values of the concentration of the analyte are available for a direct comparison with the predictions of the model. However, in a field application reference values are not available. The analysis of the secondary outputs of the MT architecture is a tool to assess the confidence of the predictions and detection of the anomalous samples or modifications in the experimental conditions. In this case, for the comparison, we fix the number of synthetic spectra per sample to 5000 for both cement and alloy matrices, and we use the β parameter best fitting the local coverage plots.

We first focus on the cement matrices ($\beta = 0.03$). We choose two CaCl molecular bands, used also in MLR and FCNN to predict the concentration of Cl in the samples, for the analysis of the trustworthiness of the predictions. This represents an easy choice, as the two bands are the two most intense in the spectral range considered. Following Section 3.3, we compute the confidence intervals on the experimental training data (unseen by the model, which is trained on synthetic spectra) as in (3.6). For the analysis, we consider $\nu = 25$ degrees of freedom at a confidence level of $1 - \alpha = 0.975$, in order to take well into account possible outliers or defects on the surface of the matrices. Nonetheless, the predictions of the MT model can be studied as a function of α , at

[Cl] wt %	C.I. MAPE (%)	
	593.46 nm	617.74 nm
0.06	3 ± 2	0.9 ± 0.4
0.19	2.1 ± 0.9	0.7 ± 0.3
0.32	1.8 ± 0.6	0.6 ± 0.3
0.46	1.3 ± 0.5	1.0 ± 0.6
0.59	1.3 ± 0.4	1.0 ± 0.4
0.72	1.1 ± 0.5	0.7 ± 0.3
0.85	0.7 ± 0.3	0.4 ± 0.1
0.98	0.9 ± 0.3	0.6 ± 0.4
1.15	1.0 ± 0.3	1.0 ± 0.5
1.43	1.9 ± 1.0	0.9 ± 0.3
1.71	1.3 ± 0.6	1.4 ± 0.8
1.95	1.6 ± 0.4	1.2 ± 0.3

Table 5.1. Confidence intervals of the cement samples. *Confidence intervals (C.I.) measured as in (3.6) on the experimental set using $\nu = 25$ degrees of freedom and a confidence level $1 - \alpha = 0.975$ ($\hat{t}_{1-\alpha}^\nu = 2.06$).*

different levels of confidence. We show the corresponding values in Table 5.1. We consider these values as reference in the analysis of the trustworthiness of the model, since they represent known standards, whose labels are available. In Table 5.2, we present the analysis of the inference on the test cement samples. *A posteriori*, we notice that the predictions of the MT architecture are all compatible with the respective ground truths, even though some samples present larger uncertainties, which may indicate faulty values. However, in the absence of reference values, predictions alone are not sufficient to measure the trustworthiness of the model.

The predictions of the secondary values show that the band at 593.46 nm is able to display a pattern which identifies some anomalies in the prediction of the integral intensities. As previously shown (see Figure 3.6 for a reference), this pattern of MAPE and t -value is typical of anomalous samples, for which the model does not provide precise predictions. In hindsight, the analysis of the secondary outputs identifies the three out-of-distribution samples present in the dataset (different matrix and salt). To measure the trustworthiness of the predictions, we then use a standard *Student's t* two-tailed test (confidence $1 - \alpha = 0.95$ and 25 degrees of freedom) to assess the predictions of the molecular emission bands. We notice that, although the samples register as anomalies, the variance of the predictions is such to include the true values of the secondary outputs in the error intervals with good confidence (case 4 in Figure 3.6). Given the inter-dependencies of the MT model previously discussed, the confidence on the predictions of the secondary output influences directly the confidence on the main prediction, the concentration of the analyte. The precise quantification of the confidence level is, nonetheless, not trivial because of the large number of parameters involved in the computation. In the case at hand, we can interpret the result by noting that the MT model is still capable of providing trustworthy predictions on the concentration of the analyte. However, its precision is highly affected in the presence of anomalous samples: the predictions of the main output contain the true value, within the uncertainty, with high probability. In other words, in this scenario, the predicted values of the concentration of the analyte can be considered compatible with the reference values, provided by the supplier. Further investigation on three anomalous samples remains necessary.

In Figure 5.6, we graphically summarise the same analysis for the alloy matrices (see Ta-

Ground truth [Cl] wt %	Prediction [Cl] wt %	MAPE (%)		t-value	
		593.46 nm	617.74 nm	593.46 nm	617.74 nm
0.23	0.25 ± 0.08	1.4	0.7	0.69	0.34
0.41 (CEM II)	0.41 ± 0.11	4.1	0.8	0.98	0.32
0.50	0.54 ± 0.09	1.7	0.7	0.48	0.26
0.59 (KCl)	0.33 ± 0.27	4.2	0.8	1.29	0.31
0.87 (CEM III)	1.40 ± 0.56	4.7	1.4	0.77	0.41
1.02	0.97 ± 0.09	1.3	0.4	0.38	0.16
1.51	1.54 ± 0.13	1.5	0.8	0.43	0.30

Table 5.2. Trustworthiness of the predictions on cement samples. *Analysis of the predictions and the secondary outputs of the MT model for the cement samples (uncertainties reported represent the RMSE). Possible anomalies are highlighted in bold characters.*

ble C.5 in Appendix C for the full results). They reasonably present quite different behaviours with respect to the cement samples. We notice that the Sn matrix displays very high values of the MAPE in correspondence of lower Fe concentrations, even though the variance of the predictions is such to ensure the compatibility of the predictions. This indicates, again, a MT model whose interpolation is possible even at small concentration of the analyte, even though precision may strongly be impacted. As previously observed, iron lines are strongly affected by spectral interference, and represents a difficult case for the architecture. As in the Zn matrix, the interference with Cu and Ni on the entire spectral range leads to a complex computation for the model. The first element, specifically, is present in the matrix in strongly greater concentrations with respect to the analyte (18 to 160 times the concentration of Fe in the Sn matrix, 60 to 170 in the Zn matrix). Since both Sn and Zn matrices were not normalised on the contributions of Cu (contrary, for instance, to the Cu matrix itself), the presence of the element restricts the generalisation ability of the model. We also notice that, for the Sn matrix, the uncertainties of the MT architecture do not differ from the performance of the ensemble model. A similar discussion holds also for the Zn matrix (see Table C.5 in Appendix C), for which the spectral interference produces large uncertainties in the prediction of the secondary outputs. However, the large variance of the predictions of the secondary outputs ensures compatibility with the true values: the model is still able to extrapolate the predictions, even in the presence of a large number of outliers. In turn, the predictions of the concentration of the analyte can be considered trustworthy (*a posteriori*, they are indeed compatible with the respective ground truths, and present quite small uncertainties, too). For instance, to improve the performance on these matrices, it would be interesting to increase the training time of the AI architecture, or fine-tune the models using a the experimental spectra. As an alternative, more experimental spectra may provide additional elements to model the synthetic data. Other matrices present only local spikes in the MAPE metric, in correspondence of a few Fe emission lines, and mostly for low concentrations of the analyte. The corresponding *t*-values are well within the limits of standard statistical tests, as shown in Figure 5.6. In general, the MT models, trained on the different matrices, can be deemed trustworthy with high probability. Moreover, no specific samples stand out as anomalies. No sample presents incompatible *t*-values or frequent (e.g. on all secondary outputs) and large MAPE (values are at most at the limit of the confidence intervals computed on the experimental data). This provides a way to assess the robustness of the MT architecture on the entire range of variability of the Fe concentration. Notice that the analysis of the secondary outputs is quantitative: for instance, a *p*-value of the prediction is computable (though, generally, not necessary). This enables to assess the performance of the model at different concentration levels. Moreover,

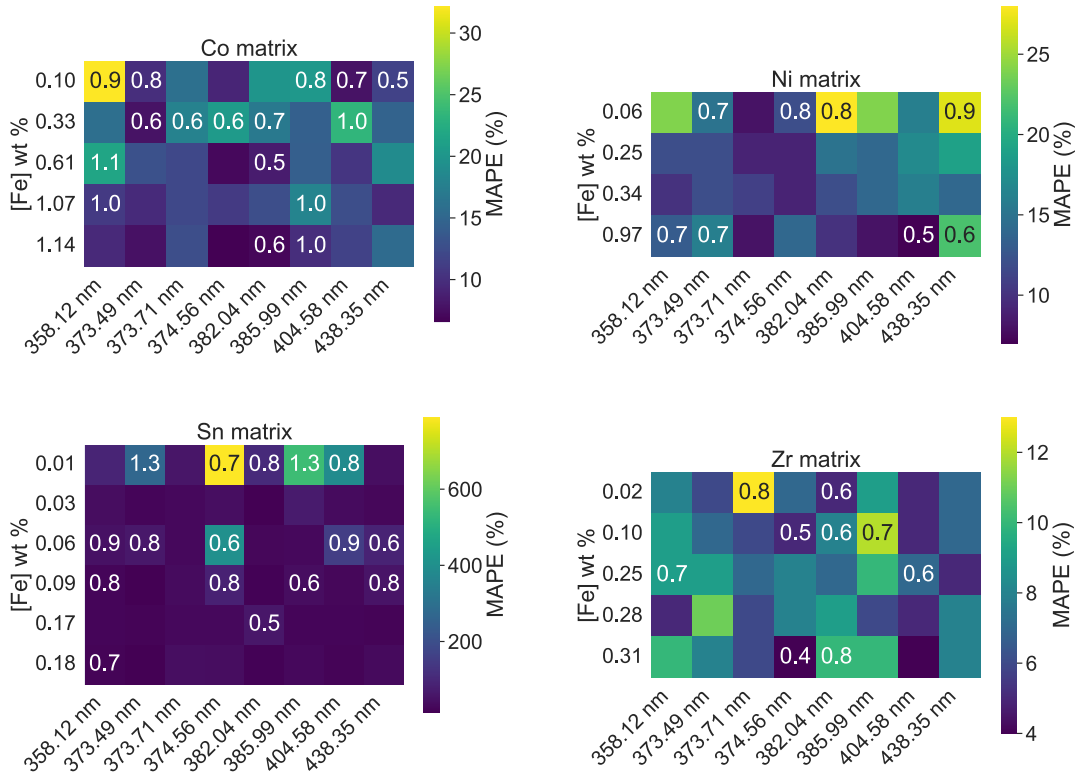


Figure 5.6. Summary of the confidence analysis on the alloy matrices. The colour map represents the MAPE. The t variable is indicated for values outside the confidence intervals measured in the experimental set, for the corresponding concentrations of the analyte, using $\nu = 25$ degrees of freedom and confidence $1 - \alpha = 0.95$ ($\hat{t}_{1-\frac{\alpha}{2}}^{\nu} = 2.06$).

different choices of the confidence $1 - \alpha$ allow comparing the model as functions of the confidence level. Finally, this analysis is always possible, with any sample, since the information contained in the secondary outputs of the model is directly comparable with the experimental data. This is different from the concentration of the analyte itself, which is known only for standard samples. This is achievable, in general, with a multi-output model, capable of providing different related quantities as predictions. A MT architecture is particularly suited, though more complex, since it first processes the input spectra into a common latent representation (in the hard parameter sharing implementation). It then proceeds to achieve the best possible performance on each task separately, in turn improving the overall performance and reducing the risk of overfit of the training data (better generalisation).

5.2.4 Anomaly Detection Mechanism: Calibration Transfer

In order to test the whole procedure, we consider the MT model trained on a matrix, and compute the predictions on different matrices, to illustrate the anomaly detection mechanism. We test the trustworthiness of the predictions in the presence of a change in the distribution of the samples. Specifically, we consider the MT model trained on the Co matrix, and we perform the inference

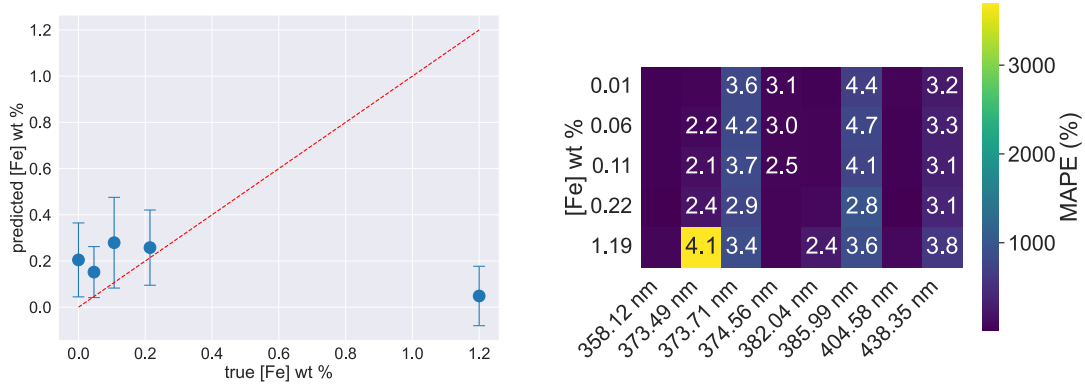


Figure 5.7. Calibration transfer of the MT model. The plot on the left compares the ground truth values of the concentration of the analyte in the Ti matrix with the predictions of the MT model trained on the Co matrix. The summary on the right displays both the values of the error fraction (MAPE) of the secondary outputs and the incompatible values of the t variable.

on the Ti and Zn matrices. In Figure 5.7, we show the true and predicted concentrations of the analyte, generally known only *a posteriori*. The model does not generalise among different matrices, hence it is not usable for calibration transfer. In the same image, we also show the statistical analysis on the secondary outputs. The Ti matrix presents predictions characterised by large values of the error fractions and by incompatible values of the t variable, whose threshold is $\hat{t}_{1-\frac{\alpha}{2}}^{\nu} = 2.06$ for $\nu = 25$ degrees of freedom and a confidence $1 - \alpha = 0.95$. For instance, this shows that the predictions of the concentration levels 0.11 wt% and 0.22 wt%, though compatible with their respective ground truths, should not be considered trustworthy. The same analysis on the Zn matrix shows MAPE larger than 10^4 on the predictions of the emission lines (see Figure D.6 in Appendix D). According to Figure 3.6, any value of the t variable would then be considered anomalous. The MT model is thus capable of detecting anomalies or modifications in the experimental conditions, which is key to assessing correctly the ability of the model to provide trustworthy predictions. Especially when a *posteriori* analyses are not feasible.

5.2.5 Towards the Resolution of Spectral Interference

Finally, we quickly consider the case of matrices, such as Sn and Ti, in the presence of spectral interference of Fe with elements such as Cu (see Section 5.2.3) for the Sn matrix or the matrix itself in the case of Ti. Despite the sparser spectra (see Figure 4.1), due to these phenomena, the MT models show higher uncertainty in the prediction of the line intensities, even though the variance of the predictions ensures compatible results. Given the training technique adopted in the analysis, the fine-tuning of the model to the intensity of the emission lines happens later in training, due to the growth of the associated parameter in the loss (see Section 4.6). We consider the Sn and Ti matrix with 1000 synthetic spectra per sample, as it represents a good trade-off between performance and wall time needed to train the MT model. We perform a longer 2000 epochs training. We also introduce a 10^{-3} ℓ_1 regularisation factor to enforce sparsity in the model, to focus training only on necessary parameters. In Figure 5.8, we show the analysis of the main output of the MT model. As far as the prediction of the concentration of the analyte is concerned, longer training and sparsity seem to be only slightly beneficial to the trueness of the model. This is the expected behaviour, since the learning of the main output happens

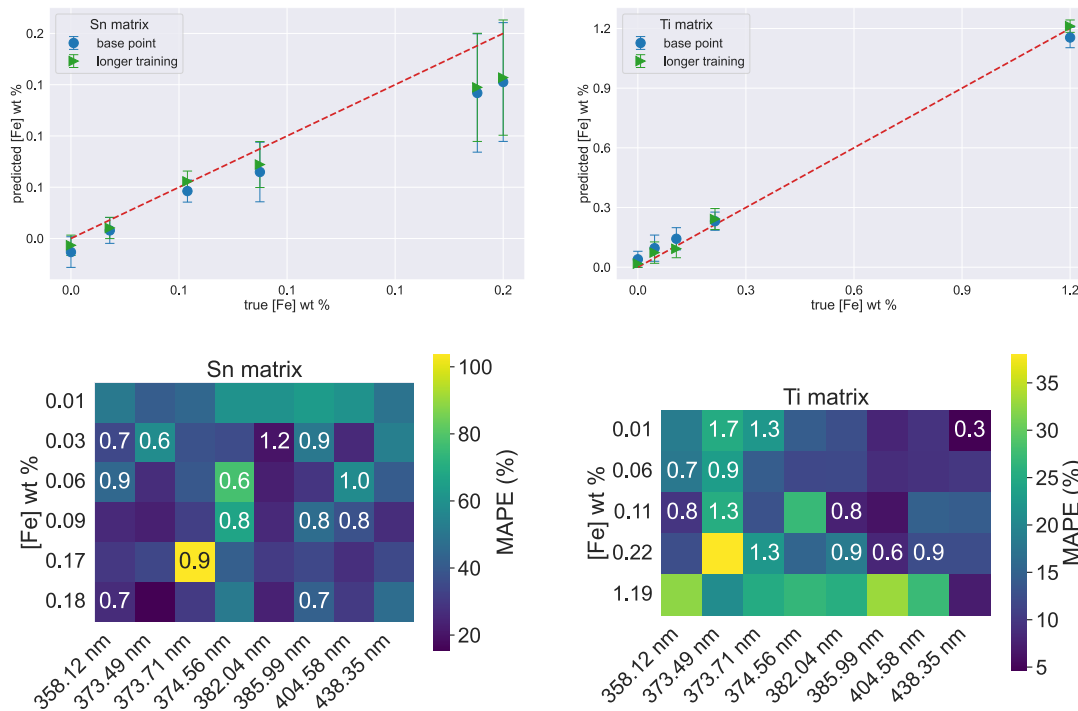


Figure 5.8. Impact of longer training on matrices with sparser spectra. *The top portion of the figure represents the comparison of the predicted values of the concentration of Fe in the matrices with the corresponding ground truths. At the bottom, we show the results of the confidence analysis of the secondary outputs: t values are annotated for values of MAPE outside the confidence intervals computed as in (3.6).*

sooner in training. The major improvement is rather on the reduction of the error fraction of the secondary outputs, which contain more precise predictions. The AI model has improved its understanding of the dependencies between the variables (the wavelength channels) contained in the data (spectra). This has a two-fold effect on the overall performance of the model. On the one hand, it contributes to slightly improve the predictions of the principal output. On the other, it grants better generalisation, by improving the adaptation of all outputs to the specific type of data. In turn, the trustworthiness and confidence of the model improves. With respect to Figure 5.6, the Sn matrix in Figure 5.8 displays lower MAPE for all secondary outputs, and for all concentrations of Fe. It also displays lower values of the t -variable, in correspondence of MAPE near the limits of the confidence intervals. Though not shown previously as an image (results are available in Table C.5 in Appendix C), the Ti matrix displays the same behaviour. We thus notice that the validation technique needs a good balance in learning of all tasks, in order to provide trustworthy predictions and the corresponding means to check their predictions.

6 Conclusions

In this work, we use DL techniques to address the quantitative analysis of LIBS data, the prediction of the concentration of an analyte, using a multivariate calibration procedure. We focus

on complementary aspects: the creation of a synthetic set of spectra as a data augmentation technique to increase the number of samples available for training, the construction of a robust MT learning model based on deep CNNs, and the analysis of the confidence of the predictions. We use the entire experimental emission spectra as inputs, without the need for a preselection of variables or dimensionality reduction. These DL architectures are, however, more complicated and longer to train than usual univariate or multivariate analysis. In some cases, they may require large computational power, though we quickly show that specific applications may be satisfied by simpler setups. Nevertheless, we leverage the robustness and performance of CNNs with the possibility to provide a tool to assess the trustworthiness of the predictions of the model, even for unknown data. Moreover, once the models are trained, the MT architecture represents a fast way to perform inference.

To this end, we introduce a MT learning architecture, based on hard parameter sharing. The model is capable of predicting the concentration of the analyte and the integral intensities of relevant emission lines (or molecular bands), at the same time. Given the size and complexity of the DL model, we introduce a data augmentation technique, based on the simulation of LIBS spectra, to create an arbitrary number of input spectra, statistically representative of the experimental data. In the analysis, we study the role of different elements entering both the theoretical modelling of the spectra and the training of the NNS. We show that synthetic spectra can indeed be used to train DL models with good generalisation ability. The MT architectures display robustness (homoscedastic behaviour) across the range of variation of the analytes. It also presents an overall good performance, usually better or, at least, comparable to the SOTA, though without the need for any preselection or reduction of the input data. Finally, the presence of the secondary outputs, allows us to introduce a statistical analysis, based on the mutual dependencies of the parameters of the AI architecture, which enables the assessment of the trustworthiness of the model. Comparisons of the predicted values with the intensities found in the experimental spectra, always available, can be used to study the predictions of the concentration of the analyte, at a given level of confidence of the model. In turn, this grants the ability to assess the extrapolation abilities of the DL model. The technique can then be used to identify anomalous samples, or to detect a change in the experimental conditions, with respect to the training samples.

Given the versatility of MT learning and its complementarity to other techniques already explored in the literature, new investigations may be possible in the future. In particular, the model used to generate synthetic spectra may be further developed to account for different experimental aspects. For instance, it could be used to model different noise sources as different confounder parameters in the likelihood function in (3.4). Moreover, advanced generative models, such as adversarial networks [78] or the more recently successful diffusion models [79]–[81], may be employed to model the distribution of the LIBS spectra and generate realistic synthetic datasets [82], with the possibility to control several experimental and physical parameters. MT also offers the possibility to provide multiple predictions of concentrations at once. In principle, different analytes could be studied together (as already explored in the literature) and a measure of global confidence could be attached to the model, using the secondary outputs as a basis for the statistical analysis. Moreover, interpretable-AI methods, either based on the study of the hidden structures in NNS [49], [50] or quantitative statistical tools [83]–[85], could be coupled to our technique to provide a more complete analysis. Finally, as training sets of arbitrary size can be synthesised, the impact of larger architectures could be explored at length. This could provide the possibility to use more complex and larger models, based on transformers or attention mechanisms [86], which may also give some insights on interpretability of the decision mechanisms.

Author Contributions

Riccardo Finotello: conceptualization, data curation, formal analysis, investigation, methodology, software, validation, visualization, writing – original draft, writing – review & editing; **Daniel L’Hermite:** investigation, methodology, resources, validation, writing – review & editing; **Celine Quéré:** investigation, methodology, validation, writing – review & editing; **Benjamin Rouge:** investigation, methodology, validation; **Mohamed Tamaazousti:** funding acquisition, project administration, resources, supervision, writing – review & editing; **Jean-Baptiste Sirven:** data curation, funding acquisition, project administration, resources, supervision, writing – review & editing.

Conflicts of Interests

There are no conflicts to declare.

Acknowledgements

We acknowledge the financial support of the *Cross-Disciplinary Programme on Instrumentation and Detection* of CEA, the French *Alternative Energies and Atomic Energy Commission*. We thank G. Gallou for proposing this collaboration. This publication was made possible by the use of the *FactoryIA* supercomputer, financially supported by the *Ile-De-France Regional Council*.

References

- [1] B. Debus, H. Parastar, P. Harrington, *et al.*, “Deep learning in analytical chemistry,” *Trends Anal. Chem.*, vol. 145, 116459, 2021. DOI: [10.1016/j.trac.2021.116459](https://doi.org/10.1016/j.trac.2021.116459).
- [2] H. Martens and S. Foulk, “NIR instruments and multivariate change thinking in process analysis,” *Adv. Instrum. Control*, vol. 45, no. 3, 1517–1528, 1990.
- [3] S. Moncayo, L. Duponchel, N. Mousavipak, *et al.*, “Exploration of megapixel hyperspectral LIBS images using principal component analysis,” *J. Anal. At. Spectrom.*, vol. 33, 210–220, 2 2018. DOI: [10.1039/c7ja00398f](https://doi.org/10.1039/c7ja00398f).
- [4] R. Finotello, M. Tamaazousti, and J.-B. Sirven, “HyperPCA: A powerful tool to extract elemental maps from noisy data obtained in LIBS mapping of materials,” *Spectrochim. Acta Part B*, vol. 192, 106418, 2022. DOI: [10.1016/j.sab.2022.106418](https://doi.org/10.1016/j.sab.2022.106418).
- [5] R. Sattmann, I. Monch, H. Krause, *et al.*, “Laser-induced breakdown spectroscopy for polymer identification,” *Appl. Spectrosc.*, no. 3, 456–461, 1998. DOI: [10.1366/0003702981943680](https://doi.org/10.1366/0003702981943680).
- [6] L.-N. Li, X.-F. Liu, F. Yang, *et al.*, “A review of artificial neural network based chemometrics applied in laser-induced breakdown spectroscopy analysis,” *Spectrochim. Acta Part B*, vol. 180, 106183, 2021. DOI: <https://doi.org/10.1016/j.sab.2021.106183>.
- [7] V. C. Costa, D. V. Babos, J. P. Castro, *et al.*, “Calibration strategies applied to laser-induced breakdown spectroscopy: A critical review of advances and challenges,” *J. Braz. Chem. Soc.*, vol. 31, no. 12, 2439–2451, 2020. DOI: [10.21577/0103-5053.20200175](https://doi.org/10.21577/0103-5053.20200175).
- [8] V. Motto-Ros, S. Moncayo, F. Trichard, *et al.*, “Investigation of signal extraction in the frame of laser induced breakdown spectroscopy imaging,” *Spectrochim. Acta Part B*, vol. 155, 127–133, 2019. DOI: [10.1016/j.sab.2019.04.004](https://doi.org/10.1016/j.sab.2019.04.004).
- [9] M. Hoehse, A. Paul, I. Gornushkin, *et al.*, “Multivariate classification of pigments and inks using combined Raman spectroscopy and LIBS,” *Anal. Bioanal. Chem.*, vol. 402, no. 4, 1443–1450, 2012. DOI: [10.1007/s00216-011-5287-6](https://doi.org/10.1007/s00216-011-5287-6).

- [10] N. C. Dingari, I. Barman, A. K. Myakalwar, *et al.*, "Incorporation of support vector machines in the LIBS toolbox for sensitive and robust classification amidst unexpected sample and system variability," *Anal. Chem.*, vol. 84, no. 6, 2686–2694, 2012. DOI: [10.1021/ac202755e](https://doi.org/10.1021/ac202755e).
- [11] J. Cisewski, E. Snyder, J. Hannig, *et al.*, "Support vector machine classification of suspect powders using laser-induced breakdown spectroscopy (LIBS) spectral data," *J. Chemom.*, vol. 26, no. 5, 143–149, 2012. DOI: [10.1002/cem.2422](https://doi.org/10.1002/cem.2422).
- [12] P. Yaroshchuk, D. L. Death, and S. J. Spencer, "Comparison of principal components regression, partial least squares regression, multi-block partial least squares regression, and serial partial least squares regression algorithms for the analysis of Fe in iron ore using LIBS," *J. Anal. At. Spectrom.*, vol. 27, no. 1, 92–98, 2012. DOI: [10.1039/c1ja10164a](https://doi.org/10.1039/c1ja10164a).
- [13] I. Monch, R. Sattmann, and R. Noll, "High speed identification of polymers by laser-induced breakdown spectroscopy," in *Sensors, Sensor Systems, and Sensor Data Processing*, O. Loffeld, Ed., ser. Proceedings of the Society of Photo-optical Instrumentation Engineers (SPIE), vol. 3100, 1997, 64–74, ISBN: 0-8194-2520-6. DOI: [10.1117/12.281265](https://doi.org/10.1117/12.281265).
- [14] V. Motto-Ros, A. S. Koujelev, G. R. Osinski, *et al.*, "Quantitative multi-elemental laser-induced breakdown spectroscopy using artificial neural networks," *J. Eur. Opt. Soc.-Rapid Publ.*, vol. 3, 08011, 2008. DOI: [10.2971/jeos.2008.08011](https://doi.org/10.2971/jeos.2008.08011).
- [15] X. Zhang, T. Lin, J. Xu, *et al.*, "DeepSpectra: An end-to-end deep learning approach for quantitative spectral analysis," *Analytica Chimica Acta*, vol. 1058, 48–57, 2019. DOI: [10.1016/j.aca.2019.01.002](https://doi.org/10.1016/j.aca.2019.01.002).
- [16] D. W. Hahn and N. Omenetto, "Laser-induced breakdown spectroscopy (LIBS), part II: Review of instrumental and methodological approaches to material analysis and applications to different fields," *Appl. Spectrosc.*, vol. 66, no. 4, 347–419, 2012. DOI: [10.1366/11-06574](https://doi.org/10.1366/11-06574).
- [17] J.-B. Sirven, B. Bousquet, L. Canioni, *et al.*, "Qualitative and quantitative investigation of chromium-polluted soils by laser-induced breakdown spectroscopy combined with neural networks analysis," *Anal. Bioanal. Chem.*, vol. 385, no. 2, 256–262, 2006. DOI: [10.1007/s00216-006-0322-8](https://doi.org/10.1007/s00216-006-0322-8).
- [18] T. Takahashi and B. Thornton, "Quantitative methods for compensation of matrix effects and self-absorption in laser induced breakdown spectroscopy signals of solids," *Spectrochim. Acta Part B*, vol. 138, 31–42, 2017. DOI: [10.1016/j.sab.2017.09.010](https://doi.org/10.1016/j.sab.2017.09.010).
- [19] D. Luarte, A. K. Myakalwar, M. Velasquez, *et al.*, "Combining prior knowledge with input selection algorithms for quantitative analysis using neural networks in laser induced breakdown spectroscopy," *Anal. Meth.*, vol. 13, no. 9, 1181–1190, 2021. DOI: [10.1039/d0ay02300k](https://doi.org/10.1039/d0ay02300k).
- [20] J. Chen, J. Pisonero, S. Chen, *et al.*, "Convolutional neural network as a novel classification approach for laser-induced breakdown spectroscopy applications in lithological recognition," *Spectrochim. Acta Part B*, vol. 166, 105801, 2020. DOI: [10.1016/j.sab.2020.105801](https://doi.org/10.1016/j.sab.2020.105801).
- [21] L. Zou, C. Sun, M. Wu, *et al.*, "Online simultaneous determination of H₂O and KCl in potash with LIBS coupled to convolutional and back-propagation neural networks," *J. Anal. At. Spectrom.*, vol. 36, no. 2, 303–313, 2021. DOI: [10.1039/d0ja00431f](https://doi.org/10.1039/d0ja00431f).
- [22] C. Lu, B. Wang, X. Jiang, *et al.*, "Detection of K in soil using time-resolved laser-induced breakdown spectroscopy based on convolutional neural networks," *Plasma Sci. Technol.*, vol. 21, no. 3, 034014, 2019. DOI: [10.1088/2058-6272/aaef6e](https://doi.org/10.1088/2058-6272/aaef6e).
- [23] T. Chen, L. Sun, H. Yu, *et al.*, "Deep learning with laser-induced breakdown spectroscopy (LIBS) for the classification of rocks based on elemental imaging," *Appl. Geochem.*, vol. 136, 105135, 2022. DOI: [10.1016/j.apgeochem.2021.105135](https://doi.org/10.1016/j.apgeochem.2021.105135).
- [24] E. D'Andrea, S. Pagnotta, E. Grifoni, *et al.*, "A hybrid calibration-free/artificial neural networks approach to the quantitative analysis of LIBS spectra," *Appl. Phys. B*, vol. 118, no. 3, 353–360, 2015. DOI: [10.1007/s00340-014-5990-z](https://doi.org/10.1007/s00340-014-5990-z).
- [25] L. Narlagiri and V. R. Soma, "Simultaneous quantification of Au and Ag composition from Au-Ag bi-metallic LIBS spectra combined with shallow neural network model for multi-output regression," *Appl. Phys. B: Lasers Opt.*, vol. 127, no. 9, 135, 2021. DOI: [10.1007/s00340-021-07681-y](https://doi.org/10.1007/s00340-021-07681-y).
- [26] R. Caruana, "Multitask learning: A knowledge-based source of inductive bias," in *Proceedings of the Tenth International Conference on International Conference on Machine Learning*, ser. Icml'93, Amherst, MA, USA: Morgan Kaufmann Publishers Inc., 1993, 41–48, ISBN: 1558603077. DOI: [10.1016/b978-1-55860-307-3.50012-5](https://doi.org/10.1016/b978-1-55860-307-3.50012-5).
- [27] R. Caruana, "Multitask learning," *Mach. Learn.*, vol. 28, no. 1, 41–75, 1997. DOI: [10.1023/a:1007379606734](https://doi.org/10.1023/a:1007379606734).

- [28] R. T. Mullapudi, W. R. Mark, N. Shazeer, *et al.*, “Hydranets: Specialized dynamic architectures for efficient inference,” in *Proceedings of the IEEE Conference on Computer Vision and Pattern Recognition*, 2018, 8080–8089. DOI: [10.1109/cvpr.2018.00843](https://doi.org/10.1109/cvpr.2018.00843).
- [29] H. Erbin and R. Finotello, “Machine learning for complete intersection Calabi–Yau manifolds: A methodological study,” *Phys. Rev. D*, vol. 103, 126014, 12 2021. DOI: [10.1103/PhysRevD.103.126014](https://doi.org/10.1103/PhysRevD.103.126014).
- [30] —, “Inception neural network for complete intersection Calabi–Yau 3-folds,” *Mach. Learn. Sci. Tech.*, vol. 2, no. 2, 2021. DOI: [10.1088/2632-2153/abda61](https://doi.org/10.1088/2632-2153/abda61).
- [31] H. Erbin, R. Finotello, R. Schneider, *et al.*, “Deep multi-task mining Calabi–Yau four-folds,” *Mach. Learn. Sci. Tech.*, vol. 3, no. 1, 015006, 2021.
- [32] S. Reed, K. Zolna, E. Parisotto, *et al.*, “A generalist agent,” 2022. arXiv: [2205.06175 \[cs.AI\]](https://arxiv.org/abs/2205.06175).
- [33] H. Shevlin, K. Vold, M. Crosby, *et al.*, “The limits of machine intelligence: Despite progress in machine intelligence, artificial general intelligence is still a major challenge,” *EMBO reports*, vol. 20, no. 10, 2019. DOI: [10.15252/embr.201949177](https://doi.org/10.15252/embr.201949177).
- [34] L.-N. Li, X.-F. Liu, W.-M. Xu, *et al.*, “A laser-induced breakdown spectroscopy multi-component quantitative analytical method based on a deep convolutional neural network,” *Spectrochim. Acta Part B*, vol. 169, 105850, 2020. DOI: [10.1016/j.sab.2020.105850](https://doi.org/10.1016/j.sab.2020.105850).
- [35] R. B. Anderson, J. F. Bell III, R. C. Wiens, *et al.*, “Clustering and training set selection methods for improving the accuracy of quantitative laser induced breakdown spectroscopy,” *Spectrochim. Acta Part B*, vol. 70, 24–32, 2012. DOI: [10.1016/j.sab.2012.04.004](https://doi.org/10.1016/j.sab.2012.04.004).
- [36] F. O. Borges, G. H. Cavalcanti, G. C. Gomes, *et al.*, “A fast method for the calculation of electron number density and temperature in laser-induced breakdown spectroscopy plasmas using artificial neural networks,” *Appl. Phys. B*, vol. 117, no. 1, 437–444, 2014. DOI: [10.1007/s00340-014-5852-8](https://doi.org/10.1007/s00340-014-5852-8).
- [37] H. Saeidfirozeh, A. K. Myakalwar, P. Kubelík, *et al.*, “ANN-LIBS analysis of mixture plasmas: Detection of xenon,” *J. Anal. At. Spectrom.* (*accepted*), 2022. DOI: [10.1039/d2ja00132b](https://doi.org/10.1039/d2ja00132b).
- [38] S. Chen, H. Pei, J. Pisonero, *et al.*, “Simultaneous determination of lithology and major elements in rocks using laser-induced breakdown spectroscopy (LIBS) coupled with a deep convolutional neural network,” *J. Anal. At. Spectrom.*, vol. 37, no. 3, 508–516, 2022. DOI: [10.1039/d1ja00406a](https://doi.org/10.1039/d1ja00406a).
- [39] J.-M. Mermet, “Limit of quantitation in atomic spectrometry: An unambiguous concept?” *Spectrochim. Acta Part B*, vol. 63, no. 2, 166–182, 2008, Honoring Issue A Collection of Papers on Atomic, Molecular and Laser Spectroscopy Dedicated to James D. Winefordner. DOI: [10.1016/j.sab.2007.11.029](https://doi.org/10.1016/j.sab.2007.11.029).
- [40] —, “Calibration in atomic spectrometry: A tutorial review dealing with quality criteria, weighting procedures and possible curvatures,” *Spectrochim. Acta Part B*, vol. 65, no. 7, 509–523, 2010. DOI: [10.1016/j.sab.2010.05.007](https://doi.org/10.1016/j.sab.2010.05.007).
- [41] G. Grimmett and D. Stirzaker, *Probability and random processes*. Oxford university press, 2020, ISBN: 9780198847595. [Online]. Available: <https://global.oup.com/academic/product/probability-and-random-processes-9780198847595>.
- [42] A. Ciucci, M. Corsi, V. Palleschi, *et al.*, “New procedure for quantitative elemental analysis by laser-induced plasma spectroscopy,” *Appl. Spectrosc.*, vol. 53, no. 8, 960–964, 1999. DOI: [10.1366/0003702991947612](https://doi.org/10.1366/0003702991947612).
- [43] D. A. Cremers and L. J. Radziemski, “Selected LIBS applications,” in *Handbook of laser-induced breakdown spectroscopy*. John Wiley & Sons, Ltd, 2013, ch. 9, 289–331, ISBN: 9781118567371. DOI: [10.1002/9781118567371.ch9](https://doi.org/10.1002/9781118567371.ch9).
- [44] E. Tognoni, G. Cristoforetti, S. Legnaioli, *et al.*, “Calibration-free laser-induced breakdown spectroscopy: State of the art,” *Spectrochim. Acta Part B*, vol. 65, no. 1, 1–14, 2010. DOI: [10.1016/j.sab.2009.11.006](https://doi.org/10.1016/j.sab.2009.11.006).
- [45] G. H. Cavalcanti, D. V. Teixeira, S. Legnaioli, *et al.*, “One-point calibration for calibration-free laser-induced breakdown spectroscopy quantitative analysis,” *Spectrochim. Acta Part B*, vol. 87, 51–56, 2013. DOI: [10.1016/j.sab.2013.05.016](https://doi.org/10.1016/j.sab.2013.05.016).
- [46] C.-T. Chen, D. Banaru, T. Sarnet, *et al.*, “Two-step procedure for trace element analysis in food via calibration-free laser-induced breakdown spectroscopy,” *Spectrochim. Acta Part B*, vol. 150, 77–85, 2018. DOI: [10.1016/j.sab.2018.10.011](https://doi.org/10.1016/j.sab.2018.10.011).
- [47] J. El Haddad, L. Canioni, and B. Bousquet, “Good practices in LIBS analysis: Review and advices,” *Spectrochim. Acta Part B*, vol. 101, 171–182, 2014. DOI: [10.1016/j.sab.2014.08.039](https://doi.org/10.1016/j.sab.2014.08.039).
- [48] C. L. Morais, K. M. Lima, and F. L. Martin, “Uncertainty estimation and misclassification probability for classification models based on discriminant analysis and support vector machines,” *Anal. Chim. Acta*, vol. 1063, 40–46, 2019. DOI: [10.1016/j.aca.2018.09.022](https://doi.org/10.1016/j.aca.2018.09.022).

- [49] W. Zhao, C. Li, C. Yan, *et al.*, “Interpretable deep learning-assisted laser-induced breakdown spectroscopy for brand classification of iron ores,” *Anal. Chim. Acta*, vol. 1166, 338574, 2021. DOI: [10.1016/j.aca.2021.338574](https://doi.org/10.1016/j.aca.2021.338574).
- [50] X. Zhang, J. Xu, J. Yang, *et al.*, “Understanding the learning mechanism of convolutional neural networks in spectral analysis,” *Anal. Chim. Acta*, vol. 1119, 41–51, 2020. DOI: [10.1016/j.aca.2020.03.055](https://doi.org/10.1016/j.aca.2020.03.055).
- [51] J. Baxter, “A model of inductive bias learning,” *J. Artif. Intell. Res.*, vol. 12, 149–198, 2000. DOI: [10.1613/jair.731](https://doi.org/10.1613/jair.731).
- [52] M. Crawshaw, “Multi-task learning with deep neural networks: A survey,” 2020. arXiv: [2009.09796](https://arxiv.org/abs/2009.09796) [cs.LG].
- [53] T. Völker, G. Wilsch, I. B. Gornushkin, *et al.*, “Interlaboratory comparison for quantitative chlorine analysis in cement pastes with laser-induced breakdown spectroscopy,” *Spectrochim. Acta Part B (submitted)*, 2022.
- [54] I. Loshchilov and F. Hutter, “Decoupled weight decay regularization,” 2017. arXiv: [1711.05101](https://arxiv.org/abs/1711.05101) [cs.LG].
- [55] D. P. Kingma and J. Ba, “Adam: A method for stochastic optimization,” 2014. arXiv: [1412.6980](https://arxiv.org/abs/1412.6980) [cs.LG].
- [56] P. J. Huber, “Robust estimation of a location parameter,” *The Annals of Mathematical Statistics*, vol. 35, no. 1, 73–101, 1964. DOI: [10.1214/aoms/1177703732](https://doi.org/10.1214/aoms/1177703732).
- [57] J. Bergstra, R. Bardenet, Y. Bengio, *et al.*, “Algorithms for hyper-parameter optimization,” in *Advances in Neural Information Processing Systems*, J. Shawe-Taylor, R. Zemel, P. Bartlett, *et al.*, Eds., vol. 24, Curran Associates, Inc., 2011, ISBN: 9781618395993. [Online]. Available: <https://dl.acm.org/doi/10.5555/2986459.2986743>.
- [58] F. Rosenblatt, “The Perceptron: A probabilistic model for information storage and organization in the brain,” *Psychol. Rev.*, vol. 65, no. 6, 386–408, 1958. DOI: [10.1037/h0042519](https://doi.org/10.1037/h0042519).
- [59] S. Ioffe and C. Szegedy, “Batch normalization: Accelerating deep network training by reducing internal covariate shift,” in *International conference on machine learning*, Pmlr, 2015, 448–456. arXiv: [1502.03167](https://arxiv.org/abs/1502.03167) [cs.LG].
- [60] F. Pedregosa, G. Varoquaux, A. Gramfort, *et al.*, “Scikit-learn: Machine learning in Python,” *J. Mach. Learn. Res.*, vol. 12, 2825–2830, 2011. [Online]. Available: <http://jmlr.org/papers/v12/pedregosa11a.html>.
- [61] A. Paszke, S. Gross, F. Massa, *et al.*, “PyTorch: An imperative style, high-performance deep learning library,” in *Advances in Neural Information Processing Systems 32*, H. Wallach, H. Larochelle, A. Beygelzimer, *et al.*, Eds., Curran Associates, Inc., 2019, 8024–8035. [Online]. Available: <https://dl.acm.org/doi/10.5555/3454287.3455008>.
- [62] W. Falcon and the PyTorch Lightning team, “Pytorch Lightning,” *GitHub. Lightning-AI/lightning*, 2019. DOI: [10.5281/zenodo.3828935](https://doi.org/10.5281/zenodo.3828935). [Online]. Available: <https://www.pytorchlightning.ai>.
- [63] C. R. Harris, K. J. Millman, S. J. van der Walt, *et al.*, “Array programming with NumPy,” *Nature*, vol. 585, no. 7825, 357–362, 2020. DOI: [10.1038/s41586-020-2649-2](https://doi.org/10.1038/s41586-020-2649-2).
- [64] T. Akiba, S. Sano, T. Yanase, *et al.*, “Optuna: A next-generation hyperparameter optimization framework,” in *Proceedings of the 25rd ACM SIGKDD International Conference on Knowledge Discovery and Data Mining*, 2019. arXiv: [1907.10902](https://arxiv.org/abs/1907.10902) [cs.LG].
- [65] A. Lacoste, A. Luccioni, V. Schmidt, *et al.*, “Quantifying the carbon emissions of machine learning,” 2019. arXiv: [1910.09700](https://arxiv.org/abs/1910.09700) [cs.CY]. [Online]. Available: <https://mlco2.github.io/impact/>.
- [66] Environmental Protection Agency (EPA), “Light-duty vehicle greenhouse gas emission standards and corporate average fuel economy standards: Final rule,” *Federal Register*, vol. 75, no. 88, 25324–25728, 2010. [Online]. Available: <https://www.govinfo.gov/content/pkg/FR-2010-05-07/pdf/2010-8159.pdf>.
- [67] O. Russakovsky, J. Deng, H. Su, *et al.*, “ImageNet large scale visual recognition challenge,” *Int. J. Comput. Vision*, vol. 115, no. 3, 211–252, 2015. DOI: [10.1007/s11263-015-0816-y](https://doi.org/10.1007/s11263-015-0816-y).
- [68] R. Balestriero, I. Misra, and Y. LeCun, “A data-augmentation is worth a thousand samples: Exact quantification from analytical augmented sample moments,” 2022. arXiv: [2202.08325](https://arxiv.org/abs/2202.08325) [cs.LG].
- [69] R. L. Figueroa, Q. Zeng-Treitler, S. Kandula, *et al.*, “Predicting sample size required for classification performance,” *BMC Med. Inf. Decis. Making*, vol. 12, no. 1, 1–10, 2012. DOI: [10.1186/1472-6947-12-8](https://doi.org/10.1186/1472-6947-12-8).
- [70] J. Cho, K. Lee, E. Shin, *et al.*, “How much data is needed to train a medical image deep learning system to achieve necessary high accuracy?,” 2015. arXiv: [1511.06348](https://arxiv.org/abs/1511.06348) [cs.LG].
- [71] X. Zhu, C. Vondrick, C. C. Fowlkes, *et al.*, “Do we need more training data?” *Int. J. Comput. Vision*, vol. 119, no. 1, 76–92, 2016. DOI: [10.1007/s11263-015-0812-2](https://doi.org/10.1007/s11263-015-0812-2).

-
- [72] S. Shahinfar, P. Meek, and G. Falzon, “How many images do i need? Understanding how sample size per class affects deep learning model performance metrics for balanced designs in autonomous wildlife monitoring,” *Ecol. Inf.*, vol. 57, 101085, 2020. DOI: [10.1016/j.ecoinf.2020.101085](https://doi.org/10.1016/j.ecoinf.2020.101085).
- [73] B. Juba and H. S. Le, “Precision-recall versus accuracy and the role of large data sets,” in *Proceedings of the AAAI Conference on Artificial Intelligence*, vol. 33, Jul. 2019, 4039–4048, ISBN: 978-1-57735-809-1. DOI: [10.1609/aaai.v33i01.33014039](https://doi.org/10.1609/aaai.v33i01.33014039).
- [74] M. S. Advani, A. M. Saxe, and H. Sompolinsky, “High-dimensional dynamics of generalization error in neural networks,” *Neural Networks*, vol. 132, 428–446, 2020. DOI: [10.1016/j.neunet.2020.08.022](https://doi.org/10.1016/j.neunet.2020.08.022).
- [75] M. Belkin, D. Hsu, S. Ma, *et al.*, “Reconciling modern machine learning practice and the bias-variance trade-off,” 2018. arXiv: [1812.11118](https://arxiv.org/abs/1812.11118) [stat.ML].
- [76] M. Geiger, S. Spigler, S. d’Ascoli, *et al.*, “Jamming transition as a paradigm to understand the loss landscape of deep neural networks,” *Phys. Rev. E*, vol. 100, no. 1, 012115, 2019. DOI: [10.1103/PhysRevE.100.012115](https://doi.org/10.1103/PhysRevE.100.012115).
- [77] P. Nakkiran, G. Kaplun, Y. Bansal, *et al.*, “Deep double descent: Where bigger models and more data hurt,” *J. Stat. Mech. Theory Exp.*, vol. 2021, no. 12, 124003, 2021. DOI: [10.1088/1742-5468/ac3a74](https://doi.org/10.1088/1742-5468/ac3a74).
- [78] I. Goodfellow, J. Pouget-Abadie, M. Mirza, *et al.*, “Generative adversarial nets,” in *Advances in Neural Information Processing Systems*, Z. Ghahramani, M. Welling, C. Cortes, *et al.*, Eds., vol. 27, Curran Associates, Inc., 2014. arXiv: [1406.2661](https://arxiv.org/abs/1406.2661) [stat.ML].
- [79] J. Sohl-Dickstein, E. Weiss, N. Maheswaranathan, *et al.*, “Deep unsupervised learning using nonequilibrium thermodynamics,” in *Proceedings of the 32nd International Conference on Machine Learning*, F. Bach and D. Blei, Eds., ser. Proceedings of Machine Learning Research, vol. 37, Lille, France: Pmlr, Jul. 2015, 2256–2265. [Online]. Available: <https://proceedings.mlr.press/v37/sohl-dickstein15.html>.
- [80] A. Ramesh, M. Pavlov, G. Goh, *et al.*, “Zero-shot text-to-image generation,” in *International Conference on Machine Learning*, Pmlr, 2021, 8821–8831. arXiv: [2102.12092](https://arxiv.org/abs/2102.12092) [cs.CV].
- [81] C. Saharia, W. Chan, S. Saxena, *et al.*, “Photorealistic text-to-image diffusion models with deep language understanding,” 2022. arXiv: [2205.11487](https://arxiv.org/abs/2205.11487) [cs.CV].
- [82] A. Alaa, B. Van Breugel, E. S. Saveliev, *et al.*, “How faithful is your synthetic data? Sample-level metrics for evaluating and auditing generative models,” in *International Conference on Machine Learning*, Pmlr, 2022, 290–306. arXiv: [2102.08921](https://arxiv.org/abs/2102.08921) [cs.LG].
- [83] S. Lipovetsky and M. Conklin, “Analysis of regression in game theory approach,” *Appl. Stochastic Models Bus. Ind.*, vol. 17, no. 4, 319–330, 2001. DOI: [10.1002/asmb.446](https://doi.org/10.1002/asmb.446).
- [84] E. Štrumbelj and I. Kononenko, “Explaining prediction models and individual predictions with feature contributions,” *Knowl. Inf. Sys.*, vol. 41, no. 3, 647–665, 2014. DOI: [10.1007/s10115-013-0679-x](https://doi.org/10.1007/s10115-013-0679-x).
- [85] M. T. Ribeiro, S. Singh, and C. Guestrin, “Why should i trust you? Explaining the predictions of any classifier,” in *Proceedings of the 22nd ACM SIGKDD international conference on knowledge discovery and data mining*, 2016, 1135–1144. DOI: [10.1145/2939672.2939778](https://doi.org/10.1145/2939672.2939778).
- [86] A. Vaswani, N. Shazeer, N. Parmar, *et al.*, “Attention is all you need,” in *Advances in Neural Information Processing Systems*, I. Guyon, U. V. Luxburg, S. Bengio, *et al.*, Eds., vol. 30, Curran Associates, Inc., 2017, 5998–6008. arXiv: [1706.03762](https://arxiv.org/abs/1706.03762) [cs.CL].

A Compositions of the Matrices

	Type	Salt	[Cl] wt%
training samples	CEM I	NaCl	0.06
	CEM I	NaCl	0.19
	CEM I	NaCl	0.32
	CEM I	NaCl	0.46
	CEM I	NaCl	0.59
	CEM I	NaCl	0.72
	CEM I	NaCl	0.85
	CEM I	NaCl	0.98
	CEM I	NaCl	1.15
	CEM I	NaCl	1.43
	CEM I	NaCl	1.71
	CEM I	NaCl	1.95
test samples	CEM I	NaCl	1.51
	CEM I	NaCl	1.02
	CEM I	NaCl	0.23
	CEM II/B-LL	NaCl	0.41
	CEM III/A	NaCl	0.87
	CEM I	KCl	0.59
	CEM I	NaCl	0.50

Table A.1. Elemental composition of the cement matrices. *The type of cement and the salt used in fabrication are specified on a sample basis.*

Matrix	Aluminium					Cobalt					Copper					Nickel			
Sample	51XG00H2	35831	63698	52963	68404	IMZ 188	BS171C	ECRM3781D	BSMP35N	IMZ 186	CT1	CT2	CT3	CT4	CT5	B7011	B7012	B7004	F294
Ag						(0.005)	(0.04)		0.047	0.28	0.057	0.042	0.026	0.016	0.0062				
Al	98.35	97.49	95.08	98.73	98.00											1.2	1.25	1.64	0.05
As	0.005										0.32	0.22	0.11	0.05	0.0056				
B						0.0009	(0.004)		0.0034	(0.007)	0.024	0.033	0.00093	0.0042	0.011				
Be																			
Bi	0.011										0.018	0.013	0.0067	0.0043	0.0011				
C						0.0526	0.119	1.181	0.009	0.59						0.095	0.16	0.01	
Ca																			
Cd	0.0031																		
Ce																			
Co						51.64	51.2	63.52	33.2	54.123	0.051	0.033	0.013	0.011	0.0061	17	17	0.06	0.51
Cr	0.0174	0.0023	0.03	0.03	0.03	26.44	20.3	28.22	20.4	23.14						19.7	19.65	19.6	0.04
Cu	0.111	0.065	0.4	0.02	0.1	0.025	(0.02)		(0.014)		97.77	99.66	99.84	99.91	99.97	0.065	0.11	0.14	0.11
Fe	0.356	0.558	0.81	0.11	0.41	1.14	1.07	0.606	0.327	0.10	0.17	0.1	0.083	0.045	0.016	0.34	0.25	0.97	0.06
H																			
Hf																			
Ga	0.011																		
Ge																			
La							(0.03)												
Mg	0.093	0.208	1.36	0.93	0.01		(0.001)		<0.01										0.02
Mn	0.154	0.108	0.69	0.03	1.15	0.68	1.47	0.0579	0.008							0.16	0.53	0.08	0.1
Mo						0.42	(0.08)	0.053	9.7							0.2	0.39	0.06	
N																			
Na																			
Nb						0.045	(0.006)		0.017										
Ni	0.119	0.0575			0.02	10.76	10.1	0.617	35.6	10.22	0.48	0.29	0.12	0.049	0.0095	58.17	57.99	74.64	98.99
O							(0.002)		(0.0004)										
P						0.011	(0.008)	(0.0023)	<0.01		0.082	0.059	0.038	0.02	0.0059				
Pb	0.114	0.08			0.02						0.013	0.086	0.31	0.88	1.48				
Pd																			
Ru																			
S						(0.0002)	(0.0008)	0.0055	<0.01		0.054	0.036	0.012	0.006	0.0024				
Sb	0.0265										0.33	0.24	0.11	0.049	0.01				
Se											0.062	0.041	0.018	0.011	0.0069				
Si	0.35	1.1	1.33	0.05	0.16	0.69	(0.1)	1.172	<0.05							1.02	0.39	0.17	0.09
Sn	0.0065	0.051			0.02				<0.01		0.24	0.14	0.07	0.025	0.007				
Ta						(0.011)	(0.02)		0.0021	3.78									
Te											0.053	0.036	0.022	0.011	0.0064				
Ti	0.128	0.166	0.06	0.06	0.065	(0.007)	(0.07)		0.75	0.19						2.05	2.28	2.63	0.03
V	0.0148					(0.011)	(0.009)		0.0095										
W						7.46	15.3	4.43	<0.05	7.17									
Y																			
Zn	0.113	0.111	0.24	0.04	0.02						0.28	0.19	0.11	0.045	0.0098				
Zr	0.015					(0.0004)	(0.01)		(0.002)	0.40									

Table A.2. Elemental composition of the alloy matrices (part 1). *The concentration of the analyte is in bold characters.*

Matrix	Tin						Titanium					Zinc					Zirconium					
Sample	IMNL891	IMNL892	IMNL893	IMNL894	IMNL895	IMNL896	BST26	BST80	BST81	BST22	BSTSU-1	43XZ5B	43XZ9A	43XGALF1A	43XSC2A	43XSC3A	ET1	ET2	ET3	ET4	ET5	
Ag												0.0254										
Al							0.002	0.0746	0.0664	0.004	6.11	3.164	3.17	4.68	3.41	3.14	0.00133	0.00158	0.01329	0.04384	0.09514	
As	0.019	0.037	0.065	0.12	0.18	0.029						(0.0005)										
B								0.004	0.0082		0.01						0.00002		0.00043	0.00071	0.0016	
Be													0.0010									
Bi	0.012	0.026	0.052	0.099	0.20	0.014						0.0148	0.0033									
C							0.005	0.0166	0.0161	0.005	0.062						0.01068	0.01313	0.02173	0.04876	0.10422	
Ca																	0.00013	0.00012	0.00024	0.00035	0.00031	
Cd	0.19	0.091	0.041	0.021	0.011	0.19						0.0030	0.0034	0.0499	0.0018	0.0028	0.00001		0.00005	0.00008	0.00019	
Ce														0.0569								
Co								0.0146	0.0395		0.061						0.00018	0.00015	0.01323	0.05727	0.11297	
Cr							0.037	0.005	0.0294	1.22	0.07		0.0034		0.023	0.0108	0.0028	0.04902	0.10377	0.13103	0.17657	
Cu	3.20	4.15	3.49	2.81	2.12	4.51	0.037	0.0375	0.0244	0.04	0.073	5.92	4.82	4.39	4.80	3.03	0.00024	0.0004	0.01342	0.04265	0.08438	
Fe	0.18	0.086	0.058	0.028	0.013	0.17	0.055	0.0093	0.1144	1.19	0.22	0.10	0.073	0.061	0.046	0.018	0.02277	0.0964	0.28288	0.25304	0.30892	
H								0.0059	0.0035													
Hf																	0.00514	0.00517	0.02035	0.05694	0.10917	
Ga																						
Ge																						
La														0.0284								
Mg							0.002			0.003	0.005	0.0144	0.0472	0.0999	0.498	0.257	0.00002				0.00006	0.00003
Mn							0.006	0.0244	0.0404	2.02	0.065	0.0061	0.0108		0.0183	0.0337	0.00011	0.0001	0.00218	0.01124	0.01667	
Mo							0.028	0.01	0.0279	1.15	0.067						0.00001		0.01566	0.04978	0.12482	
N							0.005	0.0041	0.0037	0.01	0.02						0.00169	0.00276	0.00992	0.01286	0.01885	
Na																		0.00001				
Nb							0.01	0.0367	0.0191	0.01	0.068						0.00085	0.0011	0.0152	0.04324	0.11919	
Ni	0.010	0.031	0.090	0.16	0.33	0.014	0.002	0.0156	0.009	0.008	0.073	0.0056	0.0027		0.0096	0.0261	0.00087	0.03309	0.01692	0.0987	0.15731	
O							0.069	0.0768	0.0669	0.09	0.191						0.0708	0.1443	0.17979	0.1623	0.1942	
P											0.009						0.00003		0.00111	0.0017	0.00255	
Pb	0.072	0.13	0.29	0.52	1.11	0.20						0.0029	0.0078	0.0505	0.0097	0.0066			0.00299	0.01203	0.01684	
Pd								0.1424	0.0398		0.15											
Ru								0.0469	0.031		0.07											
S							0.001			0.002	0.008											
Sb	5.66	6.39	7.41	8.14	8.86	8.03						0.065	0.0033									
Se																						
Si							0.01		0.0474	0.02	0.057						0.00005	0.00374	0.02142	0.05541	0.10567	
Sn	90.558	89	88.462	88.082	87.176	86.747	0.025	0.0257	0.0155	0.019	0.076	(0.0004)	0.0020	0.0514	0.0133	0.0078	0.0084	0.6902	1.2336	1.1331	1.681	
Ta											0.079						0.00013	0.00017	0.00729	0.05239	0.11212	
Te																						
Ti							99.11	99.37	99.32	93.19	88.18		0.0012				0.00039	0.0005	0.00774	0.03895	0.10169	
V							0.02	0.0446	0.0186	0.5	4.12						0.00009	0.00037	0.00651	0.03808	0.09808	
W							0.57	0.0174	0.0372	0.51	0.075						0.00067	0.00038	0.00607	0.04448	0.09469	
Y								0.001	0.0017		0.009											
Zn	0.099	0.059	0.042	0.020		0.096	0.005	0.0178	0.0163	0.01	0.068	90.6779	91.8509	90.532	91.1672	93.4452	0.00018	0.00021	0.00042	0.00101	0.00144	
Zr																	99.87241	98.9571	98.00379	97.61	96.16138	

Table A.3. Elemental composition of the alloy matrices (part 2). *The concentration of the analyte is in bold characters.*

B Implementation Details

Wavelength (nm)	Integration interval (nm)	Relative intensity	Spectrum
358.12	358.11 – 358.14	600	Fe I
373.49	373.47 – 373.51	700	Fe I
373.71	373.69 – 373.73	600	Fe I
374.56	374.54 – 374.58	600	Fe I
382.04	382.02 – 382.06	500	Fe I
385.99	385.97 – 386.01	500	Fe I
404.58	404.56 – 404.60	300	Fe I
438.35	438.33 – 438.37	200	Fe I

Table B.1. Wavelengths corresponding to persistent emission lines of Fe. *Integration intervals used as secondary outputs of the multitask architecture are also presented.*

Matrix	Wavelength (nm)	Integration interval (nm)
Al	396.15	396.13 – 396.18
Co	345.35	345.33 – 345.67
Cu	324.75	324.74 – 324.77
Ni	352.45	352.43 – 352.46
Sn	326.23	326.21 – 326.25
Ti	399.86	399.84 – 399.87
Zn	334.50	334.49 – 334.52
Zr	360.12	360.10 – 360.14

Table B.2. Normalisation wavelengths of the alloy matrices. *Integration intervals are specified for each matrix.*

PLS1 Components		
Matrix	Experimental data	Synthetic data (N = 1000)
Al	2	2
Co	6	8
Cu	1	8
Ni	1	1
Sn	1	1
Ti	7	4
Zn	3	3
Zr	4	3
Cement	2	2

Table B.3. Number of components used in the PLS1 model. *5-fold cross validation was used to determine the best value of the hyperparameter.*

Hyperparameter	Value		
	Alloys	Cement	
φ	0.995	0.995	
ℓ_1	0	0	
ℓ_2	3×10^{-5}	0	
learning rate	10^{-4}	10^{-3}	
$\hat{\alpha}_0$	0.91	0.93	
η	0.99	0.99	
δ	1.97	0	
weight decay	1.5×10^{-3}	3×10^{-5}	
parameter sharing	slope	0	5×10^{-3}
	batch normalisation	yes	no
	depth	4	2
	channels	80, 40, 8, 112	128, 164
	dropout	0.15, 0, 0, 0.30	0.1, 0.0
	kernels	4, 4, 10, 4	10, 6
	strides	2, 4, 4, 3	1, 3
heads	slope	1.2×10^{-4}	3×10^{-4}
	batch normalisation	yes	yes
	depth (CNN + FCNN)	4 + 2	3 + 1
	channels	112, 108, 132, 80	100, 24, 120
	dropout	0.05, 0.30, 0, 0.20	0.1, 0.2, 0.2
	kernels	10, 6, 2, 6	10, 2, 6
	strides	2, 3, 3, 3	2, 1, 1
fully connected units	32, 56	64	

Table B.4. List of hyperparameters used for the MT model. *Symbols are introduced in Section 4.6.*

C Results

X	Matrix	[X] wt %	Predicted [X] wt %				RMSE wt %				MAE wt %				MAPE (%)			
			LR	MLR	PLS1	FCNN	LR	MLR	PLS1	FCNN	LR	MLR	PLS1	FCNN	LR	MLR	PLS1	FCNN
Fe	Al	0.11	0.13	0.15	0.17	0.13	0.05	0.05	0.07	0.04	0.04	0.04	0.06	0.02	36	39	57	22
		0.36	0.39	0.34	0.37	0.35	0.10	0.06	0.07	0.08	0.10	0.05	0.06	0.07	28	15	18	20
		0.41	0.45	0.43	0.45	0.39	0.09	0.06	0.08	0.04	0.08	0.05	0.06	0.04	18	13	16	10
		0.56	0.71	0.66	0.69	0.62	0.17	0.13	0.15	0.10	0.15	0.11	0.13	0.09	27	19	24	15
		0.81	0.63	0.67	0.70	0.58	0.22	0.18	0.16	0.29	0.18	0.15	0.13	0.26	22	18	16	32
	Co	0.10	0.03	0.16	0.05	0.11	0.14	0.10	0.09	0.02	0.11	0.08	0.08	0.02	106	78	76	18
		0.33	0.51	0.34	0.23	0.34	0.27	0.10	0.14	0.11	0.24	0.08	0.12	0.08	74	24	38	24
		0.61	0.65	0.49	0.38	0.56	0.17	0.19	0.27	0.14	0.15	0.14	0.23	0.12	24	24	37	20
		1.07	1.07	1.17	1.06	1.14	0.06	0.20	0.18	0.10	0.05	0.16	0.15	0.08	5	15	14	8
		1.14	1.07	1.08	0.97	1.10	0.10	0.12	0.20	0.05	0.08	0.11	0.18	0.04	7	9	15	4
	Cu	0.02	0.03	0.03	0.03	0.03	0.03	0.02	0.02	0.02	0.02	0.02	0.014	0.014	121	106	89	85
		0.05	0.05	0.05	0.04	0.05	0.02	0.01	0.01	0.02	0.02	0.01	0.01	0.02	37	22	25	38
		0.08	0.11	0.11	0.10	0.13	0.04	0.03	0.03	0.06	0.03	0.03	0.02	0.05	38	30	27	59
		0.10	0.11	0.11	0.09	0.13	0.04	0.05	0.03	0.05	0.03	0.03	0.03	0.03	27	34	30	33
		0.17	0.13	0.18	0.16	0.20	0.05	0.12	0.13	0.11	0.04	0.07	0.09	0.05	25	43	50	32
	Ni	0.06	0.01	0.08	0.10	0.06	0.07	0.03	0.04	0.001	0.06	0.02	0.04	0.001	107	32	61	1
		0.25	0.28	0.26	0.32	0.26	0.06	0.03	0.08	0.02	0.05	0.03	0.07	0.02	21	11	28	7
		0.34	0.40	0.35	0.41	0.32	0.10	0.05	0.09	0.03	0.07	0.04	0.07	0.02	21	11	20	7
		0.97	0.92	0.91	0.94	0.95	0.18	0.16	0.15	0.04	0.15	0.15	0.14	0.02	15	15	14	2
		Sn	0.01	0.02	0.02	0.02	0.02	0.02	0.014	0.008	0.007	0.02	0.01	0.006	0.006	148	82	45
0.03	0.06		0.06	0.05	0.05	0.04	0.04	0.03	0.04	0.03	0.03	0.02	0.02	106	123	74	80	
0.06	0.08		0.07	0.06	0.06	0.03	0.02	0.01	0.02	0.02	0.02	0.01	0.02	41	27	13	31	
0.09	0.11		0.09	0.08	0.10	0.04	0.03	0.02	0.04	0.03	0.02	0.02	0.03	39	25	19	35	
0.17	0.14		0.14	0.12	0.14	0.05	0.06	0.07	0.05	0.03	0.06	0.06	0.03	19	34	35	20	
0.18	0.14	0.14	0.12	0.14	0.05	0.05	0.07	0.05	0.04	0.05	0.06	0.04	23	26	33	22		
Ti	0.01	0.00	0.01	0.01	0.02	0.07	0.04	0.04	0.03	0.06	0.03	0.03	0.014	646	368	370	154	
	0.06	0.11	0.09	0.09	0.07	0.12	0.07	0.07	0.03	0.08	0.06	0.06	0.03	147	105	105	56	
	0.11	0.04	0.11	0.11	0.09	0.08	0.04	0.04	0.04	0.07	0.03	0.03	0.03	63	26	26	24	
	0.22	0.20	0.26	0.26	0.19	0.09	0.09	0.09	0.06	0.07	0.08	0.08	0.05	30	36	36	22	
	1.19	1.02	1.14	1.14	1.19	0.30	0.1	0.1	0.007	0.25	0.1	0.1	0.005	21	9	9	0.4	
Zn	0.02	0.05	0.05	0.05	0.06	0.03	0.03	0.03	0.04	0.03	0.03	0.03	0.04	162	190	151	213	
	0.05	0.05	0.06	0.05	0.06	0.005	0.03	0.02	0.01	0.004	0.02	0.014	0.01	9	34	31	23	
	0.06	0.04	0.07	0.07	0.06	0.09	0.03	0.03	0.004	0.04	0.02	0.02	0.004	69	32	35	7	
	0.07	0.06	0.07	0.06	0.06	0.014	0.02	0.02	0.02	0.01	0.02	0.02	0.02	17	24	30	22	
	0.10	0.06	0.06	0.06	0.06	0.05	0.04	0.05	0.04	0.04	0.04	0.04	0.04	43	40	45	43	
Zr	0.02	0.12	0.08	0.08	0.08	0.12	0.07	0.07	0.09	0.10	0.06	0.06	0.06	441	262	248	250	
	0.10	0.19	0.13	0.13	0.12	0.11	0.04	0.04	0.06	0.09	0.03	0.03	0.04	94	35	31	40	
	0.25	0.23	0.26	0.25	0.26	0.06	0.06	0.06	0.05	0.04	0.05	0.05	0.04	15	20	20	16	
	0.28	0.26	0.28	0.27	0.21	0.03	0.08	0.08	0.11	0.03	0.05	0.06	0.08	10	19	20	27	
	0.31	0.27	0.36	0.35	0.31	0.04	0.08	0.08	0.01	0.03	0.06	0.06	0.007	11	21	20	2	
Cement	0.23	0.23	0.23	0.34	0.22	0.04	0.04	0.12	0.03	0.03	0.03	0.11	0.03	13	13	49	11	
	0.41	0.44	0.44	0.56	0.42	0.09	0.09	0.17	0.09	0.07	0.07	0.15	0.07	17	17	36	18	
	0.50	0.55	0.55	0.66	0.53	0.10	0.10	0.18	0.09	0.08	0.08	0.16	0.07	15	15	32	14	
	0.59	0.61	0.61	0.73	0.60	0.07	0.07	0.15	0.06	0.06	0.06	0.14	0.04	9	9	23	7	
	0.87	1.14	1.14	1.26	1.16	0.30	0.30	0.40	0.31	0.27	0.27	0.39	0.29	32	32	44	33	
	1.02	1.03	1.03	1.14	1.01	0.08	0.08	0.15	0.09	0.07	0.07	0.13	0.07	7	7	13	7	
	1.51	1.49	1.49	1.60	1.53	0.10	0.10	0.13	0.11	0.08	0.08	0.11	0.09	5	5	7	6	

Table C.1. Results of the analysis for traditional algorithms with experimental data. Results of inference are relative to the independent test set. The columns show the Root Mean Squared Error (RMSE), the Mean Absolute Error (MAE), and the Mean Absolute Percentage Error (MAPE). The algorithms refer to Linear Regression (LR), Multivariate Linear Regression (MLR), Partial Least Squares (PLS1), and Fully Connected Neural Networks (FCNN). Bold characters represent the best estimates.

X	Matrix	[X] wt %	Predicted [X] wt %				RMSE wt %				MAE wt %				MAPE (%)			
			LR	MLR	PLS1	FCNN	LR	MLR	PLS1	FCNN	LR	MLR	PLS1	FCNN	LR	MLR	PLS1	FCNN
Fe	Al	0.11	0.10	0.13	0.12	0.11	0.07	0.05	0.04	0.03	0.06	0.04	0.04	0.02	52	38	33	20
		0.36	0.34	0.34	0.32	0.35	0.09	0.07	0.07	0.07	0.09	0.05	0.05	0.05	24	15	15	15
		0.41	0.45	0.43	0.42	0.44	0.07	0.05	0.05	0.04	0.05	0.04	0.04	0.03	12	9	9	7
		0.56	0.64	0.61	0.60	0.62	0.10	0.10	0.09	0.08	0.09	0.09	0.08	0.06	16	16	14	11
		0.81	0.62	0.67	0.66	0.65	0.21	0.16	0.17	0.18	0.19	0.14	0.15	0.16	24	17	19	20
	Co	0.10	0.15	0.16	0.02	0.18	0.21	0.12	0.13	0.12	0.19	0.09	0.11	0.08	191	89	110	83
		0.33	0.36	0.36	0.22	0.40	0.13	0.11	0.14	0.09	0.11	0.10	0.11	0.08	33	31	32	23
		0.61	0.52	0.50	0.36	0.55	0.17	0.16	0.27	0.18	0.16	0.15	0.25	0.16	27	25	41	27
		1.07	1.06	1.09	0.96	1.10	0.15	0.16	0.20	0.07	0.13	0.13	0.17	0.07	12	12	16	6
		1.14	0.97	1.00	0.87	1.07	0.22	0.17	0.29	0.09	0.17	0.14	0.27	0.07	15	12	24	6
	Cu	0.02	0.04	0.03	0.02	0.02	0.03	0.014	0.01	0.01	0.02	0.01	0.008	0.009	130	68	52	56
		0.05	0.05	0.04	0.04	0.05	0.02	0.02	0.02	0.03	0.02	0.014	0.02	0.02	36	31	38	49
		0.08	0.09	0.10	0.10	0.11	0.03	0.06	0.06	0.04	0.03	0.04	0.04	0.03	31	45	46	31
		0.10	0.08	0.09	0.09	0.10	0.02	0.03	0.03	0.02	0.02	0.02	0.03	0.01	20	22	26	12
		0.17	0.13	0.15	0.15	0.14	0.05	0.05	0.05	0.05	0.04	0.04	0.04	0.04	26	24	25	24
	Ni	0.06	0.10	0.11	0*	0.07	0.04	0.05	0.09	0.009	0.04	0.05	0.08	0.007	66	80	142	11
		0.25	0.26	0.26	0.21	0.28	0.05	0.03	0.05	0.04	0.04	0.03	0.05	0.03	16	10	18	12
		0.34	0.38	0.35	0.27	0.33	0.07	0.04	0.08	0.02	0.06	0.03	0.07	0.01	19	9	20	4
		0.97	0.89	0.89	0.79	0.93	0.18	0.12	0.21	0.06	0.15	0.10	0.18	0.04	15	10	19	5
		0.01	0.01	0.02	0.03	0.02	0.02	0.01	0.014	0.006	0.014	0.008	0.01	0.004	105	63	92	34
Sn	0.03	0.04	0.05	0.05	0.04	0.03	0.02	0.02	0.01	0.02	0.02	0.02	0.01	84	70	80	29	
	0.06	0.06	0.06	0.06	0.04	0.02	0.02	0.02	0.02	0.02	0.02	0.02	0.01	29	29	30	25	
	0.09	0.10	0.10	0.09	0.12	0.03	0.02	0.02	0.05	0.03	0.02	0.013	0.04	30	23	15	49	
	0.17	0.14	0.14	0.14	0.14	0.05	0.06	0.05	0.05	0.04	0.05	0.05	0.04	21	31	27	21	
	0.18	0.13	0.13	0.13	0.16	0.05	0.06	0.06	0.04	0.05	0.05	0.05	0.02	25	30	30	14	
Ti	0.01	0.04	0*	0*	0.02	0.10	0.04	0.05	0.25	0.07	0.03	0.04	0.015	787	371	467	158	
	0.06	0.13	0.09	0.08	0.08	0.16	0.07	0.07	0.08	0.13	0.07	0.07	0.05	237	127	124	82	
	0.11	0.15	0.15	0.13	0.11	0.08	0.07	0.06	0.11	0.05	0.06	0.05	0.03	46	49	43	24	
	0.22	0.27	0.30	0.29	0.22	0.09	0.11	0.10	0.14	0.08	0.08	0.07	0.03	37	38	33	14	
	1.19	1.19	1.12	1.11	1.10	0.25	0.14	0.14	0.22	0.20	0.12	0.1	0.11	17	10	11	9.1	
Zn	0.02	0.05	0.06	0.05	0.06	0.04	0.04	0.03	0.04	0.04	0.04	0.03	0.04	196	218	153	223	
	0.05	0.06	0.06	0.05	0.06	0.014	0.02	0.01	0.01	0.01	0.012	0.007	0.01	28	27	16	26	
	0.06	0.03	0.09	0.09	0.06	0.05	0.07	0.08	0.003	0.03	0.04	0.05	0.002	47	59	86	4	
	0.07	0.07	0.07	0.07	0.06	0.01	0.02	0.04	0.01	0.01	0.02	0.03	0.014	15	24	44	20	
	0.10	0.07	0.07	0.07	0.06	0.03	0.05	0.04	0.04	0.03	0.04	0.04	0.04	28	42	40	41	
Zr	0.02	0.05	0.04	0.07	0.01	0.07	0.03	0.06	0.02	0.05	0.03	0.05	0.02	240	117	226	80	
	0.10	0.16	0.11	0.14	0.08	0.09	0.03	0.05	0.05	0.07	0.02	0.05	0.04	69	22	49	43	
	0.25	0.22	0.23	0.26	0.25	0.06	0.05	0.04	0.06	0.04	0.04	0.03	0.04	17	17	14	16	
	0.28	0.25	0.23	0.26	0.25	0.03	0.07	0.06	0.04	0.03	0.06	0.05	0.03	10	20	17	12	
	0.31	0.27	0.33	0.36	0.30	0.05	0.11	0.12	0.03	0.04	0.10	0.10	0.02	14	32	32	6	
Cl	Cement	0.23	0.25	0.24	0.35	0.21	0.04	0.04	0.13	0.04	0.03	0.03	0.12	0.03	14	13	54	13
		0.41	0.45	0.45	0.56	0.41	0.08	0.09	0.17	0.08	0.07	0.07	0.16	0.06	16	17	38	16
		0.50	0.54	0.55	0.66	0.51	0.09	0.10	0.18	0.08	0.07	0.08	0.16	0.06	14	15	33	12
		0.59	0.60	0.61	0.72	0.58	0.07	0.07	0.15	0.07	0.06	0.06	0.13	0.05	9	10	23	9
		0.87	1.12	1.13	1.24	1.09	0.28	0.28	0.39	0.26	0.25	0.26	0.37	0.22	29	30	43	26
		1.02	1.01	1.03	1.14	0.98	0.07	0.07	0.14	0.08	0.06	0.06	0.13	0.06	6	6	13	6
		1.51	1.48	1.48	1.60	1.46	0.12	0.11	0.14	0.13	0.10	0.09	0.11	0.11	6	6	7	7

Table C.2. Results of the analysis for traditional algorithms with synthetic data. *The size of the training set is fixed to 1000 spectra per sample for alloys, and 100 spectra per sample for cement matrices. Results of inference are relative to the independent test set. The columns show the Root Mean Squared Error (RMSE), the Mean Absolute Error (MAE), and the Mean Absolute Percentage Error (MAPE). The algorithms refer to Linear Regression (LR), Multivariate Linear Regression (MLR), Partial Least Squares (PLS1), and Fully Connected Neural Networks (FCNN). Bold characters represent the best estimates (*negative prediction, set to zero).*

X	Matrix	[X] wt %	Predicted [X] wt %						RMSE wt %						MAE wt %						MAPE (%)					
			MT (training size)						MT (training size)						MT (training size)						MT (training size)					
			Best	Exp	100	1000	5000	10000	Best	Exp	100	1000	5000	10000	Best	Exp	100	1000	5000	10000	Best	Exp	100	1000	5000	10000
Fe	Al	0.11	0.13 ⁴	0.08	0.01	0.11	0.21	0.23	0.04	0.05	0.11	0.02	0.10	0.13	0.02	0.04	0.10	0.013	0.10	0.12	22	95	87	12	86	51
		0.36	0.34 ²	0.11	0.12	0.32	0.48	0.61	0.06	0.25	0.25	0.09	0.15	0.26	0.05	0.24	0.24	0.09	0.13	0.25	15	300	68	24	36	40
		0.41	0.39 ⁴	0.15	0.16	0.42	0.70	0.70	0.04	0.26	0.25	0.02	0.30	0.30	0.04	0.26	0.25	0.02	0.29	0.29	10	170	60	4	71	40
		0.56	0.62 ⁴	0.13	0.30	0.53	0.66	0.73	0.10	0.43	0.26	0.04	0.10	0.17	0.09	0.43	0.26	0.03	0.10	0.17	15	400	46	6	18	23
	0.81	0.67 ²	0.07	0.32	0.77	0.82	0.84	0.20	0.74	0.50	0.05	0.03	0.05	0.15	0.74	0.49	0.04	0.02	0.04	18	3000	60	5	2	5	
	Co	0.10	0.11 ⁴	0.04	0.08	0.08	0.22	0.23	0.02	0.07	0.09	0.03	0.18	0.19	0.02	0.06	0.07	0.02	0.12	0.13	18	170	71	23	38	41
		0.33	0.34 ⁴	0.06	0.31	0.31	0.32	0.37	0.11	0.27	0.29	0.05	0.004	0.05	0.08	0.26	0.28	0.04	0.004	0.05	24	1700	84	12	1	12
		0.61	0.56 ⁴	0.09	0.64	0.64	0.65	0.71	0.14	0.53	0.19	0.04	0.05	0.11	0.12	0.52	0.19	0.03	0.05	0.10	20	47000	31	5	7	14
		1.07	1.07 ¹	0.07	1.07	1.07	1.02	1.05	0.06	1.00	0.12	0.02	0.05	0.03	0.05	1.00	0.09	0.02	0.05	0.02	5	1900	9	2	5	2
		1.14	1.10 ⁴	0.09	1.14	1.14	1.04	1.08	0.05	1.05	0.21	0.01	0.11	0.07	0.04	1.05	0.20	0.006	0.10	0.06	4	630	17	1	10	6
	Cu	0.02	0.03 ⁴	0*	0*	0.02	0.06	0.08	0.02	0.08	0.08	0.01	0.05	0.07	0.01	0.08	0.08	0.01	0.04	0.06	85	140	500	63	261	80
		0.05	0.05 ²	0*	0.03	0.05	0.07	0.09	0.013	0.10	0.04	0.01	0.03	0.04	0.01	0.08	0.03	0.007	0.03	0.04	22	21	76	16	60	48
		0.08	0.10 ³	0.03	0.00	0.11	0.14	0.12	0.03	0.08	0.09	0.03	0.06	0.04	0.02	0.07	0.08	0.03	0.05	0.04	27	190	100	31	66	30
		0.10	0.11 ¹	0.01	0.03	0.13	0.14	0.12	0.04	0.10	0.08	0.03	0.04	0.02	0.03	0.09	0.07	0.03	0.04	0.02	27	220	70	32	39	14
		0.17	0.17 ¹	0*	0.02	0.17	0.15	0.14	0.05	0.20	0.16	0.01	0.02	0.03	0.04	0.19	0.15	0.01	0.02	0.03	25	160	90	6	9	25
	Ni	0.06	0.06 ⁴	0*	0*	0.06	0.06	0.06	0.001	0.09	0.11	0.01	0.002	0.0013	0.0009	0.08	0.11	0.007	0.0014	0.001	1	77	183	12	2	2
		0.25	0.26 ⁴	0*	0*	0.24	0.26	0.25	0.02	0.37	0.42	0.03	0.01	0.003	0.02	0.36	0.42	0.02	0.008	0.002	7	460	169	8	3	1
		0.34	0.32 ⁴	0*	0*	0.33	0.34	0.33	0.03	0.46	0.51	0.02	0.004	0.02	0.02	0.46	0.51	0.02	0.004	0.01	7	440	150	5	1	4
		0.97	0.95 ⁴	0*	0.02	0.94	0.94	0.88	0.04	1.10	0.96	0.05	0.03	0.10	0.02	1.10	0.95	0.04	0.03	0.09	2	1200	98	4	3	10
	Sn	0.01	0.02 ³	0*	0*	0.002	0.01	0.02	0.007	0.20	0.11	0.01	0.003	0.005	0.01	0.20	0.11	0.01	0.002	0.004	45	110	830	85	11	17
0.03		0.05 ³	0*	0*	0.02	0.03	0.03	0.03	0.29	0.12	0.01	0.006	0.01	0.02	0.28	0.12	0.01	0.005	0.009	74	110	440	33	20	36	
0.06		0.06 ³	0*	0*	0.05	0.04	0.05	0.01	0.26	0.13	0.01	0.03	0.01	0.01	0.25	0.13	0.007	0.02	0.008	13	130	220	12	104	18	
0.09		0.08 ³	0*	0*	0.07	0.09	0.08	0.02	0.24	0.16	0.02	0.01	0.02	0.02	0.23	0.16	0.02	0.006	0.015	19	180	190	22	7	29	
0.17		0.14 ¹	0*	0*	0.13	0.15	0.14	0.05	0.34	0.21	0.05	0.04	0.05	0.03	0.33	0.20	0.04	0.02	0.03	19	210	120	24	23	36	
0.18		0.14 ⁴	0*	0*	0.14	0.16	0.16	0.05	0.35	0.23	0.05	0.02	0.03	0.04	0.35	0.23	0.04	0.02	0.02	22	220	130	22	12	16	
Ti	0.01	0.02 ⁴	0.09	0*	0.05	0.12	0.18	0.03	0.10	0.10	0.04	0.11	0.17	0.01	0.08	0.09	0.04	0.11	0.17	154	87	950	421	91	95	
	0.06	0.07 ⁴	0.06	0*	0.10	0.20	0.23	0.03	0.07	0.11	0.06	0.15	0.18	0.03	0.06	0.10	0.05	0.14	0.18	56	260	190	92	71	76	
	0.11	0.09 ⁴	0.07	0*	0.15	0.22	0.26	0.04	0.06	0.16	0.05	0.12	0.15	0.03	0.05	0.16	0.05	0.11	0.15	24	340	140	47	46	56	
	0.22	0.19 ⁴	0.09	0*	0.24	0.22	0.29	0.06	0.14	0.27	0.04	0.03	0.07	0.05	0.13	0.26	0.04	0.02	0.07	22	790	120	20	10	22	
	1.19	1.19 ⁴	0.13	1.12	1.15	1.13	1.16	0.007	1.06	0.23	0.05	0.06	0.04	0.01	1.06	0.21	0.04	0.06	0.03	0.4	960	18	4	5	3	
Zn	0.02	0.05 ³	0.12	0.06	0.02	0.02	0.03	0.03	0.10	0.05	0.01	0.008	0.01	0.03	0.10	0.04	0.01	0.007	0.008	156	84	240	50	24	25	
	0.05	0.05 ¹	0.08	0.03	0.04	0.04	0.04	0.005	0.04	0.03	0.01	0.008	0.008	0.004	0.03	0.02	0.01	0.005	0.005	9	38	47	18	16	14	
	0.06	0.06 ⁴	0.07	0.03	0.06	0.05	0.05	0.004	0.02	0.03	0.008	0.01	0.01	0.004	0.01	0.03	0.007	0.009	0.007	7	14	51	11	20	19	
	0.07	0.06 ¹	0.04	0.06	0.07	0.07	0.07	0.014	0.05	0.03	0.01	0.01	0.008	0.01	0.04	0.02	0.01	0.004	0.004	17	470	32	11	11	7	
	0.10	0.06 ²	0.07	0.07	0.09	0.10	0.10	0.04	0.04	0.03	0.008	0.005	0.003	0.04	0.03	0.03	0.007	0.004	0.002	40	63	29	7	4	3	
Zr	0.02	0.08 ⁴	0.22	0.08	0.03	0.02	0.03	0.09	0.21	0.08	0.01	0.0014	0.003	0.06	0.20	0.06	0.006	0.001	0.003	250	89	280	28	4	10	
	0.10	0.13 ²	0.24	0.14	0.10	0.10	0.10	0.04	0.15	0.07	0.003	0.0008	0.0007	0.03	0.15	0.06	0.003	0.0008	0.0005	35	59	59	3	1	0.5	
	0.25	0.23 ¹	0.22	0.26	0.26	0.25	0.25	0.06	0.05	0.06	0.003	0.0009	0.0015	0.04	0.03	0.05	0.002	0.0009	0.0013	15	18	20	1.0	0.4	0.5	
	0.28	0.26 ¹	0.31	0.38	0.28	0.28	0.28	0.03	0.04	0.11	0.001	0.001	0.0014	0.03	0.03	0.09	0.001	0.001	0.0013	10	10	33	0.3	0.4	0.5	
	0.31	0.31 ⁴	0.23	0.28	0.31	0.31	0.31	0.01	0.11	0.07	0.0013	0.002	0.002	0.01	0.09	0.06	0.001	0.0013	0.002	2	51	18	0.4	0.4	0.6	
Ct	Cement	0.23	0.22 ⁴	0.21	0.32	0.27	0.25	0.24	0.03	0.03	0.10	0.08	0.08	0.07	0.03	0.03	0.09	0.06	0.06	0.06	11	15	39	26	26	25
		0.41	0.44 ¹	0.43	0.44	0.54	0.41	0.44	0.09	0.06	0.06	0.14	0.11	0.10	0.07	0.05	0.04	0.13	0.09	0.09	17	11	11	32	22	21
		0.50	0.53 ⁴	0.58	0.53	0.54	0.54	0.53	0.09	0.10	0.06	0.08	0.09	0.09	0.07	0.08	0.04	0.06	0.07	0.07	14	14	8	12	15	14
		0.59	0.60 ⁴	0.17	0.28	0.41	0.33	0.30	0.06	0.42	0.32	0.19	0.27	0.29	0.07	0.42	0.31	0.18	0.26	0.29	14	250	53	31	44	49
		0.87	1.14 ¹	1.60	1.38	1.20	1.40	1.42	0.30	0.74	0.52	0.35	0.56	0.58	0.27	0.73	0.51	0.33	0.53	0.55	32	45	58	38	61	63
		1.02	1.03 ¹	1.16	0.96	0.99	0.97	0.98	0.08	0.17	0.09	0.07	0.09	0.09	0.07	0.15	0.07	0.06	0.08	0.07	7	13	7	6	7	7
		1.51	1.49 ¹	1.76	1.53	1.58	1.54	1.52	0.10	0.26	0.10	0.12	0.13	0.14	0.08	0.25	0.08	0.09	0.11	0.11	5	14	6	6	7	8

Table C.3. Complete analysis of the results of the MT model as function of the size of the training set. *Results of inference concern the independent test set. The MT model has been tested also on experimental data, independently of other models as separate baseline. Noise level is fixed at $\beta = 0.10$ for the alloy matrices, and $\beta = 0.03$ for the cement samples. Best results are selected from Table C.1 according to the smallest RMSE per sample. The MAPE has been used to discriminate possible equal values. Legend: ¹LR, ²MLR, ³PLS1, ⁴FCNN.*

X	Matrix	[X] wt %	Predicted [X] wt %						RMSE wt %						MAE wt %						MAPE (%)					
			MT (noise factor)						MT (noise factor)						MT (noise factor)						MT (noise factor)					
			Best	0.00	0.01	0.03	0.05	0.10	Best	0.00	0.01	0.03	0.05	0.10	Best	0.00	0.01	0.03	0.05	0.10	Best	0.00	0.01	0.03	0.05	0.10
Fe	Al	0.11	0.13 ⁴	0.13	0.07	0.07	0.09	0.11	0.04	0.02	0.05	0.06	0.03	0.02	0.02	0.02	0.04	0.04	0.03	0.013	22	17	40	41	25	12
		0.36	0.34 ²	0.41	0.41	0.41	0.40	0.32	0.06	0.13	0.13	0.13	0.13	0.09	0.05	0.12	0.12	0.12	0.11	0.09	15	33	34	33	32	24
		0.41	0.39 ⁴	0.45	0.51	0.51	0.52	0.42	0.04	0.05	0.11	0.13	0.13	0.02	0.04	0.04	0.10	0.12	0.12	0.02	10	10	24	30	28	4
		0.56	0.62 ⁴	0.67	0.60	0.60	0.60	0.53	0.10	0.12	0.07	0.06	0.06	0.04	0.09	0.11	0.05	0.05	0.05	0.03	15	20	10	8	8	6
		0.81	0.67 ²	0.75	0.80	0.80	0.77	0.77	0.2	0.07	0.03	0.04	0.05	0.05	0.15	0.06	0.02	0.03	0.05	0.04	18	8	3	4	6	5
	Co	0.10	0.11 ⁴	0.09	0.08	0.10	0.10	0.08	0.02	0.04	0.04	0.03	0.04	0.03	0.02	0.03	0.04	0.02	0.02	0.02	18	33	38	24	23	23
		0.33	0.34 ⁴	0.31	0.30	0.30	0.31	0.31	0.11	0.03	0.03	0.03	0.03	0.05	0.08	0.02	0.03	0.03	0.03	0.04	24	7	8	8	8	12
		0.61	0.56 ⁴	0.61	0.65	0.65	0.64	0.64	0.14	0.017	0.09	0.09	0.05	0.04	0.12	0.012	0.05	0.05	0.03	0.03	20	2	8	8	5	5
		1.07	1.07 ¹	1.06	1.03	1.03	1.06	1.07	0.06	0.02	0.04	0.04	0.02	0.02	0.05	0.02	0.04	0.04	0.02	0.02	5	2	4	4	2	2
		1.14	1.10 ⁴	1.11	1.11	1.10	1.11	1.14	0.05	0.03	0.04	0.05	0.04	0.01	0.04	0.03	0.03	0.04	0.03	0.006	4	2	3	4	3	0.5
	Cu	0.02	0.03 ⁴	0.04	0.03	0.03	0.04	0.02	0.02	0.02	0.015	0.02	0.02	0.012	0.014	0.02	0.013	0.019	0.02	0.010	85	141	83	116	135	63
		0.05	0.05 ²	0.06	0.04	0.05	0.07	0.05	0.013	0.02	0.010	0.012	0.024	0.009	0.010	0.02	0.009	0.009	0.02	0.007	22	42	21	21	50	16
		0.08	0.10 ³	0.10	0.08	0.11	0.10	0.11	0.03	0.02	0.011	0.03	0.03	0.03	0.02	0.02	0.010	0.03	0.02	0.03	27	25	12	31	28	31
		0.10	0.11 ¹	0.14	0.11	0.14	0.16	0.13	0.04	0.05	0.02	0.04	0.06	0.03	0.03	0.04	0.014	0.04	0.06	0.03	27	42	14	42	63	32
		0.17	0.17 ¹	0.16	0.15	0.18	0.18	0.17	0.05	0.015	0.022	0.009	0.019	0.011	0.04	0.012	0.017	0.007	0.016	0.010	25	7	10	4	9	6
Ni	0.06	0.06 ⁴	0.04	0.04	0.04	0.02	0.06	0.001	0.02	0.02	0.02	0.04	0.008	0.0009	0.02	0.019	0.018	0.04	0.007	1	30	31	30	59	12	
	0.25	0.26 ⁴	0.26	0.25	0.25	0.26	0.24	0.02	0.03	0.02	0.02	0.03	0.03	0.017	0.03	0.02	0.019	0.02	0.02	7	12	8	8	9	8	
	0.34	0.32 ⁴	0.33	0.30	0.30	0.31	0.33	0.03	0.02	0.04	0.05	0.04	0.02	0.02	0.02	0.04	0.04	0.03	0.02	7	6	12	13	10	5	
	0.97	0.95 ⁴	0.98	0.91	0.93	0.93	0.94	0.04	0.05	0.10	0.07	0.08	0.05	0.02	0.05	0.07	0.05	0.06	0.04	2	5	7	6	6	4	
	Sn	0.01	0.02 ³	0*	0*	0*	0.002	0.002	0.008	0.02	0.06	0.02	0.012	0.012	0.006	0.02	0.05	0.018	0.011	0.011	45	139	403	140	81	85
0.03		0.05 ³	0.01	0.01	0.01	0.01	0.02	0.03	0.02	0.02	0.02	0.015	0.011	0.02	0.014	0.02	0.014	0.014	0.009	74	51	80	49	51	33	
0.06		0.06 ³	0.03	0.02	0.04	0.05	0.05	0.009	0.03	0.04	0.019	0.012	0.009	0.008	0.03	0.04	0.018	0.009	0.007	13	45	66	32	16	12	
0.09		0.08 ³	0.03	0.02	0.04	0.06	0.07	0.02	0.05	0.07	0.04	0.03	0.02	0.017	0.05	0.06	0.04	0.02	0.019	19	62	74	51	28	22	
0.17		0.14 ¹	0.08	0.07	0.09	0.07	0.13	0.05	0.09	0.10	0.09	0.10	0.05	0.03	0.09	0.10	0.08	0.10	0.04	19	53	57	48	56	24	
0.18	0.14 ⁴	0.09	0.07	0.11	0.07	0.14	0.05	0.10	0.11	0.09	0.12	0.05	0.04	0.09	0.11	0.07	0.11	0.04	22	50	59	39	63	22		
Ti	0.01	0.02 ⁴	0.04	0.02	0.03	0.03	0.05	0.03	0.03	0.02	0.03	0.03	0.04	0.014	0.03	0.016	0.02	0.02	0.04	154	322	172	254	213	421	
	0.06	0.07 ⁴	0.11	0.10	0.10	0.08	0.10	0.03	0.12	0.11	0.10	0.06	0.06	0.03	0.07	0.07	0.07	0.05	0.05	56	119	120	123	86	92	
	0.11	0.09 ⁴	0.13	0.13	0.15	0.12	0.15	0.04	0.12	0.14	0.13	0.07	0.05	0.03	0.08	0.09	0.07	0.05	0.05	24	68	75	65	47	47	
	0.22	0.19 ⁴	0.31	0.28	0.30	0.27	0.24	0.06	0.3	0.24	0.21	0.10	0.04	0.05	0.3	0.2	0.19	0.09	0.04	22	115	98	86	43	20	
	1.19	1.19 ⁴	1.16	1.14	1.15	1.15	1.15	0.007	0.08	0.07	0.07	0.06	0.05	0.005	0.05	0.05	0.04	0.04	0.04	0.4	4	4	4	3	4	
Zn	0.02	0.05 ³	0.03	0.03	0.02	0.04	0.02	0.03	0.013	0.015	0.008	0.019	0.012	0.03	0.010	0.015	0.007	0.018	0.009	156	54	82	39	100	50	
	0.05	0.05 ¹	0.04	0.04	0.03	0.04	0.04	0.005	0.010	0.010	0.014	0.009	0.012	0.004	0.007	0.010	0.013	0.008	0.008	9	15	21	29	18	18	
	0.06	0.06 ⁴	0.06	0.05	0.06	0.06	0.06	0.004	0.003	0.013	0.030	0.011	0.008	0.004	0.002	0.011	0.02	0.011	0.007	7	3	18	41	17	11	
	0.07	0.06 ¹	0.07	0.07	0.07	0.08	0.07	0.014	0.010	0.008	0.011	0.008	0.012	0.012	0.006	0.006	0.008	0.006	0.008	17	8	9	11	8	11	
	0.10	0.06 ²	0.09	0.08	0.10	0.09	0.09	0.04	0.006	0.02	0.02	0.012	0.008	0.04	0.006	0.02	0.02	0.010	0.007	40	6	20	20	10	7	
Zr	0.02	0.08 ⁴	0.03	0.02	0.03	0.03	0.03	0.09	0.012	0.002	0.008	0.009	0.010	0.06	0.009	0.002	0.007	0.006	0.006	250	39	9	29	24	28	
	0.10	0.13 ²	0.10	0.10	0.09	0.10	0.10	0.04	0.0011	0.003	0.007	0.0007	0.003	0.03	0.0009	0.002	0.007	0.0007	0.003	35	1.0	2	7	0.7	3	
	0.25	0.23 ¹	0.26	0.25	0.26	0.25	0.26	0.06	0.005	0.002	0.004	0.002	0.003	0.04	0.004	0.002	0.003	0.0018	0.002	15	2	0.8	1.4	0.7	1.0	
	0.28	0.26 ¹	0.29	0.28	0.28	0.28	0.28	0.03	0.002	0.002	0.0009	0.0012	0.0010	0.03	0.002	0.002	0.0007	0.0010	0.0010	10	0.8	0.7	0.3	0.4	0.3	
	0.31	0.31 ⁴	0.31	0.31	0.31	0.31	0.31	0.009	0.003	0.004	0.003	0.002	0.0013	0.007	0.002	0.004	0.003	0.0015	0.0011	2	0.8	1.1	0.9	0.5	0.4	
Cl	Cement	0.23	0.22 ⁴	0.29	0.27	0.27	0.26	0.27	0.03	0.10	0.07	0.08	0.08	0.08	0.03	0.07	0.05	0.06	0.06	0.06	11	31	23	26	27	26
		0.41	0.44 ¹	0.56	0.52	0.54	0.49	0.42	0.08	0.18	0.17	0.14	0.09	0.06	0.07	0.15	0.13	0.13	0.08	0.05	17	36	31	32	18	12
		0.50	0.53 ⁴	0.52	0.54	0.54	0.52	0.52	0.09	0.08	0.12	0.08	0.08	0.09	0.07	0.07	0.08	0.06	0.06	0.07	14	13	16	12	12	14
		0.59	0.60 ⁴	0.40	0.49	0.41	0.41	0.44	0.09	0.2	0.14	0.19	0.2	0.17	0.07	0.2	0.12	0.2	0.2	0.2	14	33	21	31	31	26
		0.87	1.13 ¹	1.35	1.29	1.20	1.25	1.31	0.3	0.5	0.5	0.3	0.4	0.4	0.3	0.5	0.4	0.3	0.4	0.4	30	55	48	38	43	50
		1.02	1.02 ¹	1.04	1.02	0.99	0.99	1.01	0.08	0.09	0.07	0.07	0.09	0.09	0.07	0.08	0.07	0.06	0.07	0.08	7	8	6	6	7	8
		1.51	1.49 ¹	1.55	1.57	1.58	1.57	1.60	0.10	0.14	0.18	0.12	0.10	0.12	0.08	0.10	0.12	0.09	0.08	0.11	5	7	8	6	6	7

Table C.4. Complete analysis of the results of the MT model as function of the noise parameter. *Results of inference concern the independent test set. The number of synthetic samples is fixed to 1000, for illustration purposes. Best results are selected from Table C.1 according to the smallest RMSE per sample. The MAPE has been used to discriminate possible equal values. Legend: ¹LR, ²MLR, ³PLS1, ⁴FCNN (*negative prediction, set to zero).*

Matrix	[Fe] wt %	Predicted [Fe] wt %	MAPE (%)								t-value							
			358.12 nm	373.49 nm	373.71 nm	374.56 nm	382.04 nm	385.99 nm	404.58 nm	438.35 nm	358.12 nm	373.49 nm	373.71 nm	374.56 nm	382.04 nm	385.99 nm	404.58 nm	438.35 nm
Al	0.11	0.11 ± 0.02	76	45	65	28	29	28	56	66	0.97	1.45	1.49	0.93	1.08	0.65	1.84	1.59
	0.36	0.32 ± 0.09	32	29	61	29	25	24	15	35	0.88	0.86	1.10	0.98	0.70	0.61	0.66	0.84
	0.41	0.42 ± 0.02	7	12	40	10	13	7	19	17	0.70	0.95	1.22	0.66	1.14	0.57	0.62	1.04
	0.56	0.53 ± 0.04	8	12	40	10	18	4	16	7	0.66	0.84	1.56	0.81	1.04	0.81	0.77	0.90
	0.81	0.77 ± 0.05	10	11	21	15	6	8	10	13	0.49	0.46	0.60	0.78	0.44	0.47	0.62	0.48
Co	0.10	0.08 ± 0.03	32	10	16	9	20	20	8	12	0.91	0.81	0.69	0.91	1.02	0.85	0.69	0.51
	0.33	0.31 ± 0.05	16	8	18	20	17	14	23	15	0.70	0.56	0.65	0.65	0.71	0.44	0.98	0.50
	0.61	0.64 ± 0.04	22	13	12	7	9	14	11	19	1.13	1.36	0.84	0.63	0.50	0.75	0.83	1.17
	1.07	1.07 ± 0.02	11	10	12	11	13	18	13	10	1.02	0.82	0.81	1.00	0.83	1.00	1.14	0.67
	1.14	1.140 ± 0.008	10	8	13	7	7	10	12	15	0.88	0.83	0.97	0.47	0.57	1.02	0.74	1.04
Cu	0.02	0.02 ± 0.01	28	109	79	42	74	18	12	36	0.70	1.68	0.90	0.89	1.09	0.59	0.49	0.93
	0.05	0.045 ± 0.009	37	49	138	38	35	22	18	24	0.68	0.66	1.12	1.07	0.64	0.90	0.46	0.56
	0.08	0.11 ± 0.03	59	30	62	40	28	39	27	31	0.88	0.68	0.86	0.79	0.66	1.69	0.67	0.63
	0.10	0.13 ± 0.03	44	49	62	28	31	20	32	31	1.56	0.88	1.88	0.81	0.96	0.71	1.07	0.91
	0.17	0.17 ± 0.01	34	28	40	22	32	20	25	26	1.16	1.01	0.67	0.68	0.80	0.92	0.82	0.78
Ni	0.06	0.059 ± 0.008	24	15	8	12	28	24	16	27	1.82	0.74	0.69	0.76	0.84	1.36	0.74	0.86
	0.25	0.24 ± 0.03	12	12	9	9	15	14	17	19	0.86	0.79	0.81	0.62	1.02	1.40	0.96	1.06
	0.34	0.33 ± 0.02	10	12	11	9	12	14	16	14	0.88	0.89	0.72	0.82	0.91	0.83	1.13	0.72
	0.97	0.94 ± 0.05	13	16	8	14	10	8	7	22	0.67	0.68	0.58	0.72	0.69	0.42	0.48	0.59
	Sn	0.01	0.00 ± 0.01	91	269	58	789	106	544	385	42	1.05	1.29	0.61	0.70	0.83	1.33	0.75
0.03		0.02 ± 0.01	40	24	30	44	14	69	38	29	0.65	0.57	0.60	0.85	0.59	0.75	0.58	0.78
0.06		0.052 ± 0.009	50	64	32	401	28	30	155	89	0.92	0.79	0.89	0.63	0.36	0.38	0.93	0.58
0.09		0.07 ± 0.02	25	16	36	84	18	41	29	54	0.83	0.50	0.53	0.84	0.63	0.63	0.71	0.75
0.17		0.13 ± 0.05	24	23	31	32	61	24	24	22	0.52	0.73	0.60	0.74	0.53	0.49	0.44	0.48
Ti	0.01	0.05 ± 0.04	13	15	19	10	12	5	13	11	0.70	0.69	1.05	1.26	0.73	0.60	0.84	1.84
	0.06	0.10 ± 0.06	11	19	7	11	9	6	7	11	0.74	0.73	0.51	0.86	0.59	0.68	0.61	0.58
	0.11	0.15 ± 0.05	9	9	8	10	7	5	6	11	1.01	0.55	0.73	0.72	0.62	0.51	0.51	0.69
	0.22	0.24 ± 0.04	5	8	6	8	12	4	9	10	0.35	0.62	0.53	0.58	0.72	0.40	0.48	0.66
	1.19	1.15 ± 0.05	8	12	7	7	7	9	8	4	0.87	0.73	0.72	0.78	0.97	0.85	0.78	0.45
Zn	0.02	0.02 ± 0.01	123	361	174	42	135	65	338	155	1.33	1.54	1.06	0.90	1.49	0.99	1.57	1.86
	0.05	0.04 ± 0.01	75	127	136	80	95	70	125	128	0.56	1.03	0.96	1.13	0.96	0.80	1.18	0.96
	0.06	0.059 ± 0.008	119	219	123	45	159	110	301	76	0.52	0.55	0.52	0.52	0.56	0.55	0.55	0.52
	0.07	0.07 ± 0.01	93	67	110	76	48	118	75	79	0.59	0.59	0.58	0.68	0.59	0.62	0.56	0.54
	0.10	0.094 ± 0.008	281	292	191	173	131	176	194	111	0.71	0.86	0.74	0.75	0.73	0.77	0.81	0.59
Zr	0.02	0.028 ± 0.010	8	6	13	7	5	9	5	7	0.79	0.80	0.76	0.70	0.61	0.84	0.87	0.75
	0.10	0.099 ± 0.003	9	7	6	5	8	12	5	7	0.65	0.50	0.63	0.51	0.62	0.70	0.48	0.53
	0.25	0.255 ± 0.003	9	9	7	8	7	10	7	5	0.70	0.63	0.68	0.61	0.77	0.75	0.55	0.57
	0.28	0.282 ± 0.001	5	11	6	8	9	6	5	8	0.48	0.68	0.75	1.06	1.48	0.56	0.63	1.53
	0.31	0.3092 ± 0.0013	10	8	6	4	10	10	10	4	0.86	0.51	0.61	0.45	0.79	0.74	0.44	0.79

Table C.5. Results of the validation analysis on the alloy matrices. *Results concern the independent test set. The number of synthetic samples is fixed to 1000 and the noise factor to $\beta = 0.10$.*

D Complementary Figures

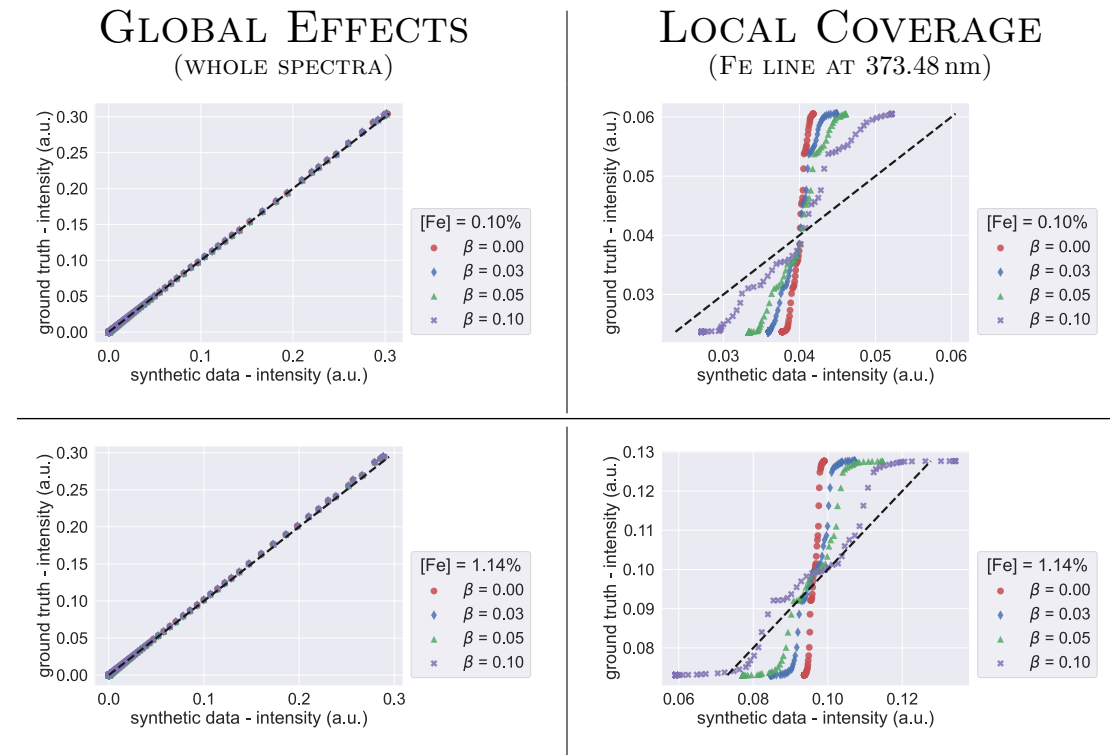


Figure D.1. Global (average spectrum) and local (Fe line at 373.48 nm) coverage of the synthetic Co matrix dataset (1000 synthetic spectra per sample) at low and high Fe concentrations.

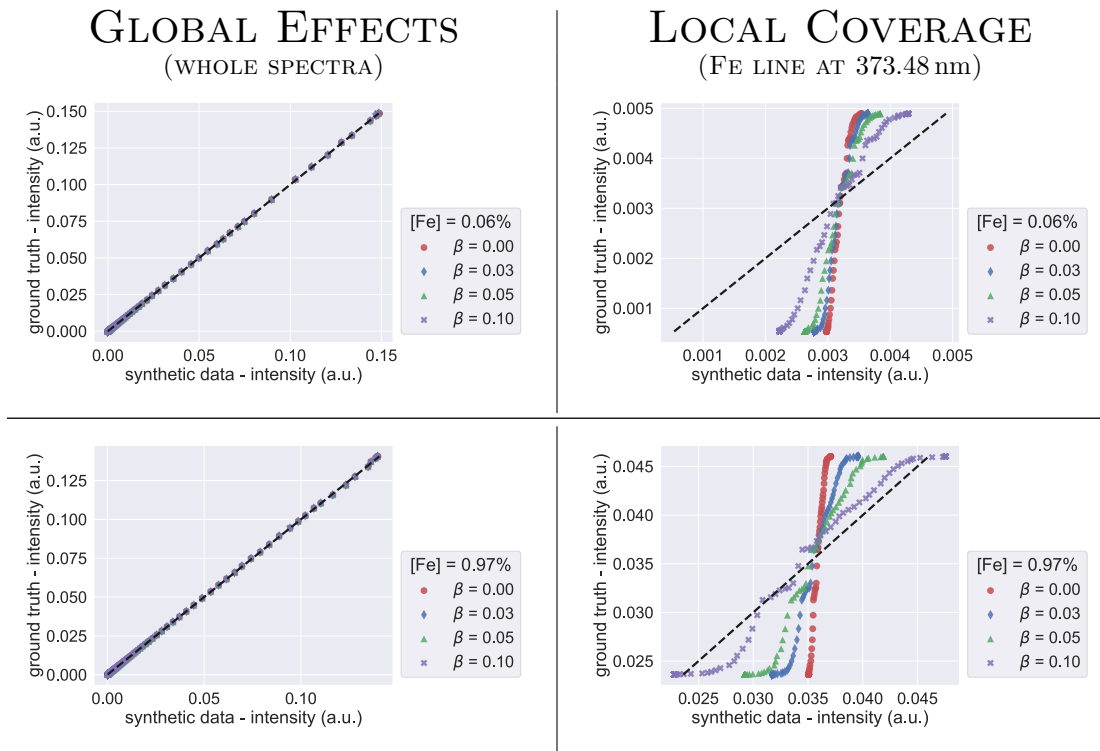


Figure D.2. Global (average spectrum) and local (Fe line at 373.48 nm) coverage of the synthetic Ni matrix dataset (1000 synthetic spectra per sample) at low and high Fe concentrations.

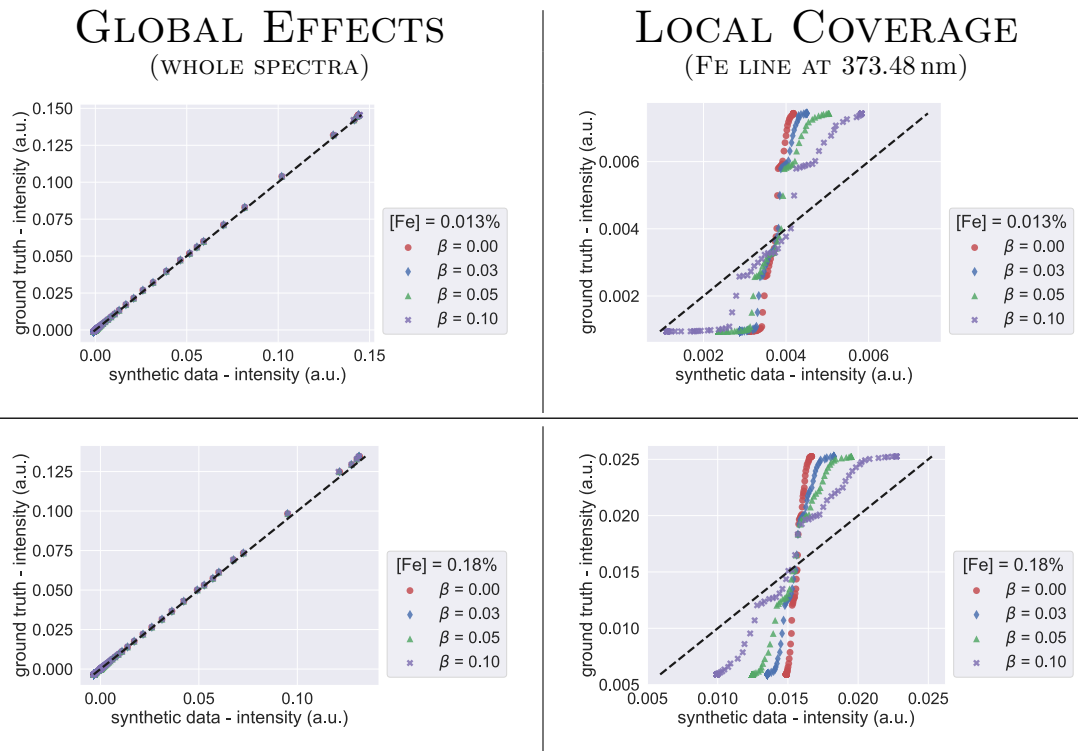


Figure D.3. Global (average spectrum) and local (Fe line at 373.48 nm) coverage of the synthetic Sn matrix dataset (1000 synthetic spectra per sample) at low and high Fe concentrations.

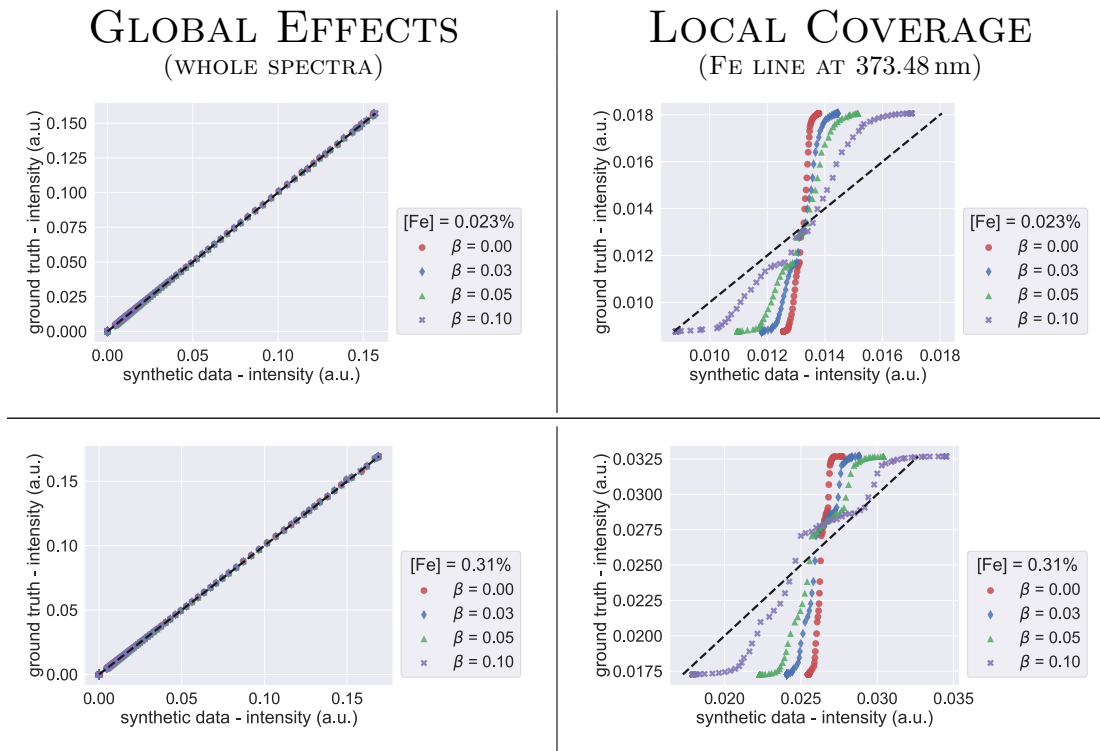


Figure D.4. Global (average spectrum) and local (Fe line at 373.48 nm) coverage of the synthetic Zr matrix dataset (1000 synthetic spectra per sample) at low and high Fe concentrations.

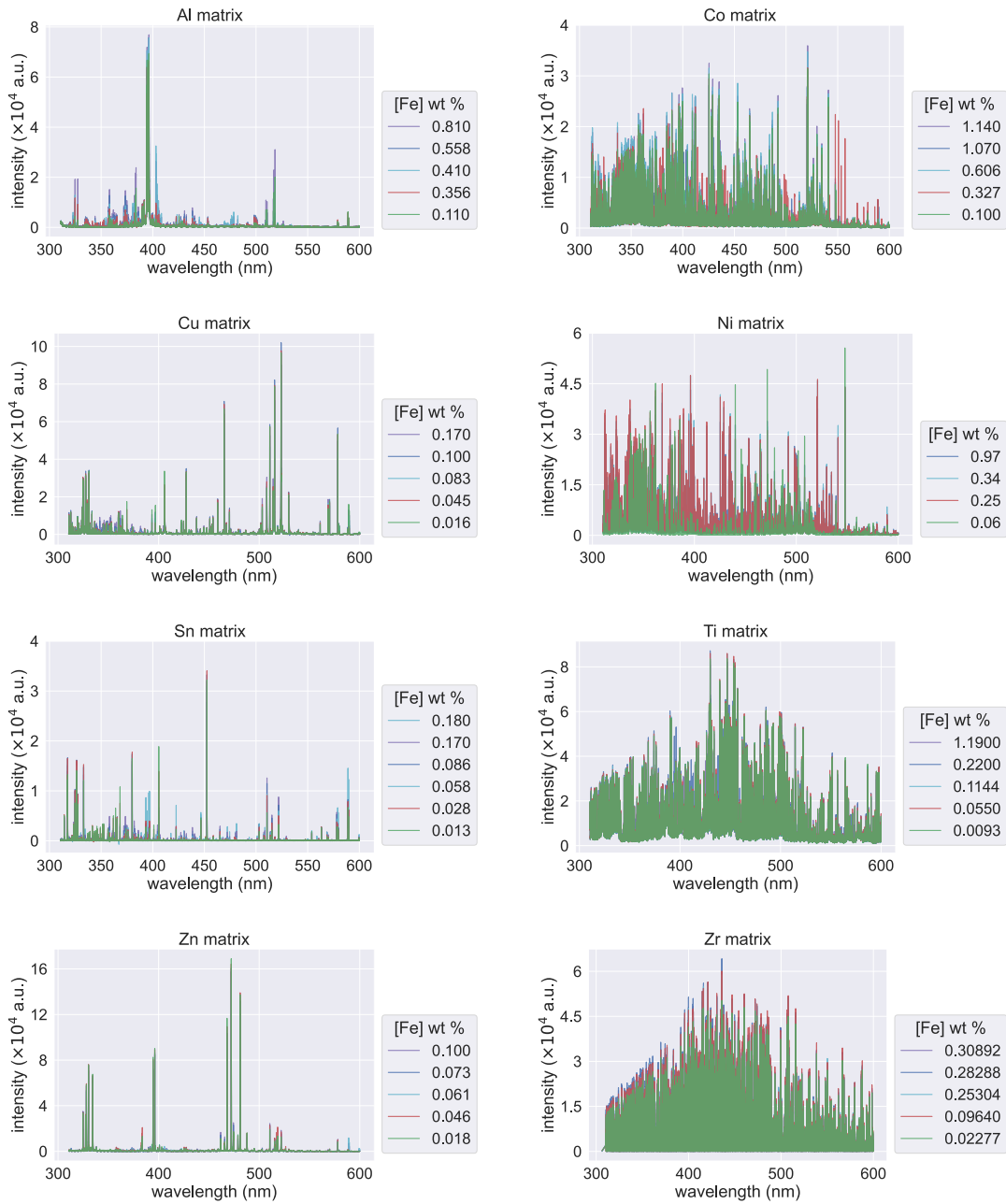


Figure D.5. Average spectra of the alloy matrices before preprocessing.

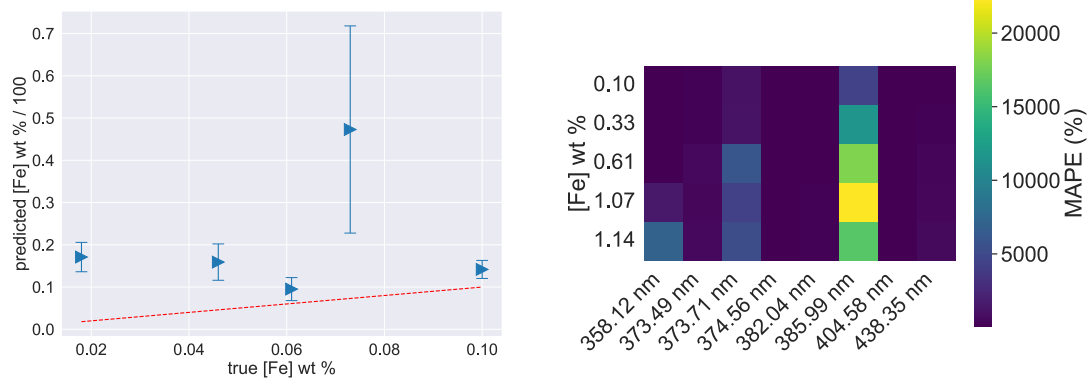


Figure D.6. Results of the calibration of the Zn matrix using the MT model trained on the Co matrix.